Title
How to couple trapped ions to superconducting resonators: towards hybrid quantum devices

Author
Moeller, Soenke Alexander

Publication Date
2016

Peer reviewed|Thesis/dissertation

How to couple trapped ions to superconducting resonators: towards hybrid quantum devices

by

Sönke Alexander Möller

A dissertation submitted in partial satisfaction of the

requirements for the degree of

Doctor of Philosophy

in

Physics

in the

Graduate Division

of the

University of California, Berkeley

Committee in charge:

Professor Hartmut Häffner, Chair
Professor Holger Müller
Professor Jeffrey Bokor

Fall 2016

How to couple trapped ions to superconducting resonators: towards hybrid quantum devices

by

Sönke Alexander Möller

Abstract

How to couple trapped ions to superconducting resonators: towards hybrid quantum devices

by

Sönke Alexander Möller

Doctor of Philosophy in Physics

University of California, Berkeley

Professor Hartmut Häffner, Chair

In this dissertation, we present work on a quantum hybrid device comprising of a trapped calcium atom and a superconducting LC resonator. This hybrid device is a first step towards building a hybrid quantum computer that can take advantage of the different properties of atomic and superconducting quantum systems and combine the best characteristics of both.

We model a trapped ion as an LC circuit and calculate its coupling to a mode of an LC resonator. Further, we optimize the trap geometry and placement of coupling electrodes to increase the coupling. We also outline the manufacturing process and simulation of the trapping potentials for the surface traps used in this work.

Finally, we report on initial experiments coupling a trapped ion to a resonant mode of the LC resonator, increasing the heating rate to 220 $\frac{\text{phonons}}{\text{ms}}$ on resonance versus 0.5 $\frac{\text{phonons}}{\text{ms}}$ without additional heating from the resonator. The ratio of the heating rates for the two secular frequencies of the ion confirm our simulated coupling rates.

Contents

List of Figures **iv**

List of Abbreviations **vi**

Acknowledgments **vii**

1 Introduction and motivation **1**

I Background **3**

2 Trapping and cooling of calcium **4**
2.1 Trapping ions with Paul traps 4
2.1.1 Surface traps 6
2.2 Energy levels of neutral Calcium 7
2.3 Energy levels of Ca^+ 8
2.4 Doppler cooling of trapped ions 9
2.5 Rabi oscillations 10
2.5.1 Temperature measurement with Rabi flops 12
2.5.2 Sideband transitions 13

3 Ion as a circuit element **15**
3.1 The ion as an LC circuit 15
3.2 Coupling ions and LC resonators 17
3.3 Heating and cooling the LC resonator 18

4 Trap design **21**
4.1 Boundary element method simulations 21
4.2 Trap design 24
4.3 Coupling electrodes 26
4.4 Heating rate of the ion 30

II Experiment **32**

5 The cryostat **33**
5.1 Thermal loads 36
5.2 Thermometry 38
5.3 Vacuum chamber 39
5.4 Laser setup 39
5.5 Imaging and detection 41

6 The superconducting LC resonator **44**
6.1 Resonator Theory 45
6.1.1 Dielectric losses 46
6.1.2 Choice of wire 47
6.1.3 Thermal anchoring 50
6.1.4 Coil former and magnetic shielding 51
6.2 Measuring the quality factor 53
6.3 Iterative improvements of the solenoid LC resonator 56
6.3.1 Toroidal resonators 61
6.3.2 Finite DC resistance 61

7 Trap fabrication and electronics **62**
7.1 Trap fabrication 62
7.1.1 Ion etch patterning of substrates 63
7.1.2 Pulsed laser patterning of substrates 63
7.1.3 Evaporation of traps 64
7.2 Voltage sources 67
7.2.1 Electric components at cryogenic temperatures 69
7.2.2 RF drive 70
7.3 Ca-oven 71
7.4 Trap frequency stabilization 72
7.4.1 The RF voltage stabilization circuit 72
7.4.2 Measurement of the trap frequency 74
7.4.3 Results of RF stabilization 75

8 Trap operation and coupling **77**
8.1 Trap operation 77
8.1.1 Micromotion compensation 78
8.1.2 Build up of stray fields 80
8.2 Heating the ion with the LC resonator 81

9 Summary and outlook **85**

Bibliography **87**

List of Figures

2.1 Level diagram for CaI showing the energy levels discussed here [1]. 8
2.2 Energy level diagram of Ca^+ with an applied magnetic field. 9

3.1 Describing an ion as a series LC circuit 16
3.2 Schematic of the ion connected to a LC resonator 17

4.1 Simulated potention for a surface trap 25
4.2 Abandoned design of a 3D trap for coupling to the ion. 25
4.3 Design drawing of an F-trap, a surface trap. 27
4.4 Pictures illustrating the construction of the coupling electrode. 27
4.5 Illustration of the wire positioning above the trap. 29

5.1 Measurement of the vibrations of the cold finger. 34
5.2 Temperature of the cold finger versus time after cooling is switch off. 35
5.3 Temperature of the cold finger plotted against heat load. 37
5.4 A rough sketch of the vacuum setup shown as a cut through the center. . . 40
5.5 Sketch of the laser setup. 42

6.1 Illustration of the presence of multiple resonances in a LC resonator built from a single layer solenoid. 46
6.2 Measurements of different niobium and NbTi wires. 48
6.3 Limit on Q due to surface resistance at 2 MHz. 50
6.4 The coil winding machine. 52
6.5 Picture of a finished coil. Nb wound on a quartz cylinder. 52
6.6 Measurement setup. 54
6.7 FFT amplitude of the return signal for multiple frequencies. 54
6.8 Visualization of the fitting procedure to determine τ. 55

6.9 Q factor vs frequency for a variety of different resonators we built. 56
6.10 The plot is showing the temperature dependence of the quality factor for three different modes of the resonator for an early LC resonator. 58
6.11 Alternative coupling method to the previously shown measurement board. . 59
6.12 Picture of a toroidal resonator and the PTFE parts used as a former. 60

7.1 Illustration of the evaporation process and trap mounting. 63
7.2 Nodules ejected during copper and gold evaporation. 65
7.3 Picture showing how we mount our traps in the cryostat. 68
7.4 Circuit diagram for the capacitive divider used to measure the amplitude of the RF drive. 71
7.5 The RF stabilization setup. 73
7.6 Construction of a temperature insensitive rectifying circuit for RF stabilization with increasing temperature stability from a) to c). 73
7.7 Variation of the radial trap frequency measured over the course of a few hours. 76

8.1 Simulation of the scattering rate for different amplitudes of micromotion and detuning. 79
8.2 Measurement of the heating rate of the ion when coupled to the LC resonator for various RF drive powers 83

List of Abbreviations

BEM	Boundery Element Method
CLCC	Ceramic Leadless Chip Carriers
DAC	Digital to Analogue Converter
DMM	Digital Multi-Meter
DRIE	Deep reactive-ion etching
EMCCD	Electron multiplying charge-coupled device
FFT	Fast Fourier Transform
FPGA	Field Programmable Gate Array
ICP	Inductively Coupled Plasma
MLCC	Multi-layer ceramic capacitors
NIR	Near Infrared
OFHC	Oxygen-free high thermal conductivity
PID	Proportional-integral-derivative
PMT	Photomultiplier tube
PTFE	Polytetrafluoroethylene (Teflon)
QCM	Quartz Crystal Microbalance
REBCO	Rare Earth Barium Copper Oxide

Acknowledgments

First and foremost, I would like to thank my family, especially my parents, Ingeborg and Niels, and my sister Mareike for all the support they have given me during my Ph.D. studies and throughout my life journey. Their encouragement helped me when things got tough.

A special thanks goes to my adviser, Hartmut Häffner. If our paths had not crossed, I would not be involved in the fascinating world of trapped ions or been able to experience Berkeley. His constant support with ideas gave me a new point of view when I had to tackle a problem, and letting me pursue whatever aspects of the work piqued my interest. His vast knowledge of the field of ion trapping served as a cornucopia of suggestions what to try next when the experiment was not working.

I would also like to thank my thesis committee, Holger Müller and Jeffrey Bokor, who listened to my qualification exam talk together with Yasunori Nomura. Especially Holger Müller, who took the time for a long walk through campus to discuss a way forward when I was down with my luck.

This work would also not have been possible without the help along the way from many great postdocs. Nikos Daniilidis, who had many of the early ideas jump-starting the experiment and providing invaluable guidance with his attention to detail and great physical intuition. He was a great mentor in the early years of my Ph.D. Philipp Schindler, who breathed a new life into the experiment and whose drive helped me to spend many long and very productive days pushing for the first few coupling results. His guidance was priceless and provided me with a surge of motivation. Clemens Matthiesen, whose interest and fresh idea helped me to review a lot of what we had done before and who helped me greatly refining this dissertation. Also, I have to mention Sankar Narayanan, who welcomed me to CCT and taught me a lot when I was new to the group, thank you.

Many greatly skilled undergraduate students worked on various important aspects of this project and provided me with the manpower needed to get everything done. Ryoh Masuda, Ryan Blais, and Brian Timar surprised me again and again by finishing tasks that I had

expected to take weeks on the next day.

Thanks also to the lattice team, Börge Hemmerling, Eli Magidash, and Dylan Gorman, for letting me join them and gain more experience with quantum simulations. It was exciting to work on a new project and I have learned a lot building the experiment and measuring with you. Eli also provided me with much-needed insight on working in industry in his discussions with me, for which I am grateful for. The enthusiasm and knowledge of Börge helped me learn valuable lessons on how to approach new projects.

Also, the other lab members that I did not work directly with but who created the great atmosphere of the Häffner Lab: Ahmed Adelrahman, Da "Chi Chi" An, Axel Kreuter, Maya Lewin-Berlin, Oliver Neitzke, Crystal Noel, Thaned "Hong" Pruttivarasin, Michael Ramm, Anthony Ransford, Ishan Talukdar, and Erik Urban. This group has always positively surprised me with their camaraderie and the many activities we do together after work has finished.

This work would have been much harder had it not been for the support of the many great people of the physics department at UC Berkeley. Anne Takizawa, who helped me answer countless questions even before I was a student at Berkeley, who seems to know everyone by name, and will know what everyone is about to ask as they step into her office. Anthony Vitan, Eleanor Crump, and Carlos Bustamante who keep the building running and were always ready to help within a heartbeat. The many people of the machine shop, Warner Carlisle, Gordon Long, Abel Gonzales, who helped me produce the intricate designs that I could not make myself or in the case of Joseph Kant, taught me what to look out for when building them.

Finally, I would like to thank my friends. Aaron Bradley, who is still my roommate and is always there to discuss physics or the world. Natania Antler, Itamar Kimchi-Schwartz, Victoria Martin, Nathan Roth, Derek Vigil-Fowler, and Steven Weber with whom I spent many long nights working on problem sets or out drinking. I also will never forget the many great people of the UC Berkeley Martial Arts Program. Training with you helped me grow as a person and provided a valuable balance to countless hours spent thinking, building, and sitting in front of the computer. The club provided me with many role models to aspire to, mentors, and friendships that I hope will last a lifetime.

1 Introduction and motivation

Feynman proposed to study difficult quantum mechanics problems by using well-controllable quantum systems as computers [2]. This idea picked up considerable speed later when multiple complex algorithms that would solve problems faster on a quantum computer than on a classical machine [3][4] provided a great impetus to create a universal quantum computer and implement these algorithms. In 2000 DiVincenzo listed the criteria necessary for a universal quantum computer [5] and today there are multiple different systems that have demonstrated all of the criteria or have made big steps towards fulfilling them [6].

Trapped ions and other atomic systems have the benefit, that they are highly isolated from the environment and have long lived states that can preserve quantum information over extended times. Also, a high level of control of the quantum states has been demonstrated [7][8]. A proposal by Cirac and Zoller [9] opened up the possibility of creating a universal quantum computer by describing a two-qubit gate, which was the last missing building block for a universal quantum computer based on trapped ions. Since then a lot of work was carried out to demonstrate high fidelity gates [10], become resistant to errors [11], and scale up to more qubits [12][13]. Experiments have also shown methods to extend the storage time of quantum information by using decoherence-free subspaces [14].

Besides ions, multiple other examples of promising architectures have been demonstrated. Some examples of systems, that are under investigation, are nitrogen vacancy centers in diamond [15], a variety of superconducting qubits [16], the nuclear spin of ^{29}Si in ^{28}Si [6], and photons [6]. Currently, many candidate systems have complementary characteristics needed for good performance of a quantum computer, such as fast gate speeds in superconducting qubits or long coherence times in trapped ions.

Because of these complementary benefits, there are many proposals combine different architectures into hybrid quantum systems. Constructing these hybrid systems faces technological and fundamental challenges and only little progress has been made in this direction so far. Most advances are of theoretical nature. For ions, proposal exist to couple to Josephson junctions devices [17][18][19] and nanomechanical oscillators [20] among others. Examples of other systems include proposals to couple Rydberg atoms to each other via superconducting

lines [21] or coupling mechanical resonators and trapped atoms [22].

Here we pursue the route of coupling trapped ions to superconducting LC resonators. We will see that resonators used in this dissertation can also be understood as transmissions lines. Coupling of superconducting qubits to transmission lines has already been successfully demonstrated [23][24]. Interfacing a trapped ion with an LC resonator would be the next step in coupling superconducting qubits to trapped ions. Approaches for this type of hybrid device has been theoretically discussed in [25] and [26].

Because of technical challenges of building a true hybrid quantum system and show entanglement of the ion and LC resonator, we investigate the first coupling mechanism and perform proof of principle experiments. In an initial experiment, we observe energy flow from the LC resonator to the ion. As the resonator temperature is many orders of magnitude higher than that of a Doppler cooled ion this energy flow is large and thus a good first step to observing the interaction of the two systems. Next, we plan to use the ion to cool one of the resonant modes of the LC resonator using the ion to detect the achieved cooling [25].

This thesis is structured as follows.

Chapter 2 covers the functioning principles of ion trapping and the detailed level diagram of neutral and singly ionized calcium. Further, we discuss light-atom interactions as relevant for laser cooling as well as driving Rabi oscillations on the long-lived Ca^+ transitions. **Chapter 3** provides the theory framework of modeling a trapped ion as a series LC circuit and the coupling of an ion to an LC resonator. **Chapter 4** discusses the simulation of trapping potentials using the boundary element method. We also look into the design of the trap and the coupling electrode to maximize the coupling. We also define the heating rate of an ion trap and provide details on which parameters influence it for a surface ion trap. **Chapter 5** discusses the design of the cryostat that is housing the ion trap as well as the LC resonator. We explain what affects the ultimate base temperature of the cryostat as well as the laser and detection setup. **Chapter 6** focuses on one of the major parts of the experiment, the design of the superconducting LC resonator. The presence of multiple resonances and parameters affecting the quality factor are discussed. We also explain the measurement setup to characterize the resonator and our results for an ultra high quality factor LC resonator. **Chapter 7** focuses on the second major part of the experiment, the ion trap. We discuss its fabrication as well as the electronics necessary to operate it. **Chapter 8** reviews the trapping experiments conducted so far as well as initial experiments coupling the LC resonator to a trapped ion. **Chapter 9** contains a summary and an outlook on possible future work.

Part I

Background

2 Trapping and cooling of calcium

For our experiments, we need to control the position, as well as the momentum and internal states of calcium ions. In this chapter, we will explain how we can confine ions in a small volume, cool them to temperatures close to their motional ground states, and control their electronic quantum state.

2.1 Trapping ions with Paul traps

The Paul trap was invented in 1953 by Wolfgang Paul [27] and is used to trap charged particles or ions using static and dynamic electric fields. It is an alternative to the Penning trap invented by Hans Dehmelt [28] which uses a combination of static quadrupolar electric fields and a homogeneous magnetic field. A benefit of the Paul trap is that the trapped particle can be almost static, while in a Penning trap the trapped ions circle the trap center in a meta-stable obit. In the experiments discussed here, we choose the Paul trap to avoid this motion.

The electrical field trapping the ion can be decomposed into a time-independent and a sinusoidally varying part that is driven by an RF voltage source. To ease the discussion, we assume specific quadrupolar potentials of the form

$$\Phi(x,y,z,t) = U\frac{1}{2}(\alpha x^2 + \beta y^2 + \gamma z^2) + \tilde{U}\cos(\Omega_{RF}t)\frac{1}{2}(\alpha' x^2 + \beta' y^2 + \gamma' z^2)\,. \tag{2.1}$$

Here Ω_{RF} is the frequency of the RF trap drive, $\tilde{U}$ the amplitude of the RF trap drive and U the amplitude of the DC potential. With this parametrization both potentials fulfill the Laplace equation $\Delta\Phi = 0$. Multiple choices of α, β, and γ are possible to satisfy the Laplace equation, though for our traps the geometric factors typically are [29]

$$\begin{aligned} \alpha + \beta &= 2\gamma \\ \alpha' &= -\beta' \end{aligned} \tag{2.2}$$

This choice results in dynamical confinement along the x- and y-axis of trap and confinement by the static potential along z. The equations of motion of the ion are decoupled in the spatial directions. Here we will only consider the equation of motion in the x coordinate for an ion of mass m with a charge Q.

$$m\ddot{x} = -Q\nabla\Phi = -Q(U\alpha + \tilde{U}\cos(\Omega_{RF}t)\alpha')x\,. \tag{2.3}$$

We define a few new variables

$$\begin{aligned} \xi &= \tfrac{\Omega_{RF}t}{2} \\ a_x &= \tfrac{4QU\alpha}{m\Omega_{RF}} \\ q_x &= \tfrac{2QU\alpha'}{m\Omega_{RF}} \end{aligned} \tag{2.4}$$

transforming Eq. 2.3 to the standard form of the Mathieu differential equation [29]:

$$\frac{d^2x}{d\xi^2} + (a_x - 2q_x\cos(2\xi))x = 0\,. \tag{2.5}$$

From the Floquet theorem, we find the general stable solutions [29]

$$x(\xi) = Ae^{i\beta_x\xi}\sum_{n=-\infty}^{\infty} C_{2n}e^{i2n\xi} + Be^{-i\beta_x\xi}\sum_{n=-\infty}^{\infty} C_{2n}e^{-i2n\xi}\,. \tag{2.6}$$

The recursive relation for C_{2n} and the characteristic exponent β_x, which is a function of a_x and q_x is detailed in [29] and many other publications. This equation has no solution with closed form but can be approximated in lowest order as

$$x(t) = 2AC_0\cos(\omega_x t + \phi_i)\left(1 + \frac{q_i}{2}\cos(\Omega_{RF}t)\right)\,. \tag{2.7}$$

The factor $2AC_0$ is used to satisfy initial conditions. ω_x is called the secular frequency and is given by

$$\omega_x = \beta_x\frac{\Omega_{RF}}{2} \text{ with } \beta_x = \sqrt{a_x + \frac{q_x^2}{2}}\,. \tag{2.8}$$

From this solution, we see that the motion of the ion consists of harmonic oscillations with a frequency ω_x superposed with a much faster oscillation at the RF drive frequency. The position the ion would be trapped at by purely the RF voltage is called the RF null, as it is where the amplitude of the oscillating potential is zero. For a Paul trap build from four rods assembled in a quadratic shape with end caps [30], this RF null is along a line in the center of the trap. If the ion is not exactly at the RF null, which is never the case due to a certain extent of the ion motion, even in the ground state $x_0 = \sqrt{\frac{\hbar}{2m\omega_i}}$, it exhibits this driven motion originating from the RF potential. This additional oscillation with the drive frequency is called micromotion. The amplitude of the micromotion increases if linear electric fields displace the ion further from the RF null, but this excess micromotion can be

compensated by applying the right compensation fields which push the ion back to the RF null.

2.1.1 Surface traps

In our experiments we use surface traps. These microfabricated Paul traps have typically a much smaller ion electrode distance. This is important for our experiment as the coupling rate between the ion and the LC resonator scales linearly with the inverse of the distance fo the ion from the trap electrodes, so we want to trap an ion with the smallest ion-electrode distance possible, see Sec. 3.2. Additionally, we can try different trap geometries in fast iterations as we can fabricate multiple different traps at once and quickly test them to see if they provide an advantage in our experiment. This would be much harder with the hand assembled macroscopic Paul traps. To make those arguments more concrete, we discuss below the various trap types used in experiments.

Traditionally, Paul traps were three-dimensional, fabricated in a machine shop and hand-assembled. While these traps have been very successfully used in many experiments, it is difficult to achieve the necessary accuracy of the assembly when we want to miniaturize the Paul traps. Miniaturization is desired when trying to trap tens or even hundreds of ions as the distance between ions decreases as more ions are loaded into the same trap. With miniaturized traps, this problem can be bypassed by using the electrodes to spread the ions out [12] and make single ion addressing possible even for a large number of ions in the same trap. In the first step towards miniaturization, the trap electrodes were micro-machined with pulsed lasers and the electrodes later electroplated [31]. However, these traps still require some hand assembly.

One example of completely micro-fabricated traps are so-called surface traps that have been used in ion trap experiments for the last decade [32][33]. In these traps all the electrodes lie in a single plane. For surface traps, the accuracy of the electrode arrangement is limited only by micro-fabrication techniques which are very similar to those used in the semiconductor industry, so nanometer scale resolution is achievable. This is important as the length scale of the electrodes correlates in most designs directly with the trapping height [34]. Due to the small electrode sizes, we can locally compensate stray electric fields along the trap axis and ion-electrode distances down to a few tens of micrometers are possible.

Surface traps are also one of the possible pathways to scale up quantum computation with trapped ions. Besides the advantage of miniaturization having multiple segmented DC electrodes, they also allow for shuttling of ions from one end to another by locally changing the trapping potential and have separate trapping, cooling, and interaction areas [12].

Since the first proposal of a surface trap architecture, many advances have been made showing the shuttling of trapped ions [35][36]. Also, multi-qubit gates based on microwave have been demonstrated that are only possible due to the small ion-electrode spacing [37]. Due to the same requirement of small ion trap distances, the study of microwave gates helps to advance technologies also required for the experiments discussed here.

2.2 Energy levels of neutral Calcium

While there are methods of directly generating charged metal ions via laser ablation [38] [39] or generating them from a diffuse gas via impact ionization [40], both of these methods suffer from the generation of stray charges that create a force pushing the ion from the RF null resulting in excess micromotion [40][38]. This micromotion then needs to be compensated for us to be able to perform precision experiments. The presence of stray charges is greatly reduced when creating ions via photoionization [38], which is the method of choice in this work.

The ionization energy for CaI is 6.11316 eV, which corresponds to a photon wavelength of 202 nm. Experiments have shown that light below a wavelength of 422 nm can produce charges on glass (light at 397 nm created charges while light at 422 nm did not), which leads to an electric field displacing trapped ions. Glass is an important material to consider as there are multiple viewports in our setup close to the trapped ions. Creating charges on isolating patches on the metal electrodes of a surface trap was observed even with light at 729 nm, though a higher rate of charge creation was observed at lower wavelengths [41]. From this study it seems beneficial to avoid high energy photons when possible, which is why we use a multiphoton process. Some of the energy levels of neutral calcium are shown in Fig. 2.1. For all of these transitions, there are diode lasers available simplifying the experimental setup. In our laboratory we use a two-step process, first exciting to the 4^1P_1 state using light from a frequency-doubled diode laser [42] before using light from a diode laser with a wavelength of 375 nm to excite the electron past the ionization limit. An additional benefit of this method is that the photoionization is isotope selective [43] minimizing loading of the wrong calcium isotope which would show up as a dark ion due to the different transition frequencies.

We also tested a three-photon ionization method by exciting the $4^1P_1 \rightarrow 4^1D_2$ transition with a diode laser at 732.6 nm before exciting to the continuum with a free running laser diode at 830 nm. This ionization pathway utilizes photons that have shown a minimal generation of stray charges [41] and have been predicted to selectively ionize rare calcium isotopes such as ^{41}Ca even from an unenriched source. This is useful for calcium dating, a method similar to carbon dating [44]. To find the correct frequency, which might be shifted due to Doppler shifts, we first excite to the 4^1P_1 state. We then scan the frequency of the 732.6 nm laser and look for reductions in the 422 nm fluorescence signal. Using this method we successfully loaded calcium ions but chose the two-photon method due to the greater simplicity.

Very high stray fields encountered during trapping experiments in the cryostat (see Sec. 8.1.2) might make it necessary to revisit the three-photon method. It might also prove useful in experiments with low trapping heights where light scatter from the 375 nm laser is harder to avoid. For traps with a 80 µm trapping height we typically have a beam diameter of 50 µm. This beam diameter allows us enough margin of error in positioning to be sure to ionize calcium. Additional windows in our setup lead to difficulties in achieving an ideal gaussian beam resulting in visible reflections on the trap when the beam is positioned at

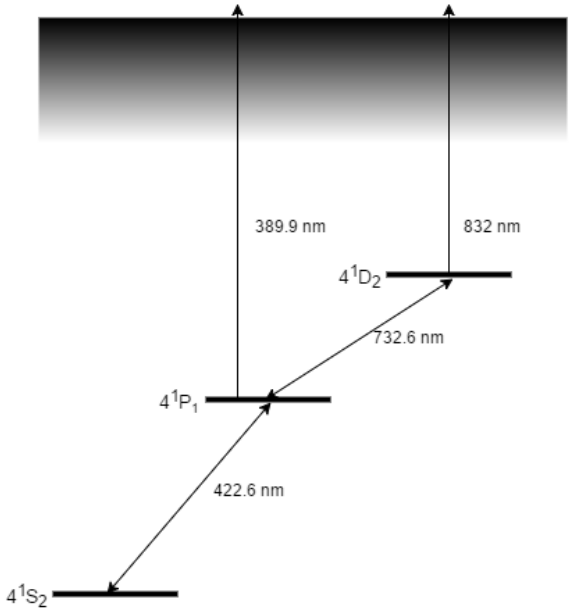

Figure 2.1: Level diagram for CaI showing the energy levels discussed here [1]. The gradient from white to black symbolizes the closely spaced higher states. Note that high lying Rydberg states (n>30) can be ionized by the RF field of the ion trap [43].

the trapping height. Due to a power of 120 µW used for photoionization even the 0.3% of power expected to hit the trap surface is still a significant amount of photons.

2.3 Energy levels of Ca^+

Once calcium is ionized and trapped we can use laser light to control both the motion and internal electronic state of the ion. The energy levels of $^{40}Ca^+$ are shown in Fig. 2.2. The $4^2S_{1/2} \rightarrow 4^2P_{1/2}$ transition is used for Doppler cooling. Due to the finite branching ration of 6.5% to the $3^2D_{3/2}$ level [48] we use a diode laser at 866.21 nm to repump to the $4^2P_{1/2}$ state. Due to the short lifetime of the $4^2P_{1/2}$ state, one can scatter millions of photons per second on the S-P transition that can be collected either by a PMT or a camera. This can be used to discriminate whether the ion is in the S or the $D_{5/2}$ state. In $^{40}Ca^+$ the $4^2S_{1/2} \rightarrow 3^2D_{5/2}$ clock transition is commonly used to define the qubit. We define $4^2S_{1/2} = |1\rangle$ and $3^2D_{5/2} = |0\rangle$. The $3^2D_{5/2} \rightarrow 4^2P_{3/2}$ transition at 854 nm is used to repump the $3^2D_{5/2}$ state after an experiment or to broaden the transition to reduce the lifetime during resolved sideband cooling.

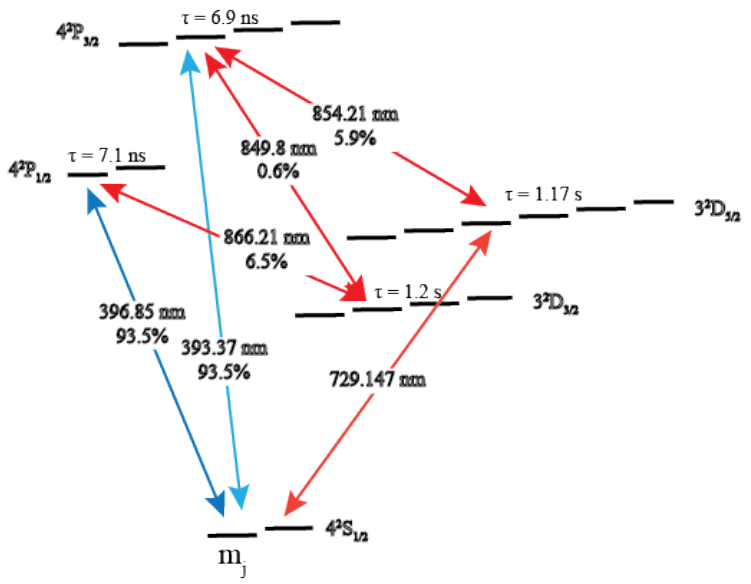

Figure 2.2: Energy level diagram of Ca^+ with an applied magnetic field. Data used to create this graph can be found in [45][46][47][48][49]

2.4 Doppler cooling of trapped ions

Reducing the kinetic energy or temperature of trapped atoms is critical for precision spectroscopy or to improve the fidelity of quantum gates. With laser light, it was first successfully demonstrated in 1978 [50][51] and has been an integral part of neutral atom and ion trapping experiments ever since [29].

We consider an ion trapped along the axial direction of the trap, oscillating with a secular or trap frequency ν_a. It does not experience micromotion along this direction, which would complicate the dynamics since there are no changing electric fields to drive the ion. As a result, the velocity of the ion follows $v = v_0 \cos(\omega_a t)$. Typically, Doppler cooling is performed on a fast cycling transition with a decay rate Γ on the order of MHz. In this case $\Gamma \gg \nu_a$, meaning that one photon absorption and emission cycle occurs while the velocity of the ion does not change significantly as compared to its velocity. Each cycle transfers a momentum of $\Delta p = \hbar\vec{k}$ from the photon to the atom during the absorption, while the emission delivers a similar momentum kick. The direction of the emitted photon is randomly distributed into the entire solid angle, so averaging over multiple events results in no preferential momentum transfer. But there is still a random walk in momentum space as this process is happening in discrete steps. The average force on the ion is therefore

$$F(v) = \hbar k \Gamma \rho_{ee} \,. \tag{2.9}$$

Where ρ_{ee} is the excited state probability [52]

$$\rho_{ee} = \frac{s/2}{1 + s + \left(\frac{2(\Delta - \vec{k}\vec{v})}{\Gamma}\right)^2} \tag{2.10}$$

with the laser detuning $\Delta = \omega_L - \omega_0$, we introduce the saturation parameter $s = 2|\Omega|^2/\Gamma^2$ with an on-resonance Rabi frequency Ω.

For small velocities we can linearize $F(v) \approx F(0)(1+\kappa v)$ with the average force for $v = 0$ of,

$$F(0) = F_0 = \hbar k \Gamma \frac{s/2}{1 + s + \left(\frac{2\Delta}{\Gamma}\right)^2} \tag{2.11}$$

and the friction coefficient

$$\kappa = \frac{8k\Delta/\Gamma^2}{1 + s + \left(\frac{2\Delta}{\Gamma}\right)^2} \,. \tag{2.12}$$

From this we can calculate the cooling rate $\dot{E}_c = F_0 \kappa \langle v^2 \rangle$.

The heating rate $\dot{E}_h$ is due to the random distribution of momentum kicks resulting from the absorption and emission of photons by the ion. We equate both cooling and heating rate to find the ion temperature [29]

$$T = \frac{\hbar\Gamma}{8k_B}(1+\xi)\left((1+s)\frac{\Gamma}{2\Delta} + \frac{2\Delta}{\Gamma}\right) \tag{2.13}$$

which has a minimum for $\Delta = \frac{\Gamma\sqrt{1+s}}{2}$. This minimum is called the Doppler temperature and is [29]

$$T_{\mathrm{D}} = \frac{\hbar\Gamma\sqrt{1+s}}{4k_B}(1+\xi) \,. \tag{2.14}$$

The factor $(1+\xi)$ originates from the fact emission and absorption have the same rate but different directionality. For Dipole radiation as is the case for the $4^2S_{1/2} \rightarrow 4^2P_{1/2}$ transition $\xi = \frac{2}{5}$.

For $^{40}\mathrm{Ca}^+$, $\Gamma = 22.4\,\mathrm{MHz}$, which yields a Doppler temperature of $T_{\mathrm{D}} = 0.5\,\mathrm{mK}$.

2.5 Rabi oscillations

If the spontaneous emission becomes small, the atomic levels may undergo a coherent dynamics when irradiated with laser light. In the simplest case of dynamics restricted to two levels, the dynamics exhibit so-called Rabi oscillations. By shining in and applying the light field for a set amount of time it is possible to transfer population from one state to another. This is often used to perform single qubit gates or for state preparation. Here we will use it to assess the kinetic energy of the ions and thus to measure the heating rate of the ion motion $\dot{n}$. For our experiments, we drive Rabi oscillations on the $4^2S_{1/2} \rightarrow 3^2D_{5/2}$ transition

with the transition frequency ω_0.

The Hamiltonian $H = H_0 + H_I$ of a trapped ion driven by a single mode laser along the trap axis x_i can be divided into the Hamiltonian H_0 describing the kinetic energy and electronic structure of the atom, and the one describing the laser-atom interaction H_I [53][54][55]

$$\begin{array}{ll} H_0 & = \frac{p^2}{2m} + \frac{1}{2}m\omega_i^2 x^2 + \frac{1}{2}\hbar\omega_0\sigma_z \\ H_I & = \frac{1}{2}\hbar\Omega(\sigma^+ + \sigma^-)\left(e^{-i(kx_i-\omega_L t+\phi)} + e^{i(kx_i-\omega_L t+\phi)}\right) \end{array} \tag{2.15}$$

For an atomic transition with a long lifetime and a Rabi frequency $\Omega \ll \omega_i$, we resolve individual sidebands, that is transitions $|S,n\rangle \rightarrow |D,m\rangle$ between different motional states n,m of the ion. In this case, we can neglect transitions to other motional states.

The Hamiltonians in 2.15 can be expressed in terms of creation and annihilation operators $a^\dagger, a$. If we also perform the rotating wave approximation, we find [54]

$$\begin{array}{ll} H_0 = & \hbar\omega_i\left(a^\dagger a + \frac{1}{2}\right) + \frac{1}{2}\hbar\omega_0\sigma_z \\ H_1 = & \frac{1}{2}\hbar\Omega\left(e^{i\eta(a+a^\dagger)}\sigma^+ e^{-i\omega_L t} + e^{-i\eta(a+a^\dagger)}\sigma^- e^{i\omega_L t}\right) . \end{array} \tag{2.16}$$

With the wavefunction

$$\Psi(t) = \sum_{n=0}^{\infty}(C(t)_{S,n}|S,n\rangle + C(t)_{D,n}|D,n\rangle) . \tag{2.17}$$

We also define the Lamb-Dicke factor

$$\eta = kx_0 = k\sqrt{\frac{\hbar}{2m\omega}} . \tag{2.18}$$

We transform into the interaction picture with $U = e^{iH_0 t/\hbar}$, the interaction Hamiltonian $H_I = U^\dagger H U$ reads

$$H_I = \frac{1}{2}\hbar\Omega\left(e^{i\eta(\hat{a}+\hat{a}^\dagger)}\sigma^+ e^{-i\Delta t} + e^{-i\eta(\hat{a}+\hat{a}^\dagger)}\sigma^- e^{i\Delta t}\right) \tag{2.19}$$

with $\hat{a} = ae^{i\omega_i t}$ and the detuning $\Delta = \omega_L - \omega_0$. This Hamiltonian can be interpreted in the following way. Intuitively, the ion motion in the laboratory frame results in a frequency modulation of the laser field with the trap frequency in the ions frame of reference. As a result we can drive sideband transitions, that is a transition from $|S\rangle \rightarrow |D\rangle$, which changes the motional state of the ion where the energy difference $\hbar(\omega_L - \omega_0)$ is either taken from, given to the motional energy of the ion.

The coefficients in 2.17 can be found by solving the Schrödinger equation $i\hbar\delta\Psi/\delta t = H_I\Psi$ to be[55]

$$\begin{array}{ll} \dot{C}_{S,n} = & -i^{1-|n-m|}e^{i\delta t}\Omega_{m,n}C_{D,m} \\ \dot{C}_{D,m} = & -i^{1+|n-m|}e^{-i\delta t}\Omega_{m,n}C_{S,n} . \end{array} \tag{2.20}$$

Here $\delta = \Delta - (m-n)\omega_i$ is the detuning from the transition $|S,n\rangle \rightarrow |D,m\rangle$ and $\Omega_{m,n}$ the Rabi frequency [55]

$$\begin{aligned}\Omega_{m,n} &\equiv \Omega|\langle m|e^{i\eta(a+a^\dagger)}|n\rangle| \\ &= \Omega e^{-\eta^2/2}\sqrt{\tfrac{n_<!}{n_<!}}\eta^{|n-m|}L_{n_<}^{|n-m|}(\eta^2)\end{aligned} \tag{2.21}$$

with $n_<(n_>)$ the lesser(greater) of n and m and the generalized Laguerre polynomial L_n^α.

$$L_n^\alpha(X) = \sum_{m=o}^{n}(-1)^m \begin{Bmatrix} n+\alpha \\ n-m \end{Bmatrix} \frac{X^m}{m!} \,. \tag{2.22}$$

The solutions of 2.20 show an oscillatory behavior of the population of the two states. When the laser is on resonance ($\delta = 0$) we find [55]

$$\Psi(t) = \begin{pmatrix} \cos(\Omega_{n,m}t) & -ie^{i\frac{\pi}{2}|n-m|}\sin(\Omega_{n,m}t) \\ -ie^{i\frac{\pi}{2}|n-m|}\sin(\Omega_{n,m}t) & \cos(\Omega_{n,m}t) \end{pmatrix}\Psi(0) \tag{2.23}$$

We typically apply three different kinds of laser-ion interactions. Transitions with $n - m < 0$ are called blue sideband transitions and add motional energy to the ion. In the case of $n-m > 0$ we reduce the motional energy of the ion, we call them red sideband transitions. For carrier transitions $n - m = 0$ and the motional state of the ion is unaffected.

In the Lamb-Dicke limit, i.e. $\eta \ll 1$, we can expand 2.21 and 2.19 in η. The interaction Hamiltonian then reads

$$H_I = \frac{1}{2}\hbar\Omega\left[\sigma^+\left(1 + i\eta(\hat{a}^\dagger + \hat{a})\right) + \sigma^-\left(1 - i\eta(\hat{a}^\dagger + \hat{a})\right)\right] + \mathcal{O}(\eta^2)\,. \tag{2.24}$$

were the first term is the Rabi carrier transition and the η-depended terms describe red and blue sidebands. From Eq. 2.21, we find for the Rabi frequency of the carrier transition

$$\Omega_{n,n} = \Omega(1 - \eta^2 n) \tag{2.25}$$

with an on resonance interaction Hamiltonian

$$H_I = \frac{1}{2}\hbar\Omega_{n,n}(\sigma^+ + \sigma^-)\,. \tag{2.26}$$

2.5.1 Temperature measurement with Rabi flops

From 2.25 we see that the carrier Rabi frequency depends on the motional state of the ion. We utilize this to measure the temperature of the ion. We assume the ion is in a thermal state with a temperature [29]

$$T = \frac{\hbar\omega_i}{k_B \ln\left(\frac{\bar{n}+1}{\bar{n}}\right)}\,, \tag{2.27}$$

where $\bar{n}$ is the mean occupation number of the harmonic motion.

The probability, to find the ion in the Fock sate $|n\rangle$, is [29]

$$P(n) = \frac{\bar{n}^n}{(\bar{n}+1)^{n+1}} \,. \tag{2.28}$$

We then perform Rabi flops to determine the mean motional occupation number. For the Rabi flops, we prepare the ion in the ground state and switch on a resonant laser for a time t. After the laser pulse, we detect whether the ion is in state $|S\rangle$ or $|D\rangle$. We repeat the experiment multiple times, typically one hundred times, to determine the excited state probability $P_D = 1 - P_S$. The experimental sequence is then repeated for different pulse lengths t.

It follows from 2.25 that if we perform Rabi flops, for each instance of the experiment the ion will experience a different Rabi frequency depending on which Fock state the ion is in. This results in a reduction of contrast of the Rabi oscillations – we do not fully reach $P_D = 1$. Specifically, the probability of finding the ion in $|S\rangle$ is

$$P_S(t) = \sum_{n=0}^{\infty} P(n) cos^2\left(\frac{\Omega(1-\eta^2 n)t}{2}\right) \,. \tag{2.29}$$

By fitting the resulting curve with $\bar{n}$ as a parameter we can then find the corresponding temperature of our ion.

This method can also be used to measure a heating rate $\dot{\bar{n}}$ by varying the wait time after cooling the ion before we measure the Rabi flop.

2.5.2 Sideband transitions

With a laser detuning of $\delta = (m-n)\omega_i$ we drive sideband transitions. Transitions for which the final state has more (less) motional quanta are called blue (red) sidebands. Sideband transitions can be used for further reduce the temperature of the ion after Doppler cooling, detection of micromotion, and for a momentum state detection as described in Sec. 2.5.1. For highly occupied motional states the interaction strength of the first and second sideband is larger than for the carrier transition [30], a characteristic we will use later.

Assuming the Lamb-Dicke regime, the interaction Hamiltonian for the red sideband is [29]

$$H_{I,rsb} = \frac{\hbar}{2} i\Omega_{n-1,n}(\hat{a}\sigma^+ + \hat{a}^\dagger\sigma^-) \,. \tag{2.30}$$

When we compare 2.30 to 2.25, we see that for low or medium motional states n, the coupling on the sideband is weaker than on the carrier transition as we find the Rabi frequency by expanding 2.21

$$\Omega_{n-1,n} = \eta\sqrt{n}\Omega \,. \tag{2.31}$$

The red sideband can be used to further cool the ion after Doppler cooling [29]. A laser resonant with the red sideband is detuned by $\delta = \omega_i$ from the carrier and $\delta = 2\omega_i$ from the

heating blue sideband. As such these transitions are suppressed. In the Lamb-Dicke regime, the ion will also predominantly decay on the carrier transition. For calcium we also shine in a laser on the $3^2D_{5/2} \rightarrow 4^2P_{3/2}$ transition to broaden the line width of the $3^2D_{5/2}$ energy level, which increases the rate of decay and speeds up the cooling process.

For blue sideband transitions, the interaction Hamiltonian is [29]

$$H_{I,bsb} = \frac{\hbar}{2} i\Omega_{n+1,n}(\hat{a}^\dagger \sigma^+ - \hat{a}\sigma^-) \,. \tag{2.32}$$

And for the Rabi frequency from the expansion of 2.21

$$\Omega_{n+1,n} = \eta\sqrt{n+1}\Omega \,. \tag{2.33}$$

We can use the dependence of coupling strength on the motional state of the ion to measure the ion temperature [29]. For this, we measure the excitation probability for a laser pulse resonant with the blue and red sidebands. Then we calculate the ratio of these probabilities from Eq. 2.31 and Eq. 2.33

$$R = \frac{P_D^{\mathrm{rsb}}}{P_D^{\mathrm{bsb}}} = \frac{\bar{n}}{\bar{n}+1} \,. \tag{2.34}$$

When solving this equation for the mean motional occupation number we find

$$\bar{n} = \frac{R}{1-R} \,. \tag{2.35}$$

This method of measuring $\bar{n}$ is most sensitive for small $\bar{n}$ such that $\eta\bar{n} \ll$. If $\eta\bar{n}$ becomes substantial for thermal states it is usually easier to measure carrier Rabiflops instead because the carrier resonance does not depend on the trap frequency ω_i.

3 Ion as a circuit element

An ion in a Paul trap is located in the center between the trap electrodes. It oscillates in the harmonic potential, inducing an image current as it moves towards or away from the electrodes. The ion also experiences a force from any voltage applied to the electrodes. Keeping this in mind, we can model the trapped ion as an LC circuit.

3.1 The ion as an LC circuit

When evaluating how trapped ions interact with circuit elements, it is advantageous to model the trapped ion as a series LC-circuit. We consider the case that the ion is trapped between the plates of a capacitor with an applied driving voltage V as seen in Fig. 3.1a. In this case, the movement of the ion induces a displacement current in the capacitor plates [56]

$$I = \frac{ev_y\kappa}{d} = \frac{ev_y}{D_{\text{eff}}} \,. \tag{3.1}$$

Here, $\kappa \approx 1$ is a geometric factor that depends on the actual electrode structure of the ion trap and D_{eff} the effective distance resulting from this geometric factor and the distance of the trap electrodes d. We imagine the ion is held in place by a massless, neutral spring with a spring constant k and write the ion's equation of motion

$$m\ddot{y} + ky = \frac{eV}{D_{\text{eff}}} \,. \tag{3.2}$$

With Eq. 3.1 we can write Eq. 3.2 as,

$$\frac{mD_{\text{eff}}^2}{e^2}\frac{dI}{dt} + \frac{mD_{\text{eff}}^2\omega^2}{e^2}\int I dt = V \,. \tag{3.3}$$

Equation 3.3 relates the current induced by the ion motion to the voltage between the trap electrodes. Comparing Eq. 3.3 with those of an LC circuit we find the equivalent inductance

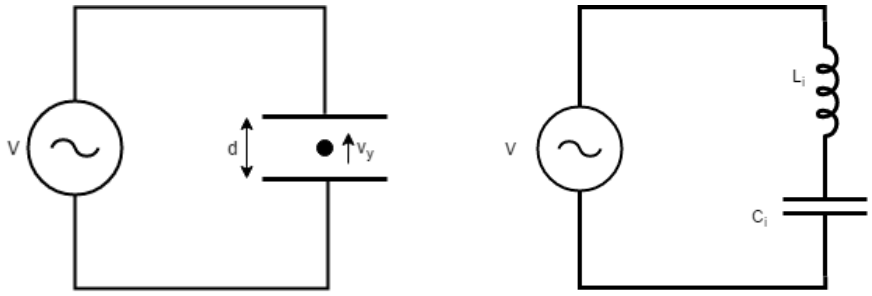

(a) A charged particle is trapped between the plates of a capacitor

(b) The ion can be modeled as a series LC circuit

Figure 3.1: Describing an ion as a series LC circuit

L_i and capacitance C_i [57]

$$L_i = \frac{mD_{\text{eff}}^2}{e^2}, \qquad C_i = \frac{1}{L_i\omega^2} \qquad \text{and} \qquad \omega_i = \frac{1}{\sqrt{L_iC_i}}\,. \tag{3.4}$$

In a series RLC circuit, the dampening rate is given by $\alpha = \frac{R}{2L}$. In the case of the ion the attenuation of the secular motion can be achieved via Doppler cooling. As a result we can model the laser-cooled ion as a series RLC circuit. To find an equivalent ion resistance R_i we take the cooling rate near the Doppler cooling limit [58],

$$\frac{dE}{dt} = \frac{I\sigma_0}{\hbar\omega_L}\frac{\hbar^2k^2}{2m}\left(-\frac{2E}{\hbar\gamma}+1\right), \tag{3.5}$$

with the recoil energy $R = \frac{\hbar^2k^2}{2m}$, laser intensity I, resonant scattering cross section σ_0, and decay rate γ. The laser frequency is tuned to $\omega_L = \omega_0 - \frac{\gamma}{2}$ for optimal cooling and the laser intensity is adjusted for optimal Doppler cooling. Next we rewrite Eq. 3.5 to

$$\frac{d}{dt}\left(E-\frac{\hbar\gamma}{2}\right) = -\dot{N}_s\frac{2}{\hbar\gamma}\frac{\hbar^2k^2}{2m}\left(E-\frac{\hbar\gamma}{2}\right)\,. \tag{3.6}$$

Here $\dot{N}_s$ is the on resonance scattering rate.

By equating the energy decay rate in an RLC circuit with the energy decay of a Doppler cooled ion we find for the equivalent resistance R_i [25]

$$R_i = L_i\dot{N}_s\frac{2}{\hbar\gamma}\frac{\hbar^2k^2}{2m}\,. \tag{3.7}$$

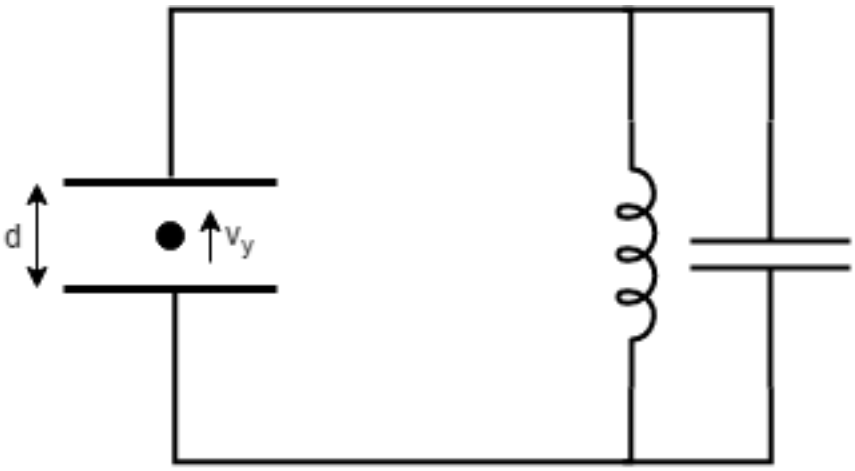

Figure 3.2: Schematic of the ion connected to a LC resonator

3.2 Coupling ions and LC resonators

We now consider coupling the ion motion to an LC-resonator. Both the ion and the resonator are harmonic oscillators described by a Hamiltonian $H = \hbar\omega_i(a_i^\dagger a_i + \frac{1}{2})$. When those harmonic oscillators are coupled the resulting interaction Hamiltonian is

$$H_I = \hbar g(a_1^\dagger a_2 + a_1 a_2^\dagger) \tag{3.8}$$

with a coupling constant g. The coupling constant describes after what time $\tau_{\text{swap}} = \frac{\pi}{g}$ a population transfer from one oscillator to the other has happened.

To calculate the coupling constant, we view the ion as a charged mechanical oscillator. Its interaction in an electrical field is described by $U_{\text{ion}} = -exE$ as is displaced from its equilibrium by x. The electric dipole moment of the ion is then $\mu = ex$ and the dipole operator

$$\mu = e\sqrt{\frac{\hbar}{2m\omega}}(a^\dagger + a)\,. \tag{3.9}$$

From this follows that the electric dipole moment of the motion of the trapped ion is [19]

$$\mu_{el} = e\sqrt{\frac{\hbar}{2m\omega}}\,. \tag{3.10}$$

The zero-point fluctuation of voltage and current of our resonator satisfy $Z = \frac{V_0}{I_0}$, with Z the characteristic impedance of the oscillator. The voltage fluctuations can couple to the trapped ion via an electric field. The electric field produced is $E = \frac{V}{D_{\text{eff}}}$. As [59]

$$V_0 = \omega\sqrt{\frac{\hbar Z}{2}} \tag{3.11}$$

and with the previously mentioned interaction strength of the electric dipole we find

$$U_{\mathrm{el}} = \frac{V_0 \mu_{\mathrm{el}}}{D_{\mathrm{eff}}} = \frac{\omega \mu_{\mathrm{el}}}{D_{\mathrm{eff}}} \sqrt{\frac{\hbar Z}{2}} \,. \tag{3.12}$$

From 3.10 and 3.12 we can now calculate the coupling constant in 3.8 [19]

$$g = \frac{\omega}{2} \sqrt{\frac{e^2 L}{m D_{\mathrm{eff}}}} = \frac{\omega}{2} \sqrt{\frac{L}{L_{\mathrm{ion}}}} \,. \tag{3.13}$$

Here we use the ion equivalent inductance from 3.4 to find that the coupling constant depends on the square root of the ratio of ion and resonator inductance. An easy way to increase the coupling is to trap more ions, which increases the coupling with the square root as according to Eq. 3.4 the inductance decreases with the square of the charge and only increases linearly with the mass. The inductance of the resonator is already maximized by choosing a solenoid geometry with a low capacitance (see Sec. 6). The final accessible tuning knob is the effective distance of the ion from the trap electrodes which can be reduced by miniaturization or trap geometry.

3.3 Heating and cooling the LC resonator

For the ultimate goal of building a hybrid quantum system, the occupation number of both the ion and the resonator need to be low enough to allow for the exchange of single excitations without a significant heating from coupling to the bath. This is very challenging, hence we focus first on the exchange dynamics of using a Doppler cooled ion to cool a mode of the resonator. As the Doppler cooling limit is already much lower than the temperature of typical cryostats, this is already a very attractive goal (see Sec. 2.4).

For these studies, the coupling constant g is an important property of the system. We need to be in the strong coupling regime, analogous to cavity QED systems [60], such that the coupling constant is the dominating interaction, much stronger than the coupling of the resonator mode or the trapped ion to the environment. A strong coupling to the environment will make the observation of any interaction between the ion and the resonator mode hard as the system returns to the equilibrium state.

If we assume an effective distance of $D_{\mathrm{eff}} = 100\,\mu\mathrm{m}$, a resonance frequency of $\omega = 2\pi \times 2\,\mathrm{MHz}$ and a resonator inductance $L = 5\,\mathrm{mH}$, the coupling constant is $g \approx 2\pi \times 350\,\mathrm{Hz}$. We compare this coupling rate to the heating rate of the resonator modes to the environment of $\gamma = \frac{\omega}{Q}$. For an in this work demonstrated quality factor of $Q = 10^5$, the resonant mode heating rate is $\gamma = 2\pi \times 20\,\mathrm{Hz}$. Even lower heating rates of the ion's motion are possible in cryogenic surface traps for these trapping heights. From this estimate, we find that we can cool the resonator mode by more than an order of magnitude if we continuously couple to the cooled trapped ion.

The occupation number of the resonator at a time t, for example after cooling it due to coupling to an ion, is described by [25]

$$\bar{n}_{\mathrm{LC}}(t) = \bar{n}_{\mathrm{LC}}(0)e^{-\gamma t} + \bar{n}_{\mathrm{bath}}(1 - e^{-\gamma t}) \,. \tag{3.14}$$

The first term describes the decays of excitation present in the resonator after cooling it with a trapped ion, while the second term describes the equilibration with the environment. $\bar{n}_{\mathrm{bath}} = \frac{kT_{\mathrm{bath}}}{\hbar\omega} \approx 32,000$ is the occupation number of the bath for at a typical temperature of 4 K. For short times $t \ll \frac{1}{\gamma}$ the heating rate is $\frac{\gamma k T_{\mathrm{bath}}}{\hbar\omega} \approx 1\,\mathrm{MHz}$. If we want to perform quantum gates, which take $\mathcal{O}(10\,\mu\mathrm{s})$, we need to reduce the heating rate. A less fragile experiment is the measurement of the temperature after cooling the resonator mode with an ion. The heating rate can be reduced in multiple ways, such as a cryostat with a lower base temperature, a smaller scale trap, more ions, or a higher Q resonator, allowing us eventually to perform coherent exchange of excitation between the two harmonic oscillators.

We can calculate the dampening rate in 3.14 with the previously found coupling constant. In the case of large occupation numbers, the exchange of energy between the resonator mode and the ion is an incoherent process. We remind ourselves of the circuit picture of the ion and evaluate the case that the resonator damps the ion motion, which occurs at the same rate as the heating of the ion motion. The induced current I flows through an impedance Z inducing a voltage $V = I\,\mathrm{Re}\,Z$ in the electrode [28]. The voltage induces an electric field $E = I\,\mathrm{Re}(Z)/D_{\mathrm{eff}}$ resulting in a force

$$F = -\frac{eI\,\mathrm{Re}(Z)}{D_{\mathrm{eff}}} \,. \tag{3.15}$$

The force depends on the velocity and is, therefore, a dissipative force,

$$F = -m\gamma\dot{y} \,, \tag{3.16}$$

with a dampening constant γ. From 3.15 and 3.16 we find [28]

$$\gamma = \frac{\mathrm{Re}(Z)e^2}{D_{\mathrm{eff}}^2 m} \,. \tag{3.17}$$

We now calculate the dampening constant in terms of parameters easily measured in our experiment. With substituting the expressions from 3.4, 3.13, and the expression for the real impedance of a parallel LC circuit, $\mathrm{Re}(Z) = \omega LQ$, 3.17 simplifies to

$$\gamma = \frac{g^2 Q}{\omega} \,. \tag{3.18}$$

An experiment that is accessible with a base temperature of 4 K and a lower quality factor resonators than would be necessary for coherent excitation exchange, is to measure the heating of the ion from a resonator mode. The base temperature of the ion is $T_D = 0.5\,\mathrm{mK}$,

four order of magnitude lower than the resonator bath temperature. This results in a heating described by 3.14. For the parameters detailed here we find an ion heating rate of $\frac{\hbar\omega}{\gamma k T_{\text{bath}}} \approx 0.4\,\mu$ on resonance. This heating rate is orders of magnitude larger than those typically found in surface traps with similar trapping heights and thus easily detectable.

4 Trap design

In this chapter, we will focus on the simulation of the trap potential before going into detail of the trap design and the coupling electrode. We want to optimize both the trap design and the coupling electrode to maximize the coupling constant.

4.1 Boundary element method simulations

From examples of previously built surface traps and an understanding of electrostatics, one can guess a trap design and values for RF and DC voltages that traps ions. An example of such voltages is positive voltages at the electrodes on either side of the trapping location and a negative voltage on the electrode closest to the desired trapping position for the positively charged ion. While this approach has been taken in early surface trap experiments, it is severely limited in terms of independent control over the homogeneous and quadrupolar electric field components.

Ideally, we have full control over the electric field components and also know and control the orientation of the trap axis. For this goal, we numerically solve for the trap potential each electrode generates via a boundary element method (BEM) and then compose the desired potential out of these [61] [62]. As the first step, we draw the ion trap using Autocad in the dxf file format with each electrode assembled using the Autocad command 3Dface. We estimate where the ion will be trapped and then use the BEM toolkit [61] to calculate the electric potential created in that cube by applying 1 V to each of the electrodes and 0 V to all others.

With those solutions of the Laplace equation, one can then quickly calculate the resulting trap potential for arbitrary voltage combinations. Our goal is to find the set of voltages that creates a specific harmonic or quadrupolar components. Towards this goal we decompose the specific solutions for each electrode i, $\Phi_i(r, \Theta, \varphi)$, into spherical harmonics [63].

$$\Phi(r,\Theta,\varphi)=\sum_{l=0}^{\infty}\sum_{m=-l}^{l}(A_{lm}r^{l}+B_{lm}r^{-(l+1)})Y_{lm}(\Theta,\varphi)\,. \tag{4.1}$$

The coefficients B can be determined from the boundary conditions. The potential in the trap center is finite and hence the coefficients B_{lm} vanish. The coefficients A_{lm} can be calculated with

$$A_{lm}=\int d\Omega\, Y^{*}_{lm}(\theta,\varphi)\Phi(\theta,\varphi) \tag{4.2}$$

with the spherical harmonics

$$Y_{lm}(\theta,\varphi)=\sqrt{\frac{2l+1}{4\pi}\frac{(l+m)!}{(l-m)!}}P_{l}^{m}(cos\theta)e^{im\varphi} \tag{4.3}$$

where P_l^m is the associate Legendre polynomials.

Surface traps we use do not have spherical symmetry and it is more convenient to switch to Cartesian coordinates. We then further simplify the expansion by changing the basis of the spherical harmonics to a single index real basis with the following mapping

$$Y_j=\left\{\begin{array}{ll} r^{l_j}Y_{l_j,0} & \text{if } m_j=0\\ \frac{1}{\sqrt{2}}r^{l_j}((-1)^{m_j}Y_{l_j,m_j}+Y_{l_j,-m_j}) & \text{if } m_j>0\\ \frac{i}{\sqrt{2}}r^{l_j}(Y_{l_j,-m_j}-(-1)^{m_j}Y_{l_j,m_j}) & \text{if } m_j<0\end{array}\right\} \tag{4.4}$$

and the new expansion coefficients

$$M_j=\left\{\begin{array}{ll} A_{l_j,0} & \text{if } m_j=0\\ \frac{1}{\sqrt{2}}((-1)^{m_j}A_{l_j,m_j}+A_{l_j,-m_j}) & \text{if } m_j>0\\ \frac{i}{\sqrt{2}}(A_{l_j,m_j}-(-1)^{m_j}A_{l_j,-m_j}) & \text{if } m_j<0\end{array}\right\}\,. \tag{4.5}$$

In 4.4 and 4.5, l_j and m_j provide a map from the indices j to the indices l,m, with

$$l_j=\left\{\begin{array}{ll} 0 & \text{if } j=0\\ \lfloor\sqrt{j-1}\rfloor & \text{if } j>0\end{array}\right\} \tag{4.6}$$

and

$$m_j=j-(2l_j+1)-l_j(l_j-1)\,. \tag{4.7}$$

This mapping results in the following expansion of the simulated potential of electrode i per volt where we neglect orders $l=3$ and higher

$$\begin{aligned}\tfrac{\Phi_i(x,y,z)}{V}= \;& M_{1,i}+M_{2,i}\left(\tfrac{x}{r_0}\right)+M_{3,i}\left(\tfrac{y}{r_0}\right)+M_{4,i}\left(\tfrac{z}{r_0}\right)+M_{5,i}\left(\tfrac{xy}{2r_0^2}\right)+M_{6,i}\left(\tfrac{zy}{2r_0^2}\right)\\ & +M_{7,i}\left(\tfrac{2z^2-x^2-y^2}{2r_0^2}\right)+M_{8,i}\left(\tfrac{zx}{2r_0^2}\right)+M_{9,i}\left(\tfrac{x^2-y^2}{2r_0^2}\right)+O(r^3)\,.\end{aligned} \tag{4.8}$$

The first term corresponds to a gauge transformation, while the terms $M_2 - M_4$ are the dipole fields, which can be used to apply a homogeneous field at the ion location in order to apply a force that displaces the ion. Terms $M_5 - M_9$ are the quadrupolar contributions to the potential. They provide the harmonic potentials for trapping the ion and can rotate the potential in the Cartesian coordinates.

We repeat the process for all N electrodes of a trap.

For a set of applied voltages $\vec{V}$ the resulting potential can be calculated from

$$\Phi(x, y, z) = \sum_{j=1}^{9} Y_j M_j = \sum_{i=1}^{N} \sum_{j=1}^{9} M_{j,i} V_i Y_j \, . \tag{4.9}$$

We would like now to find the voltages, which generate a specific set of multipoles $\vec{M}$. For this we calculate the inverse of matrix $\mathbf{M}$ as

$$\vec{V} = \mathbf{M}^{-1} \vec{M} \, . \tag{4.10}$$

Due to the need to compensate a specific stray electric field or change the axial trapping frequency, typically we want to know the voltage vector that just affects one of the multipole coefficients so that we can change each multipole independently. We call these control vectors or $\vec{C_j} = \{0, .., x_j, .., 0\}$ with $x_j = 1$, which can be easily calculated from 4.10 by setting $\vec{M} = \vec{C_j}$. Due to the superposition principle for electric potentials, we can so exactly define the potential we want to apply.

We minimize the voltages needed for any set of multipoles[1]. For this purpose, we calculate the Kernel of $\mathbf{M}$, that is the subspace of $\mathbf{M}$, for which two voltage vectors $\vec{V}$, whose only difference is in that subspace $\mathbf{K}$, map to the same multipole vector $\vec{M}$

$$\mathrm{Ker}(\mathbf{M}) = \{\vec{k_i} \in \mathbf{K}^n \mid \mathbf{M}\vec{k_i} = \vec{0}\} \, . \tag{4.11}$$

Where $\vec{k_i}$ is the orthonormal basis of that subspace $\mathbf{K}$

We then subtract linear combinations of $\vec{k_i}$ so that we minimize the norm of the control vectors $\vec{C_j}$.

$$\min \left\{ \| \vec{C_j} - \sum_{i=1}^{N-9} \lambda_i \vec{k_i} \| \right\} \, . \tag{4.12}$$

If after this voltage minimization step, the voltages may still be considered too large, a further reduction can be achieved by only allowing for the control of one of the quadrupole

[1]Typical traps we use have far more electrodes than multipoles we want to control. This is the case as we have multiple trapping regions as fabrication defects or local charges in specific locations might make a particular region of the trap undesirable for trapping. With multiple trapping regions, we can avoid such locations. As such the problem of finding the control vectors for the multipoles is underconstrained. A constraint not included in the simulations is the amplitude of the voltages that the voltage sources can provide.

terms responsible for providing axial confinement and allowing an arbitrary magnitude for the other five terms. One disadvantage is that this will lead to an uncontrolled orientation of the trap axes and consequently to small uncontrolled changes of the radial trapping frequencies.

In our experimental control software we have reordered and substituted the multipoles in the following way

$$\begin{array}{ll} M_1 & \to C \\ M_2/r_0 & \to -E_y \\ M_3/r_0 & \to -E_z \\ M_4/r_0 & \to -E_x \\ M_5/r_0^2 & \to U_3 \\ M_6/r_0^2 & \to U_4 \\ M_7/r_0^2 & \to U_2 \\ M_8/r_0^2 & \to U_5 \\ M_9/r_0^2 & \to U_1 \end{array} \quad . \tag{4.13}$$

So that

$$\begin{aligned} \Phi(x,y,z) = \; & C + E_x(-x) + E_y(-y) + E_z(-z) \\ & + U1\left(\tfrac{x^2-y^2}{2}\right) + U2\left(\tfrac{2z^2-x^2-y^2}{2}\right) \\ & + U3\left(\tfrac{xy}{2}\right) + U4\left(\tfrac{yz}{2}\right) + U5\left(\tfrac{xz}{2}\right) + O(r^3)\,. \end{aligned} \tag{4.14}$$

Where we choose for E_i units of $\frac{\mathrm{V}}{\mathrm{mm}}$ and for U_i $\frac{\mathrm{V}}{\mathrm{mm}^2}$.

A typical value of $U_2 = 4\frac{\mathrm{V}}{\mathrm{mm}^2}$ results in an axial trapping frequency of 500 kHz. An example of a simulated potential for an F-trap is shown in Fig. 4.1.

4.2 Trap design

To maximize the coupling of the ion to the LC resonator the ion should be as close as possible to the coupling electrode (see Sec. 3.2). Another consideration is to assure that our trap has enough optical access to shine in all the required laser beams mentioned in Sec. 2.3.

Initially, we considered a 3D design, shown in Fig. 4.2. The RF electrodes, as well as the coupling electrodes in this design, are titanium wires while the axial confinement is provided by the electroplated wire mounts. The mounts for the wires would have to be made from a vacuum compatible, insulating material. Due to experience with other trap designs, we choose Macor. It is better machinable than Alumina and stiffer than Peek, two other materials used for this purpose in our group. One difficulty of this design is the optical access. We loose one direction between the wire on the top and the bottom due to the smaller diameter coupling electrodes. In our design, the laser beams would enter under a 45° angle from the top in Fig. 4.2.

Another problem in this design is, that the two coupling electrodes shield the ion from the RF potential. While trapping is still possible, the close distance to the ion and their

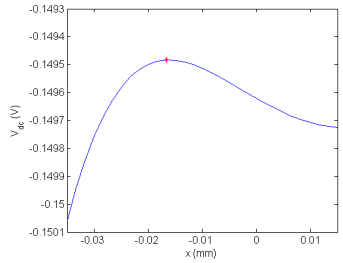

(a) DC potential cut along the x-axis

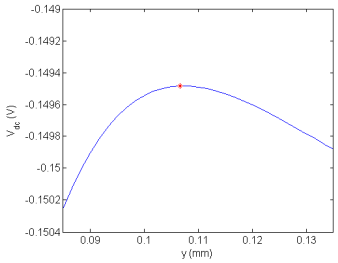

(b) DC potential cut along the y-axis

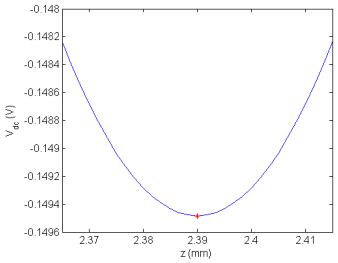

(c) DC potential cut along the z-axis

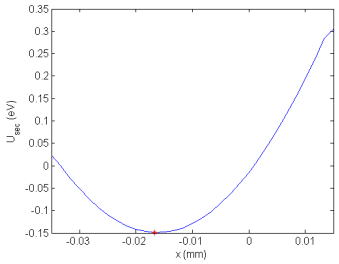

(d) DC and Pseudopotential cut along the x-axis

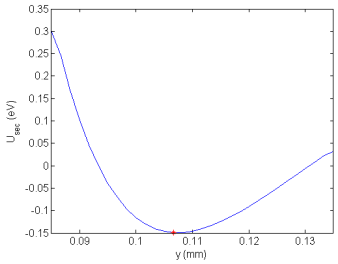

(e) DC and Pseudopotential cut along the y-axis

Figure 4.1: Example of a potential simulation when only applying a RF voltage and the U2 multipole. The red dot shows the ion position. The simulation is for an F-trap, a trap with a trapping height of 107 µm. The trap can be seen in Fig. 4.4a

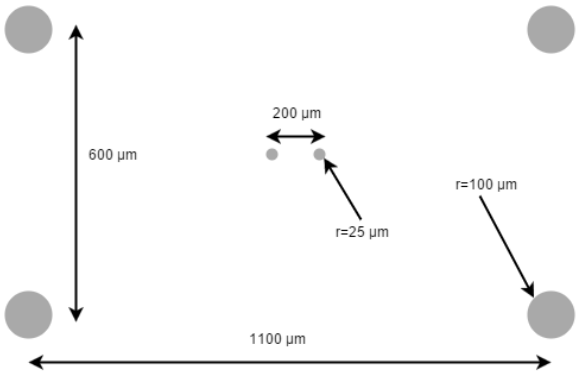

Figure 4.2: Abandoned design of a 3D trap for coupling to the ion. Here shown are the wire positions, the wires themselves would extend out of the page. The trap electrodes were planned to be made of titanium wires. The material was chosen due to the stiffness and thermal contraction properties. The wires are clamped in a ceramic mount. The ceramic mount holding the wires and not shown here is metal coated to act as endcaps, providing axial confinement of the ion. Optical access would exist only from the top or from the bottom of the trap.

relative positions result in a requirement of getting the absolute position correct within better than 10 µm. The high price quote for the fabrication of the parts, the fact that this would be an unproven design with limited optical access lead us to abandon this design in favor of an alternative.

Surface traps have proven to be a good pathway for miniaturization, demonstrating trapping heights as low as 30 µm [37]. For an initial design, we do not have to be as ambitious, as a trapping height of $h \sim 100$ µm would already provide a large enough coupling to conduct initial experiments, while also being in the range of trapping heights commonly used by other experiments in our laboratory.

Besides the trapping height, which relies on the dimensions of the trap electrodes, another important feature is a smooth, constant RF potential along the axis of the trap. To achieve this goal we extend the RF electrode well past the DC electrodes controlling the axial confinement as seen in Fig. 4.3.

Finally, we also need sufficient optical access. Care needs to be taken that no UV or visible light shines on the trap surface to avoid charging [41]. Hence, UV beams need to be send in parallel to the trap surface. One possible obstacle are wire bonds used to connect the trap to the voltage sources. The are arching up from the bonding pads to avoid shorting to the ground plane and can produce scatter when a laser beam hits them. In Fig. 4.3 we can see how the wire bonding pads are arranged in one of the traps used in this work. By placing them on opposite ends of the RF electrode on the two sides we have two clear paths across the trap under a 90° and a 45° angle. The direction along the trap axis can be obstructed by the coupling electrode described in the next section.

4.3 Coupling electrodes

We want to maximize the coupling strength of the ion to the LC-resonator. An important parameter in the coupling is the effective distance D_{eff} (see Eq. 3.13) between the ion and the electrodes attached to the resonator and so decreasing the equivalent inductance of the ion, see 3.4. D_{eff} is the distance of the plates of a perfect parallel plate capacitor that creates an identical field at the ion position for a charge C as the coupling electrodes. In order to minimize D_{eff} we place a 50 µm diameter NbTi wire above the gap between the center and RF electrode of the trap as seen in Fig. 4.4b. This way the ion is trapped slightly to the side of the wire so that none of the light collected by the objective is blocked, as seen in Fig. 4.5a.

Besides increasing the coupling strength of the ion to the LC resonator, the wire also influences the trapping potential. From using the software package Maxwell[2], we determine the capacitance of the coupling wire to the center electrode to be $C_{\text{wire}} \sim 100$ fF, depending on the exact position. In combination with the inductance of the LC circuit, which dominates the impedance at our RF drive frequencies off resonance, this results in 10% of the RF voltage applied to the coupling wire. Due to the high Q of the LC resonator, we assume to be far off

[2]by ANSYS

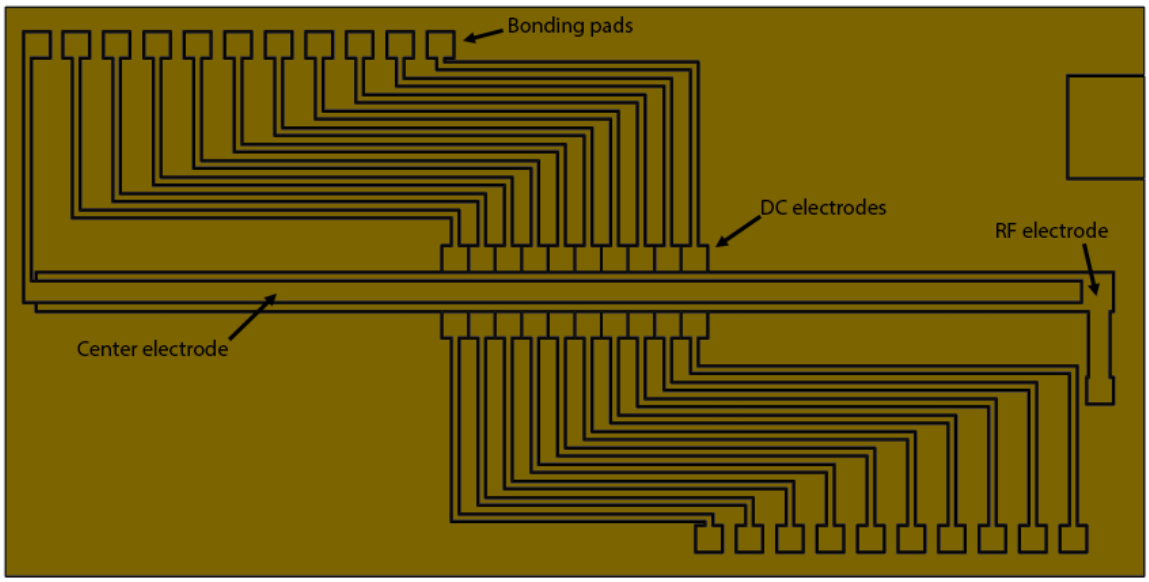

Figure 4.3: Design drawing of an F-trap, a trap with a trapping height of 100 µm. The DC electrodes have a side length of 200 µm. The center electrode is 160 µm thick and the two sides of the RF electrode 60 µm thick.

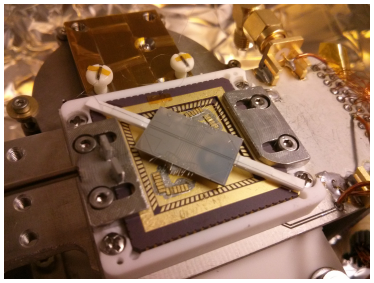

(a) Final assembly of the trap with all wire-bonds and the coupling wire above the trap

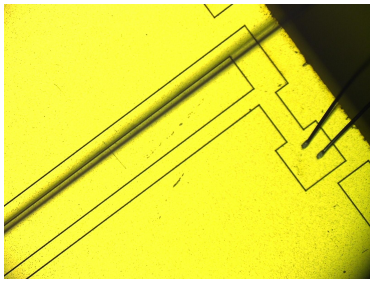

(b) Microscope picture of the wire above the trap. The center electrode is 180 µm wide

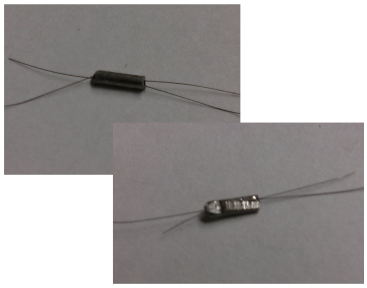

(c) The superconducting contact is made by feeding the wire through a Nb tube and crimping it together

Figure 4.4: Pictures illustrating the construction of the coupling electrode.

resonance with our drive voltage. If we are by chance in resonance with the LC resonator we can slightly modify our helical resonator and change it's resonance frequency. A simulation of the trap potential with these parameters results in a stable trap configuration, but a shift of the trapping height from 80 µm to 85 µm. The secular frequency of the ion is reduced from 3.5 MHz to 3 MHz and from 3.8 MHz to 3.2 MHz for the horizontal and vertical directions respectively. The influence of the wire will increases as the wire height is lowered from the 250 µm used for the analysis here, which will make it necessary to repeat this estimate if the geometry is scaled down in the future.

We strive to position the wire as accurately as possible. Any error in the position will change the trapping potential. To place the wire in the desired position as accurately as possible, we mount it between two posts and keep it under tension. The posts, in turn, are mounted on a translation stage that controls the height. Onto the edge of the CLCC we glue lapped and diced alumina slices of a specific thickness to reach the desired height as seen in Fig. 4.4a. While imaging the trap under a microscope, the wire is slowly brought closer until it touches the alumina spacers. It is aligned horizontally with tweezers and by shifting the CLCC. Then we secure the wire in position with Stycast 1266 epoxy. However, the positioning of the wire is not perfect. By comparing the wire positions with different microscopes the displacement from the desired position seems to be within the width of the electrode gap. One problem is that the microscopes available have a slight angle of the objective with respect to the normal of the sample plane, that differs from microscope to microscope. This results in a slight offset in the position, as we are viewing the projection from the microscope angle. We estimate that the alignment accuracy is about $10 - 20\,\mu\text{m}$ by comparing it to the electrode gap of the Translume traps of 10 µm.

A further improvement for future iterations of this experiment would be to replace the NbTi wired with a copper wire. The NbTi wire is not well thermally anchored and as such has a finite resistance much larger than a comparable thickness copper wire would have(see Sec. 6.1.3).

Calculation of the coupling strength

This electrode configuration seems far removed from a parallel plate capacitor. To find the effective distance D_{eff}, we run a BEM simulation of the trap as discussed in Sec. 4.1. The coupling is calculated for the case that the LC resonator is connected on one side to the wire above the trap and on the other side of the ground plane. We then calculate the potential at the position of the ion, that results from applying a 1 V potential difference between the two coupling electrodes and plot that potential in cuts along the axis of the trapping potential. For a parallel plate capacitor $V = Ed$. Therefore

$$D_{\text{eff}} = \frac{\Delta x_i}{\Delta V} \tag{4.15}$$

for the trap axis i.

For the effective distance D_{eff}, we find 334 µm where we assumed the wire height to be

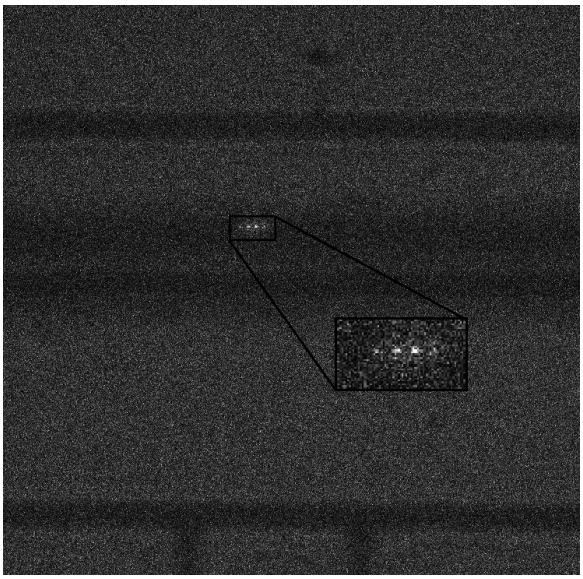

(a) Camera picture of four ions trapped underneath the wire, with height 500 µm. The wire is placed with the help of a microscope directly above the gap between the center and RF electrode. We see that the shadow of the wire, as well as the underlying trap structure, is visible in the picture. The picture was taken with a few hundred ms exposure time.

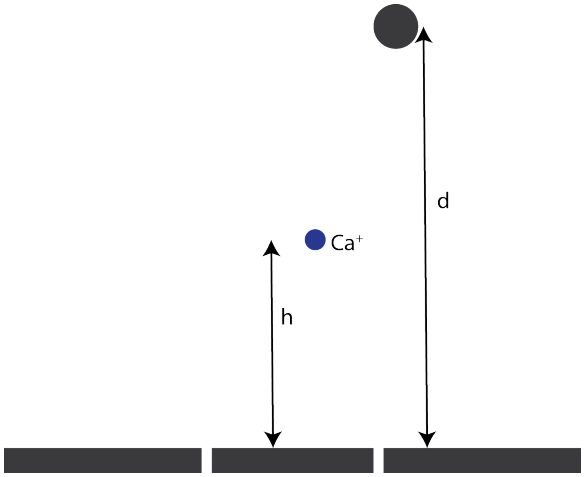

(b) Sketch of the wire position above the trap. Shows the trapping height h and the wire height d. For the sketch we view a cut at 90deg to the RF electrode at the ion position.

Figure 4.5: Illustration of the wire positioning above the trap.

238 µm and the wire to be offset in the horizontal by 50 µm to avoid blocking the fluorescence from the ion. The resulting trapping height for these parameters is 83 µm. Placing the wire directly above the center electrode improves the coupling resulting in $D_{\text{eff}} = 283\,\mu\text{m}$.

We also notice that a close coupling wire influences the trapping potential leading to a lower trapping height and stronger RF confinement compared to a trap without a coupling wire. An identical trap to the one used in these simulations without a coupling wire traps the ion 107 µm above the trap surface.

A camera picture that shows the horizontal displacement for a larger wire height can be seen in Fig. 4.5a along with a sketch illustrating the wire positioning above the trap in Fig. 4.5b.

Coupling using just the trap electrodes

An alternative way of connecting the LC resonator to the trap is by connecting it directly to the trap electrodes. When we simulate connecting the LC resonator between the center

electrode and the ground plane of the trap we find $D_{\text{eff}} = 430\,\mu\text{m}$ for a trap with a trapping height of $100\,\mu\text{m}$. The advantage of this coupling method is that the trap geometry is much better defined and there is no need for alignment by hand. However, the effective distance is increased significantly.

Connecting the coupling wire to the resonator

The wire above the trap is then connected to the LC-resonator by crimping to the wire leading out of the resonator can (Fig. 4.4c). We measured the resistance of this method of connecting the two wires to be below the sensitivity of a four-wire-measurement of a Keithley 2110 DMM of $10^{-4}\,\Omega$.

4.4 Heating rate of the ion

A very important metric for our experiment and many others is the heating rate.

$$\dot{\bar{n}} = \frac{d\bar{n}}{dt}\,, \tag{4.16}$$

with $\bar{n}$ the mean occupation number of the harmonic oscillator describing the ion motion.

The heating rate is important as a large occupation number will decrease the fidelity of carrier Rabi oscillations (see Eq.2.29). Further, we want to couple the ion to the LC resonator and investigate the energy exchange between the two oscillators. A possible experiment would be to cool the ion to the Doppler limit and bring the two oscillators into resonance. After equilibrium is achieved, we can then use the ion to determine the temperature of the resonator mode we coupled to. If the heating rate of the trap is higher than the heating due to coupling to the LC resonator, we cannot determine the temperature we reach or what part of the total heating rate is due to the LC resonator coupling.

The heating of the motional degree of freedom of the ions is due to fluctuations of the electric fields. It is assumed, that the spectral density of the electric-field noise S_E follows a power law with respect to frequency ω, the ion-electrode distance d, and the temperature T [64].

$$S_E \propto \omega^{-\alpha} d^{-\beta} T^{+\gamma}\,. \tag{4.17}$$

The study of heating rates in ion traps has found renewed interest since a scaling of the heating rates with a power law of d^{-4} was found [64]. The scaling is different from the d^{-2} scaling expected from Johnson noise. The d^{-4} distance scaling can be explained by small areas or patches, that vary slightly in the otherwise constant potential. These fluctuations may be due to absorbed atoms or changing crystal structures. This interpretation is further corroborated by studies that showed a reduction of the heating rate after cleaning of the trap electrodes [65][66].

The frequency scaling of the heating rate tends to follow a 1/f scaling behavior for S_E, which describes the range of $0.9 \leq \alpha \leq 1.4$ for the frequency scaling [67]. This scaling has

been measured in a wide range of ion trap experiments [64]. It should be mentioned that in some experiments a vastly different frequency scaling was found. In one case the frequency scaling changed dramatically from $\alpha = 0$ to $\alpha = 6$ after cleaning the trap surface with HCl [68].

Fortunately for our experiment, this observed anomalous heating is greatly suppressed at cryogenic temperatures [69] [70], with a reduction of the heating rate by two orders of magnitude when cooled to liquid helium temperatures [64]. The specific traps used in the experiment described in [69] had high heating rates, as compared to traps with identical trapping height, at room temperature. Cooling them to 6 K reduced the heating rate by seven orders of magnitude, two orders of magnitude below previously reported heating rates at room temperature. One suspected source of the motional heating is charge fluctuations that have been demonstrated to be thermally driven, which explains why cooling the trap to cryogenic temperatures reduces the heating rate.

We measure the heating rate with the carrier Rabi flop method described in Sec. 2.5.1.

Part II

Experiment

5 The cryostat

As we have seen in Sec. 3.3, a high quality factor of the LC resonator is important, since it minimizes the heating from the environment. To build a resonator with a high Q, we need to minimize losses in the resonator, for example, due to resistance or dielectric losses. The straightforward way of accomplishing this goal is by using superconducting wire, cooling it below its critical temperature T_C.

The cryostat used to cool the assembly is a closed cycle cryostat operating on the Gifford-McMahon refrigeration cycle[1] with a base temperature of < 4 K. The expander is connected to a compressor by two helium lines. A valve disk rotates to allow the high-pressure helium to expand into the expander before it gets compressed again in the compressor. A regenerative heat exchanger maximizes the refrigeration. The motor that drives the valve disk causes a vibration of the expander, which would be problematic for maintaining proper beam alignment when trapping ions $50 - 200\,\mu$m above a surface trap. To isolate the vibrations of the motor from the sample holder, there is an intermediary chamber sealed with a rubber bellow that separates the expander from the vacuum chamber. The intermediary chamber is filled with helium gas at a pressure slightly above ambient pressure and is cooled via a heat exchanger by the expander. The helium gas, in turn, cools the sample in the vacuum chamber and eventually liquefies to provide a cooling buffer. The residual vibrations have an amplitude of 5 nm and a dominant frequency of 2.7 Hz, as seen in Fig. 5.1.

After the cryostat is switched off, the liquefied helium can hold the sample temperature steady for roughly 100 min, depending on heat load, as seen in Fig. 5.2.

For the cryostat to reach its base temperature, we need to keep the heat load to a minimum. It consists of radiative heat transfer, heat conduction, and Joule heating. Table 5.1 shows the cooling power at various points of the cryostat.

[1] ARS DE-210S

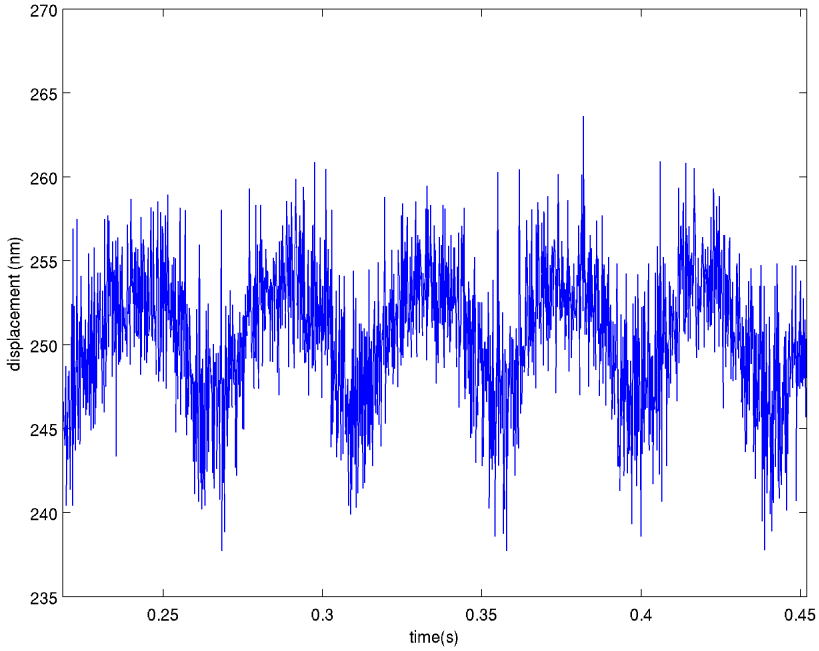

Figure 5.1: Measurement of the vibrations of the cold finger. For the measurement, one mirror of a Michelson interferometer was mounted to the cold finger. The dominant frequency is 2.7 Hz with an amplitude of 5 nm.

Temperature [K]	Cooling capacity [W]
4.2	1
10	9
20	16
77	26
1st stage 77	60

Table 5.1: Cooling power of DE-210S cryocooler.

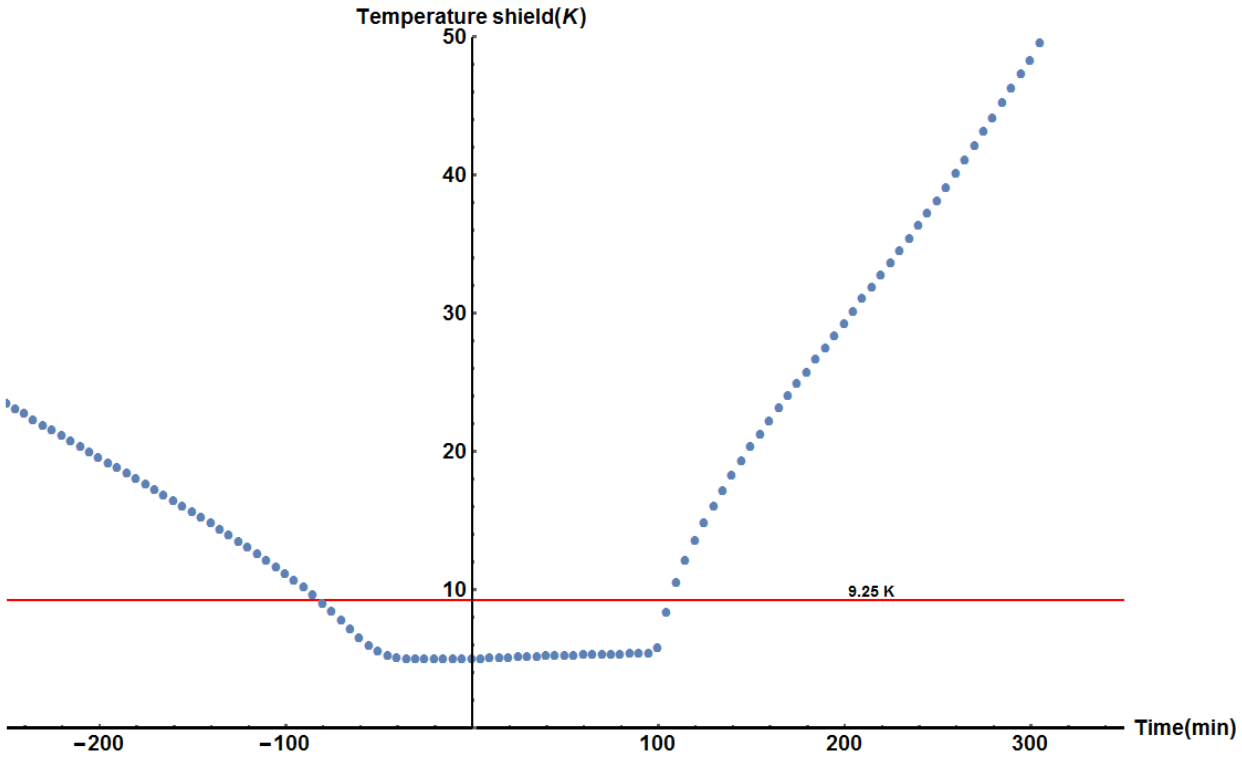

Figure 5.2: We measure the temperature on the niobium shield in the 4 K-stage after switching off the cryostat. A small reservoir of liquid helium keeps the 4 K-stage cold while the helium evaporates. The cryostat is switched off at time zero. The red line shows the position of T_C for niobium. During this measurement, no heat load from the RF drive was present. This measurement shows that we can stop the cryostat for some time to reduce any potential noise the cryostat operation produces. Due to additional heat loads the time window will be shorter than the 100 minutes measured here.

Material	$\lambda_{4K}[\frac{W}{mK}]$	$\lambda_{40K}[\frac{W}{mK}]$
Al6061-T6	8	60
Al6063-T5	40	250
OFHC	43	80
304 SS	0.4	8

Table 5.2: Thermal conductivity data for materials used in construction [71] [72] [73].

5.1 Thermal loads

We installed two layers of heat shielding inside the vacuum chamber, one of which is supplied by the manufacturer. However, we modified the manufacturer supplied heat shielding as we need additional space to fit filter-board, ion trap, helical resonator and our LC-resonator, including its shielding. The upper part is the OEM heat shield, a copper tube which has been silver-plated to increase reflectivity. Onto this tube we clamp the modified heat shield, which is manufactured from AL6063-T5 alloy. This alloy has a comparable thermal conductivity λ as OFHC copper as shown in table 5.2. The second inner thermal shield is manufactured from the same aluminum alloy and bolted directly to the cold finger of the cryostat.

Heat conduction through interfaces can be a major limiting factor to the sample temperature. The heat conductivity can be improved by using grease or solder joints. We limit the use of grease in the setup to prevent contamination of the ion trap surface. Instead, we use 500 µm thick indium sheets to improve thermal conductivity by about an order of magnitude for aluminum and copper interfaces [74]. For metal to metal contacts, the force with which the two parts are held together determines the heat conductivity [73]. Screws, made from 304 stainless steel, are used to connect parts and to attach the $4\,K$-stage to the cold finger. Stainless steel contracts 0.1% less than the aluminum alloy reducing the force holding the parts together. This is a universal problem, which also applies to other potential materials for the screws such as titanium. As a result, stainless steel screws are still the best choice. Because of the significantly lower thermal conductivity of stainless steel care needs to be taken to always join aluminum or copper directly together and to not have any stainless steel layers in any paths to the cold finger for any parts that need to be cold.

In our setup, one major source of thermal load is radiative heat exchange. The net radiative heat exchange between two surfaces is giving by [73]

$$\dot{q}_{\text{rad}} = \sigma E A (T_2^4 - T_1^4) \tag{5.1}$$

with the Stefan-Boltzmann constant σ, a surface temperature T, and a surface area A. E is a factor between 0 and 1, which depends on the emissivity ϵ of the material. Calculating the heat load for the dimensions of the cryostat, we find $\dot{q}_{\text{rad, 40 K}} = 4\,\text{W}$ and $\dot{q}_{\text{rad, 4 K}} = 2\,\text{mW}$. This shows the importance of a secondary heat shield as the cryostat would otherwise not be

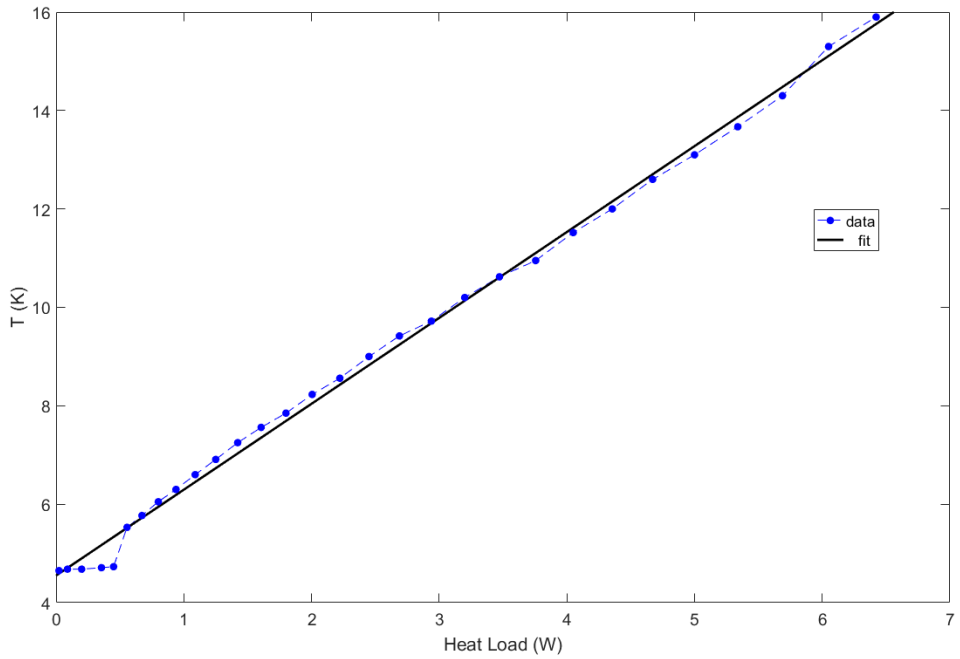

Figure 5.3: Temperature plotted against heat load. The temperature was measured directly at the cold finger and the heat load was applied via the 50 Ω resistor at the cold finger. This measurement was taken before any wiring of the cryostat was installed. The temperature rises linearly with the heat load. The flat section for the first 0.5 W can be attributed to a reservoir of liquefied helium that has not finished boiling off. The slope is 1.7 $\frac{\mathrm{K}}{\mathrm{W}}$.

able to cope with the 4 W thermal load of the 40 K environment. Moreover, we also found that it is crucial to thermally anchor the windows in the heat shield to the heat shield. Not doing so, we found the base temperatures of the 4 K-stage was raised by up to 2 K. The increase in temperature is caused by a much higher temperature of the windows when compared to the heat shield. This leads to a significantly higher heat load from radiative heat transfer due to the T^4 temperature dependence of radiative heating.

The windows have an area of 45 cm^2 and an E factor of 0.9. From 5.1 we can calculate the heat load if the windows do not thermalize to the 40 K-heat shield temperature. From Fig. 5.3 we see that even a heat load below 1 W will raise the temperature. Depending on how well the windows thermalize the cold finger will have an additional heat load of up to 1.6 W, corresponding to a temperature rise of 2.7 K. The observed rise in base temperature with poorly anchored windows can be explained by assuming the windows are at 230 K instead of 40 K. It is likely that the temperature of the windows will slowly equilibrate to a lower value, though anchoring them with indium strips is clearly the preferred solution.

The good thermal connection to the heat shield is assured by using thin indium strips around the windows before securing them with screws. Because of the ductile indium, the

windows can be held firmly in place without breaking.

Another source of thermal load is heat conduction, the magnitude of which can be calculated by

$$\dot{q}_{cond} = \frac{A}{l} \int_{T_1}^{T_2} \lambda(T) dT \, . \tag{5.2}$$

The thermal conductivity λ often has a strong temperature dependence, but cryostat design is simplified by tabulated thermal-conductivity integrals [73]. The cryostat is wired with 32 phosphor-bronze wires with a diameter of 36 AWG. In addition, there are three stainless steel coaxial cables[2] running to the 4 K-stage. The wires are thermally anchored at both the 40 K and 4 K-heat shield to avoid temperature gradients from the cold finger to the end of the wires. The thermal anchoring is achieved by epoxying[3] the wires into an aluminum mount that can be screwed into the heat shield. Heat load from the wiring accounts for $\dot{q}_{\text{cond, 40K}} = 12\,\text{mW}$ and $\dot{q}_{\text{cond, 4K}} = 26\,\text{mW}$ respectively, well below the cooling power of the cryostat.

One remaining and likely the dominant source of thermal load is from the RF power, which is used to drive the ion trap. Here we need a helical resonator [75] with a high step-up of the voltage to minimize this source of heating. The helical resonator we are using needs roughly 0.2 W of RF power to reach the required voltage.

5.2 Thermometry

The cryostat comes supplied with two silicon diode temperature sensors[4], one of which is attached to the cold finger and the other is thermally anchored to the 4 K-stage and can be attached anywhere within it. The 40 K-stage can be monitored separately with a Cernox thermometer[5]. The temperature of the heat shield can have dramatic effects on the base temperature of the cryostat due to the T^4 dependence of the radiative heat load, which makes the ability to monitor its temperature important. Additionally, there are some optional carbon resistor thermometers [76]. These are a cheap alternative build by grinding away the insulation coating of a carbon resistor until the resistive element is visible and then epoxied to a copper substrate with Stycast 2850. Care is taken to not short the resistor to the copper substrate. We conduct a 4-wire measurement with a sensing current of 10 µA. When the carbon sensors are calibrated with silicon diode, we found them reliable in the temperature range of $4 - 50\,\text{K}$ with an accuracy of about 100 mK. This is sensitive enough for our purposes as we primarily want to verify that the 4 K-stage temperature is below the superconducting transition of Nb or NbTi at 9.25 K and 9.8 K, respectively.

[2] Nexans 5633JZZD
[3] Stycast 2850
[4] Lakeshore Cryogenics, SD-670
[5] Lakeshore Cryogenics, CX-BR

5.3 Vacuum chamber

During operation, the vacuum inside the 4 K-stage is solely provided via cryopumping. Only during the cool-down process, we use a pumping station with a dry roughing pump and a turbo pump to reach a vacuum of $< 10^{-3}$ mbar. The shape of the chamber is shown in Fig. 5.4. To the instrumentation skirt, we attach two 8" nipples. Splitting this section into two parts simplifies opening of the vacuum chamber immensely. To the nipples, we attach an 8" octagon from Kimball physics which houses the heat shields and the experiment. Five of the eight 2.75" ports are covered with fused silica viewports, four which are anti-reflective coated for 397 nm and one coated for 800 nm, originally used for the oven laser described in Sec. 7.3. To one of the remaining 2.75" ports, we connect a full range gauge[6], an all metal angle valve[7], and a burst disk to provide a pressure relieve if the pressure inside the vacuum chamber rises to $9 - 11.5$ psi. An overpressure can occur during warm-up when a small leak is present and the cryostat is kept cold for an extended period of time. This results in air freezing out inside and then boiling off during the warm-up. The last 2.75" port contains the calcium oven mounted on an adjustable bellow. The lower port is covered with a viewport anti-reflection coated for 397 nm and 729 nm, which is used for imaging the ions.

Onto one of the viewports, we mount a magnetic field coil providing a magnetic field of $\approx 0.7\,\frac{\mathrm{G}}{\mathrm{A}}$, which we drive with a current of 3 A to provide a magnetic field of 2 G at the ion position. This magnetic field is necessary to split the Zeeman sublevels of the calcium ion.

5.4 Laser setup

We exclusively use diode lasers in our experiment. For the 729 nm, 854 nm, and 866 nm light, we use extended cavity lasers in the Littrow configuration[8] locked to a Fabry-Pérot cavity. As we need tens of mW power of the 729 nm, we amplify the transmission signal of the cavity first with two injection-locked diode lasers, and finally amplify it again to 450 mW with a tapered amplifier[9]. The 422 nm light, we generate by frequency doubling a 844 nm laser in a custom build Bow-tie cavity [42]. For the 397 nm light source, we choose a commercial diode laser that is amplified by a tapered amplifier and frequency doubled in a Bow-tie cavity[10], which provides enough power, 500 mW of 397 nm, for running multiple experiments concurrently. The final laser at 375 nm is for the second step of the photo-ionization (see Sec. 2.2) and does not need to be frequency stabilized to more than a few nanometer. Because of this, we operate the diode laser free running and only stabilize its temperature, as this keeps the wavelength sufficiently stable due to the narrow range of the gain medium of the laser diode.

[6] Pfeiffer, PKR251
[7] VAT
[8] Toptica Photonics, DL100, DL Pro
[9] Eagleyard photonics
[10] Toptica Photonics, SHG Pro

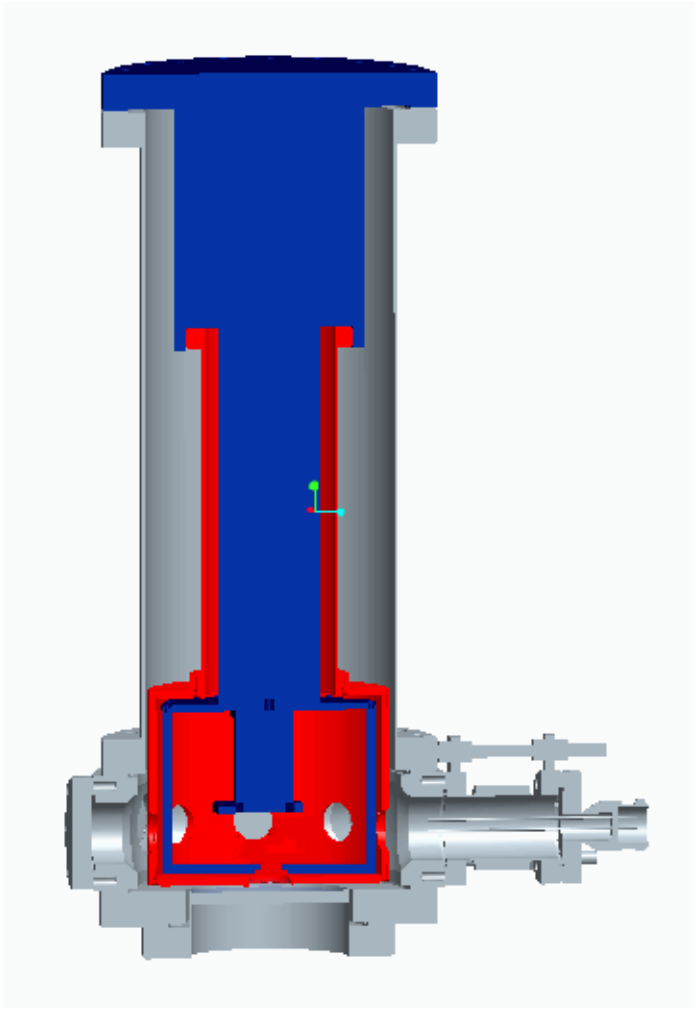

Figure 5.4: A rough sketch of the vacuum setup shown as a cut through the center. The 40 K-stage is shown in red and the 4 K-stage is in blue. The silver outer structure is the vacuum chamber. Electrical connections are not displayed. In the current setup, the one long 8" nipple is made up of two identical pieces.

The Lasers are in a separate room, shared between experiments. Having multiple laser beams in the same fiber may be beneficial, but we noticed problems with that approach. We observed that with short wavelength light close to the UV, there is a noticeable horizontal and vertical offset at the focus between two beams of different wavelengths in the same fiber. We avoid having a low laser power at the ion position for one of the beams, as would be the case if both lasers would be in the same fiber, by using a separate collimator for each short wavelength laser beam. For IR wavelengths this is not an issue for our collimators. Because of that, we keep the 854 nm and 866 nm light in the same fiber. Additionally, these two wavelengths are used for repumping and less power is needed. As the wavelength is far from the 397 nm used for detection we can easily filter any scattered light. In Fig. 5.5, the position of all the different lasers used are shown.

The collimators are mounted on two translation stages, one for moving the beam vertically and the other for translating the beam along the trap axis. For alignment purposes, we focus onto the trap and look at the image of the trap on the camera discussed in Sec. 5.5. We then align the laser beams using the reflections from the trap surface as visual feedback and use the translation stages to raise the beam up to the trapping height of the ion. Thanks to the accuracy of the translation stages and the BEM simulations (see Sec. 4.1), very little adjustment of the laser beams is necessary after an ion is trapped.

For all the sides where no laser beams enter, we use aluminum disks of the same dimensions as the AR coated windows to close the openings. The aluminum conducts heat many orders of magnitude better than fused silica [73] so that each closed side results in an about 200 mK lower base temperature of the 4K-stage.

5.5 Imaging and detection

To detect if an ion is present and what state it is in, we collect light from the $4^2S_{1/2} \rightarrow 4^2P_{1/2}$ transition. The light is collected by a custom built objective[11] via the 6" viewport at the bottom of the vacuum chamber. The objective is anti-reflection coated for 397 nm and 729 nm, has a diameter of 38 mm, and a design working distance of 58 mm. The lens is designed for use with a 6 mm fused silica viewport, but in our setup, we have two additional 3 mm thick AR coated fused silica windows in the two heat shields. The size and distance of the windows are selected such that no photons entering the objective will be blocked while minimizing the diameter of the window. This is important as having nine 1" diameter windows in each of the two heat shields raises the base temperature of the 4 K-stage by roughly 2 K. We found that compared to other experiments in our group, we detect noticeably fewer photons with our PMT compared to an identical imaging system, whose only difference is the lack of the two additional fused silica windows. The cause of this reduction is that even a flat window creates spherical aberrations that need to be corrected. Hence, a redesign of the objective to be optimized for 12 mm fused silica in the imaging path will likely increase our overall light collection efficiency. Correcting for these aberrations is crucial especially

[11] Sill Optics, Germany

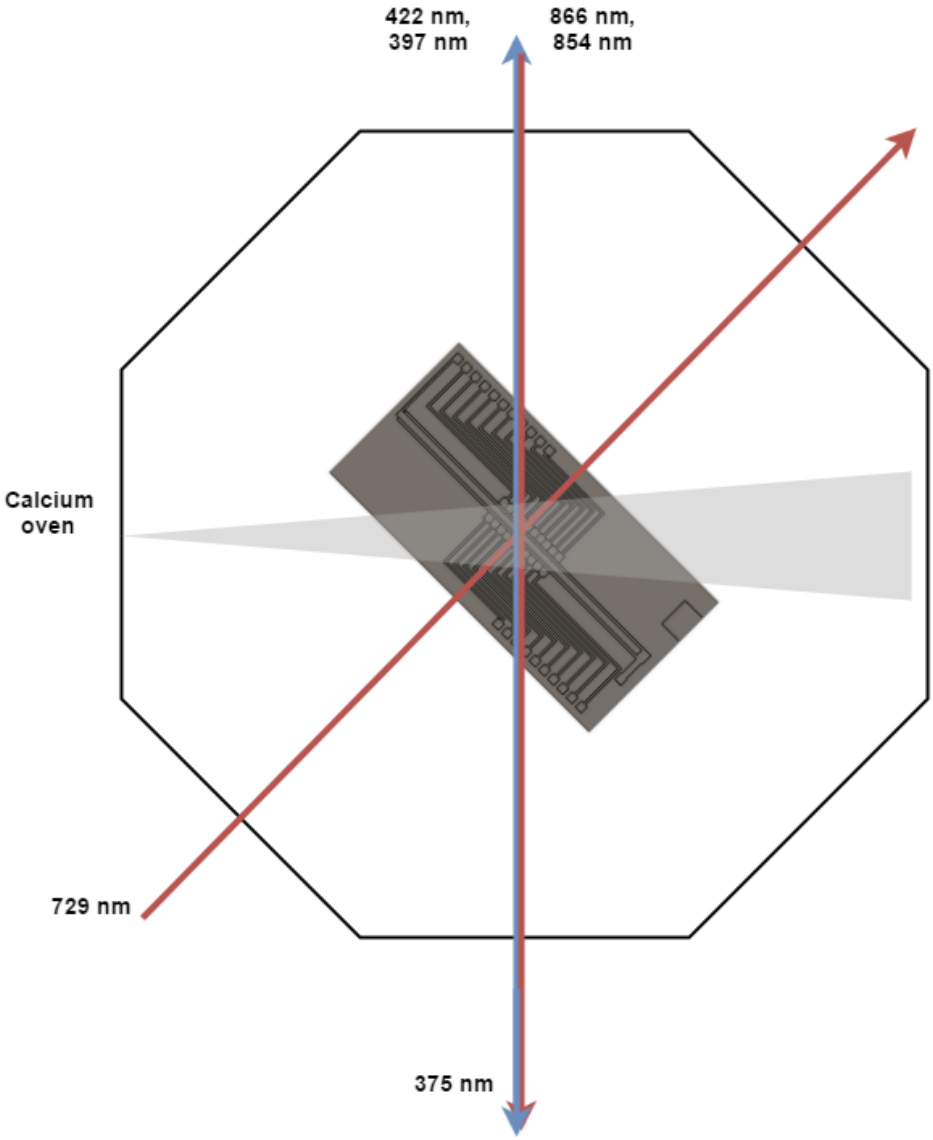

Figure 5.5: Sketch of the laser setup. The octagon represents the vacuum chamber and heat shields. The trap is in the center of the vacuum chamber. The arrows show the positioning of the collimators for the different lasers, the start of the arrow indicating the position of the collimator and pointing in the direction of the laser beam.

for large NA objectives such as required to collect the fluorescence of single ions. The aberrations are caused by the different angles and path lengths through the windows that result in each ray being focused in a slightly different spot [77]. The focal point of a beam passing through a parallel plate with a refractive index n with an aperture angle α is shifted by [77]

$$\Delta s' = d\left(1 - \frac{\cos\alpha}{\sqrt{n^2 - \sin^2\alpha}}\right) . \tag{5.3}$$

The light collected by the objective is guided via broadband dielectric mirrors into a shielded box that minimizes stray light. Other experiments in our group use a pellicle beamsplitters to allow for simultaneous use of a camera and a PMT [42]. In our case because of the lower light collection efficiency, we use a flip mirror to either direct the light onto an EMCCD[12] or a PMT. We place a slit with four blades in front of the PMT to have the ability to further reduce the amount of stray light collected. In front of both the EMCCD and the PMT, we place two bandpass filters[13] which have an 11 nm transmission band centered around 395 nm and combined block 19% of the 397 nm light while having an $OD > 8$ for the wavelengths outside the passband, greatly increasing our S/N-ratio.

We start our trapping attempts with all light from the objective directed onto the camera. The camera software also allows us to set a region of interest in which the pixel counts are summed and plotted versus time. With this information, we can adjust of laser detuning for Doppler cooling and accomplish some micromotion compensation (see Sec. 2.1). For running experiments such as Rabi flops, we sent all of the collected light to the PMT. We then set a threshold to determine if the ion is either in the $|0\rangle$ or $|1\rangle$ state. If the counts during a set time interval are below the threshold, we register this as state $|0\rangle$ and above the threshold as state $|1\rangle$.

[12] Andor Xion
[13] Semrock, USA

6 The superconducting LC resonator

When assessing earlier attempts to build high Q LC-resonators, we find two routes that experimenters that follow. The first route is using the self-capacitance of the coil [78], the other using low loss capacitors in addition to the self-capacitance [79] [80] [81]. The resonance frequency of an LC resonator is $\omega = \frac{1}{\sqrt{LC}}$. We want to maximize the coupling for a specific frequency, so as a result, we need to build an LC resonator, which has the highest inductance and lowest capacitance for a set resonance frequency.

The LC resonator is an integral part of the experiment. As shown in Sec. 3.2, a high inductance is needed to maximize the coupling rate to the ion. In addition, we also want to maximize the Qs so that the coupling of the resonator modes to the environment is limited as much as possible. To have the highest possible inductance for a given resonance frequency, we rely solely on the parasitic capacitance between different windings of the inductor and the unavoidable stray capacitances to ground. This parasitic capacitance but can be minimized by optimizing the geometry of the coil, for example, by restricting ourselves to just a single layer of windings.

For such a coil, the lumped element approximation fails as the voltage and current greatly vary over the inductor. In particular, we construct a resonator with a resonance frequency in the range of the trap frequency of Ca^+ ions of $1 - 3\,\mathrm{MHz}$. To this goal, we need to wind tens of meters of wire into a solenoid. Considering that the wavelength of a $2\,\mathrm{MHz}$ signal is $\approx 150\,\mathrm{m}$, the assumption of uniform conditions over the entire length of the wire are no longer given. Still, experiments have shown that an equivalent lumped parallel capacitance can be analytically calculated matching the experimental capacitance [82] [78]. A distributed element model describes the effects seen while measuring the LC resonators better, in particular, the presence of multiple resonances [83] [84] that are observed in the resonator described here, as we will later see.

6.1 Resonator Theory

The helical structure of the solenoids that we use in our experiments supports a standing wave along its length with a wavelength λ_g. We need to calculate the frequency for such a coil, as we need to match the coil's resonance frequency to the secular frequency of the ion for efficient energy transport from the coil to an ion. The height of a coil that matches the resonant condition for λ_g depends on the boundary conditions. In the case that one end of the coil is grounded, we find $h = \frac{\lambda_g}{4}$ and $h = \frac{\lambda_g}{2}$ if both ends are left floating [85].

With such a helical waveguide, we can calculate the velocity factor ν_f [86]

$$\nu_f = \frac{\nu_p}{c} = \frac{\lambda_g}{\lambda_0} = \frac{1}{\sqrt{1 + 20\sqrt{\left(\frac{D}{n}\right)^5 \frac{D}{\lambda_0}}}} \tag{6.1}$$

with a coil diameter D, phase velocity ν_p, windings per meter or 1/pitch n, and the free space wavelength λ_0. This expression is valid for $\frac{nD^2}{\lambda_0} \leq \frac{1}{5}$ as is the case for the solenoids constructed for this work. We solve Eq. 6.1 for λ_0

$$\lambda_0 = \sqrt[5]{\frac{400 D^6 N^5 \lambda_g^4}{h^5}} \,. \tag{6.2}$$

We determine the frequency

$$f_0 = \frac{K}{ND} \sqrt[5]{\frac{h}{D}} \tag{6.3}$$

where

$$K = \frac{c}{\sqrt[5]{400}} R^{\frac{4}{5}} \,. \tag{6.4}$$

Here, R is the resonance mode with $R = \frac{1+2i}{4}, i \in \mathbb{N}_0$ for quarter-wave resonators and $R = \frac{i}{2}, i \in \mathbb{N}$ for half-wave resonators with i signifying which overtone we are calculating the frequency for. In Fig. 6.1 the voltage along the resonator is shown for the first three resonances of a quarter wave resonator.

In an initial experiment, we want to use the ion to cool one of the resonant modes of a superconducting LC resonator. The quality factor Q of a resonator is an important figure of merit in this case as it tells how strongly it is coupled to the environment. The heating rate of a resonator mode is $\gamma = \frac{\omega}{Q}$. It also governs the $\frac{1}{e}$ storage time of excitation of the mode $\tau = \frac{2Q}{\omega}$, which will be important if we want to use this system to create a hybrid quantum system of trapped ions and superconducting circuit elements. The quality factor is limited by losses in the system, which can originate from a finite resistance R_R in the wire, the magnetic fields inducing currents in surrounding metals with a finite resistance R_M, or losses in the dielectric of the capacitor R_C, for example.

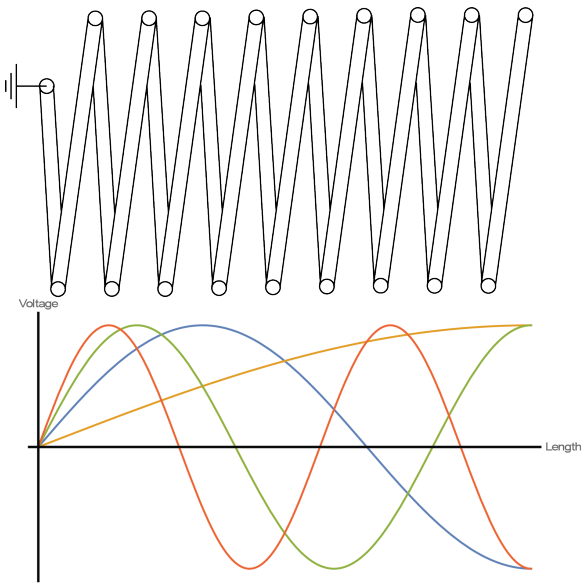

Figure 6.1: Illustration of the presence of multiple resonances in a LC resonator built from a single layer solenoid.

6.1.1 Dielectric losses

Dielectric losses are characterized by the loss tangent of the dielectric. It is defined as [87]

$$\tan\delta = \frac{\omega\epsilon'' + \sigma}{\omega\epsilon'} \tag{6.5}$$

which simplifies for a dielectric to $\tan\delta = \frac{\epsilon''}{\epsilon'}$, where the complex dielectric constant is $\epsilon = \epsilon' - i\epsilon''$. An alternative way to view the $\tan\delta$ is as δ, the angle between a capacitors impedance vector and the negative reactive axis. Hence, when choosing materials to use for the coil construction, the loss tangent of the material is important. When the entire electric field of the capacitor is inside the dielectric, the limit to the quality factor is $Q = \frac{1}{\tan\delta}$. When only part of the electric field is inside the dielectric material, the quality factor of the resonator is limited to

$$Q = \frac{W_e}{W_{e,D}} \frac{1}{\tan\delta} \tag{6.6}$$

were W_e is the total energy of the electric field and $W_{e,D}$ the fraction of the energy stored in the dielectric due to the loss in the dielectric.

Material	$\tan\delta$	Temperature
Formvar	1.3×10^{-2}[88]	300 K
PTFE	2×10^{-5}[89]	300 K
Quartz	$< 10^{-5}$ [90]	10 K
Sapphire	$< 5 \times 10^{-8}$ [90]	10 K
Stycast 1266	$< 10^{-6}$ [91]	4 K

The loss tangent at room temperature should be considered an upper bound as it is lower at 4 K, and generally decreases with decreasing temperature for many materials, for example, PTFE [92], quartz, sapphire, [90] and alumina [93]. Though this is not universal as can be seen in the example of $SrTiO_3$ and $NdGaO_3$ [94]. The loss tangent is also frequency dependent with $\tan\delta$ increasing with higher frequencies [95] [96] with some materials showing resonances [96], thus care needs to be taken to look for data at the relevant frequency and temperature to avoid surprises.

Formvar is a common choice for the insulation of wire but we can see from the loss tangent that is is a poor choice for wire used in the construction of high Q resonators as the Q would be limited to $Q = 76$ if the entire field is contained in the dielectric. Even though choosing PTFE the limit is $Q = 50,000$. However, only a small fraction fo the field will be contained in the insulator and hence PTFE should not limit the quality factor to below 100,000.

6.1.2 Choice of wire

In recent years, a wide variety of superconducting wires with a wide range of transition temperatures have become available such as REBCO or various low-temperature superconductors such as NbTi or Nb_3Sn, either as solid insulated wire or embedded in a copper matrix. There are also medium temperature superconducting wires such as magnesium diboride, whose wires are made with the powder in tube method. The REBCO wire, MgB, and low-temperature superconductors in a copper matrix all have the disadvantage of a larger cross section which would result in a larger overall coil. Additionally, the superconductors in these wire are in close proximity of normal conducting metals which lowers the achievable Q due to the induction of eddy currents and resulting losses [79].

Finite resistance of niobium wire below T_C

It is critical that the DC resistance of the wire is negligible as already a resistance of one Ohm will prevent us from reaching the desired quality factors. Because of this, we measured the DC resistance of the wire used for winding the coil.

Testing of the superconducting properties of the Nb wire was first carried out with a fully wound coil with $\approx 30\,\text{m}$ of wire, finding a DC resistance of $80\,\Omega$.

One possible cause for the high resistance is the crimp connection of the niobium wire to gold-coated copper pins similar to the connections shown in Fig. 4.4c. To rule out this cause, we made a series of crimp connections measuring them at room temperature

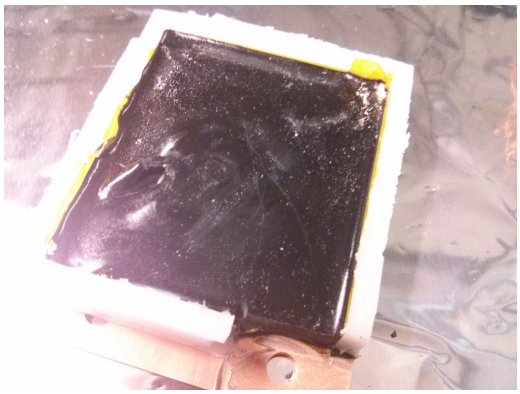

(a) Setup for measuring wire resistance below T_C.

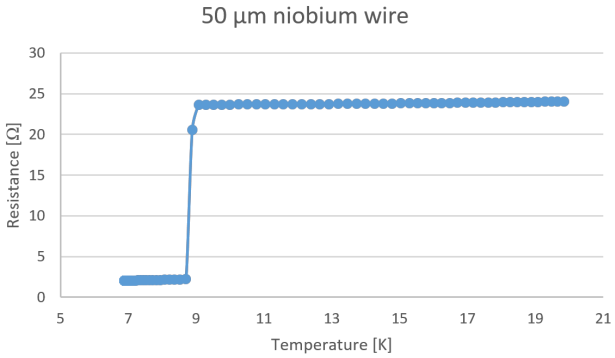

(b) The superconducting transition is visible in a resistance vs temperature plot even though there is a finite resistance in the superconducting state.

Figure 6.2: Measurements of different niobium and NbTi wires.

and finding resistances below the sensitivity of our 4-wire measurement. Also, cooling down some samples to normal experimental temperatures did not result in the connections failing. Though still care has to be taken when making the crimps as we had a failure rate of a few percent and most failures can be verified by slightly pulling on the two wires. Moreover, these failures are very easy to identify after they occur once we warm the cryostat up and measure the resistance over the LC resonator. Typically, a failure at the crimp connection also results in an open connection.

We tested three different samples of niobium wire: 50 µm Teflon insulated, 50 µm Formvar insulated, and 100 µm Teflon insulated wire. For a meter long section, we measured a resistance of 2 Ω for the 50 µm diameter wire. A plot of resistance versus temperature is shown in Fig. 6.2b. For the same length of wire, we measured 0.12 Ω for the 100 µm diameter wire. The entire wire was encased in Stycast 2850FT to assure proper thermalization as seen in Fig. 6.2a. A silicon diode thermometer was soldered on the measurement PCB to allow for a temperature measurement.

We found that the pure niobium wire we were using[1] still had a resistance of 33 $\frac{\text{m}\Omega}{\text{cm}}$ below the superconducting transition, while with two different samples of Nb48%Ti[2] the DC resistance of a 60 cm section of wire was below the detection limit of $10^{-5}\,\Omega$ for the DMM used[3]. The wire was encased in Stycast 2850FT for this measurement to ensure proper thermal anchoring.

For a similar measurement with NbTi wire, the resistance measured was below the detection limit of our DMM. Because of this, we will use NbTi wire for future experiments

[1] California Fine Wire Co
[2] California Fine Wire Co, GVL Cryoengineering
[3] Keithley 2110 DMM

unless we can find out the reason for the residual resistance of the niobium wire.

Critical field of niobium

Another possibility is that we reach the critical magnetic field and either have a mixture of superconducting and normal conducting state (H_{C1}) or just the normal conducting state (H_{C2}). Measurements for niobium give a critical field of $H_{C1} = 1.7\,\mathrm{kOe}$, and $H_{C2} = 4\,\mathrm{kOe}$ [97] much higher than fields found in our lab even when running the magnetic field coils we use for Zeeman splitting of atomic states ruling out this possibility.

Surface resistance

Ideally, we think of a superconductor to have no resistance below its critical temperature T_C which would be nice but is not true [98]. For a normal conductor in the case of an RF signal the surface resistance is given by

$$R_{Surf} = \frac{1}{\delta\sigma} \tag{6.7}$$

with the skin depth δ. For a superconductor in the two-fluid model, the skin depth is modified to [98]

$$\delta = \frac{\sqrt{2}\lambda}{\sqrt{\omega\tau\frac{n_s}{n_n} - i}}\,. \tag{6.8}$$

Here, n_n and n_s are the electron density in the normal and superfluid state, λ the penetration depth, and τ the momentum relaxation time. For frequencies $f < 10^{11}\,\mathrm{Hz}$ $\omega\tau \ll 1$ and the skin depth simplifies to $\delta = \sqrt{2i}\lambda_L$. We find that the skin depth for frequencies up to the high microwave frequencies is larger than the maximum 1/e distance, the London penetration depth λ_L [98]. As a result, we will substitute the London penetration depth for the skin depth in the following discussion.

The conductivity of a superconductor has a real and imaginary part

$$\sigma = \sigma_n + i\sigma_s = \frac{n_n e^2\tau}{m(1+\omega^2\tau^2)} + i\left(\frac{n_s e^2}{m\omega} + \frac{n_n e^2(\omega\tau)^2}{m\omega(1+\omega^2\tau^2)}\right) \tag{6.9}$$

which simplifies when we remember that $\omega\tau \ll 1$ for frequencies of interest to us.

The surface resistance is the real part of the complex impedance so

$$R_{surf} = \frac{1}{\lambda_L}\frac{\sigma_n}{\sigma_s^2+\sigma_n^2} = \frac{1}{\lambda_L}\frac{\sigma_n}{\sigma_s^2} \tag{6.10}$$

where we utilized the fact that $\sigma_n^2 \ll \sigma_s^2$ in our frequency regime.

We assume we will be working in a temperature regime $T \sim T_C$. In this regime, we find

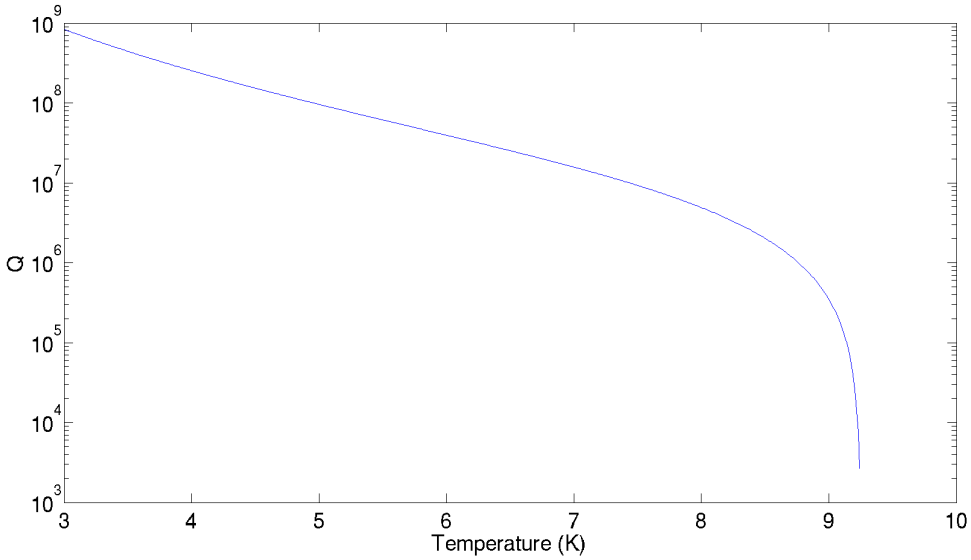

Figure 6.3: Limit on Q due to surface resistance at 2 MHz.

[98]

$$\frac{n_s}{n} = 1 - \left(\frac{T}{T_C}\right)^4 . \tag{6.11}$$

Using the dimensions of a typical coil and wire diameter we can then calculate the surface resistance and the resulting Q that we could expect the result of which is shown in Fig. 6.3. We can see from the graph that the surface resistance of the wire should not be a limitation as long as we are at least a few hundred mK below the superconducting transition.

6.1.3 Thermal anchoring

During our measurements, we also learned the importance of proper thermal anchoring of the superconducting wire. We can calculate the temperature drop over a 1 cm long section of niobium wire [73]

$$\Delta T = \frac{\dot{Q}}{\bar{\lambda}} \frac{l}{A} . \tag{6.12}$$

The mean thermal conductivity of niobium at the superconducting transition is $\bar{\lambda}_{9\,K} = 0.4\,\frac{\mathrm{W}}{\mathrm{cmK}}$ [99], which results in a temperature gradient of $0.25\,\frac{\mathrm{K}}{\mu\mathrm{W}}$. For NbTi, the mean thermal conductivity is two orders of magnitude lower [100], resulting in an even larger temperature gradient when energy is dissipated in the wire. We already experience Joule heating when conducting a 4-wire measurement for which we pass 10 µA of current through the niobium wire as the niobium wire has a finite resistance, even when parts of it are superconducting. This results in a temperature increase and a sharp increase in the resistance when conducting a resistance measurement after letting the wire cool down below the transition temperature.

For both samples of Nb-48%Ti at temperatures below the superconducting transition, we find the resistances lower than our detection limit and no resistance increase is noticeable during the 4-wire measurement opposed to what we experienced for pure niobium wire.

Therefor, we use cryogenic vacuum grease[4] to thermally anchor the superconducting wire to the sapphire coil former. The section that leads out of the superconducting shield is difficult to thermally anchor, so we choose a material for this section for which the absolute temperature is not critical and which by itself has a better thermal conductivity. The copper wire leading out of the magnetic shield has a resistance $< 1\,\mathrm{m}\Omega$ and has only a slight dependence on the temperature. Additionally, its thermal conductance $\bar{\lambda}$ is orders of magnitude larger than that of niobium, resulting in a lower ΔT for the same power dissipated in the wire.

6.1.4 Coil former and magnetic shielding

A coil former is the body of a coil, upon which the wire is wound. It is used to keep the wire in a particular shape. It is absent in air-cored coils, for which the wire stiffness provides the structural integrity. It should not be confused with the magnetic core sometimes used to increase the magnetic field created. Another approach is to preserve the coil structure with epoxy [101]. Heat conduction through the wire is limited because of the thin wire diameter we use. Ideally, we need a coil former material with a good heat conduction to make certain that the entire length of the wire is in thermal equilibrium with the rest of the coil. We decided to use coil formers made from quartz and sapphire because of the low loss tangent and good thermal conductivity of these materials.

The material of the coil former was chosen for two reasons. The first is that the thermal contraction when cooled from room temperature to 4 K, $\frac{\Delta L}{L}_{4K}$, for sapphire $\frac{\Delta L}{L}_{4K} = 0.079$ is a better match to that of niobium $\frac{\Delta L}{L}_{4K} = 0.1436$ than quartz $\frac{\Delta L}{L}_{4K} = -0.008$ [73]. This is important because the tube is glued with Stycast 1266 to the top of the superconducting shield, which is made from 99.8% pure Nb. Initially, a quartz tube was used but we found that due to the slightly different thermal expansion of Nb and quartz, the tube would shatter after a couple of cool-down cycles. The shield itself is machined of 99.9% pure niobium.

The second reason is that Sapphire has an even lower loss tangent than quartz [96] with a value of $\tan\delta < 10^{-10}$.

In order to maximize inductance of the solenoid coil, $L = \frac{\mu N^2 A}{l}$, we want to maximize the diameter of the coil. Due to limitations in the size of the 4 K-stage of the cryostat, the shielding of the coil is chosen with a diameter of 5 cm. The coil itself is wound on a 4.5 cm long and 3 cm diameter sapphire tube. This was the largest diameter sapphire tube we found commercially available at a reasonable price. Higher inductances could be reached by increasing the tube diameter.

Another limitation on the size comes from the ideal size for the coil shield. The current induced in the shield from the coil creates a flux in the coil turns, which can reduce its

[4] Apiezo N

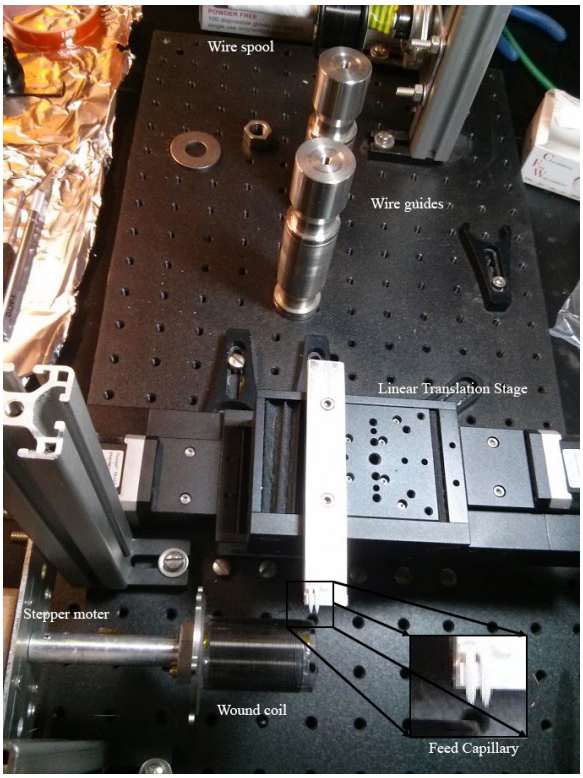

Figure 6.4: The coil winding machine.

Figure 6.5: Picture of a finished coil. Nb wound on a quartz cylinder.

inductance [102]. Calculations for coils of similar dimensions in [102] show that for a shield that has an about 40% larger diameter than the coil, the reduction in inductance is about 10%. This effect almost disappears for a shield that has twice the coil diameter. As a result, we find that our current coil former and shield combination should not reduce the coil inductance by more than a few percent.

The coil is wound from 50 µm diameter superconducting PTFE insulated wire on a home build winding machine shown in Fig. 6.4. A stepper motor rotates the coil former at a constant speed while a linear translation stage moves a feed capillary along the coils former, resulting in an adjustable pitch of the superconducting wire. Two posts act as wire guides to remove the jitter of the wire as it is being pulled from the wire spool. The pitch can be adjusted by setting the frequency of the TTL signal which controls the stepper motor driver. Each TTL pulse advances the stepper motor by $\frac{1.8}{8}^\circ$ as the micro-step functionality of the driving circuit is enabled, resulting in one revolution per 1600 TTL pulses. The linear translation stage is normally set to a speed of $0.08\,\frac{\mathrm{mm}}{\mathrm{s}}$, so that a TTL frequency of 1600 Hz results in a pitch of 0.08 mm. A finished coil is shown in Fig. 6.5.

6.2 Measuring the quality factor

We had to fabricate many iterations of the LC-resonator to find the best materials and techniques to use in its production. To evaluate a particular coil it is connected to a measurement board. The measurement setup is sketched in Fig. 6.6a. To connect the coil, we crimp the wire to a gold plated push on connector that mates with a connector soldered to the measurement board seen in Fig. 6.6b. The board weakly couples the coil via a capacitor with $C_c = \mathcal{O}(100\,fF)$ to a coaxial cable connecting to the outside of the cryostat. On a trigger from the measurement computer, a signal generator sends 10 ms long RF pulses via an RF switch through the coupling capacitor into the LC circuit. The energy in the resonator saturates if the excitation pulse length is chosen as $t_{\text{Pulse}} = \frac{2Q}{\omega} = \tau$, the mean lifetime of the signal in the resonator. For longer times, the return amplitude does not increase and eventually the amplitude decays as the energy dissipation heats the resonator past T_{C}. For a frequency of $\omega = 2\pi \times 2.6\,\text{MHz}$ and $Q = 10^5$, the optimal time is 2.6 ms, so 10 ms ensures we saturate the resonator while not excessively heating it. The 10 ms pulse length also broadens the excitation frequency by 100 Hz, making the excitation more likely in the case of an extremely high Q. After a pulse has been sent, the switch is toggled to record the returning signal from the LC resonator on an Oscilloscope and store the data on a computer. The frequency is stepped through in 1 kHz steps, taking one data point every few hundred ms. For each step, we calculate an FFT of the signal returning from the resonator. To find the resonances of the coil, we take the magnitude of the Fourier transform for the three frequencies closest to the excitation frequency and calculate the mean. This mean is then plotted for each of the 1 kHz steps to find the resonances as in Fig. 6.7.

An FFT of the return signal shows in some cases a frequency two or three times higher than the excitation signal. This allows us to faster find resonances at higher frequencies. An example of this is shown in Fig. 6.7. Typically, the resonances are excited by multi-photon processes, which result in a lower return signal and have to be excited with a more accurate frequency. This is visible in Fig. 6.7 as a lower number of data points for higher order excitation.

Once we know where the resonances approximately lie, we manually find the resonance frequencies by taking measurements in 100 Hz steps and look for the signal with the highest return amplitude from the LC resonator and determine the decay time τ. Due to noise, we time bin the data and find the maximum and minimum of each bin before fitting an exponential to both the minima and maxima. The quality factor can then be calculated by $Q = 2\tau\omega$ receiving a value for both the upper and lower part of the decay curve. An example of this can be seen in Fig. 6.8.

The signal generator we used for the quality factor measurements has a maximum output amplitude of 10 V. Even with a 10 V measurement amplitude, we found no change in resonance frequency or degradation of the quality factor if the duty cycle was less than 1%. A duty cycle of 50% would typically result in a loss of resonance after about a minute of measurements because the temperature of the coil rose above T_C. This is likely due to the heat load of the measurement process and will depend on thermal conductance of the exact

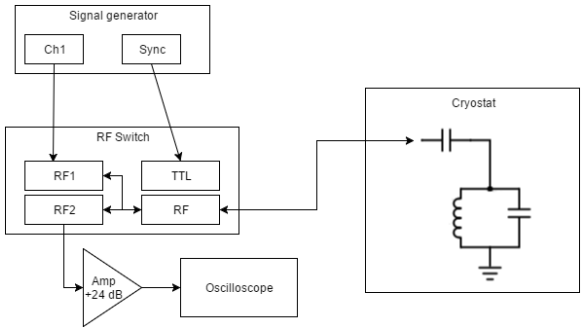

(a) Setup for finding of resonances of the resonator and determining the quality factor.

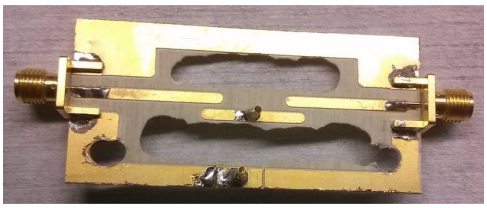

(b) Coupling board to realize the coupling capacitors.

Figure 6.6: Measurement setup.

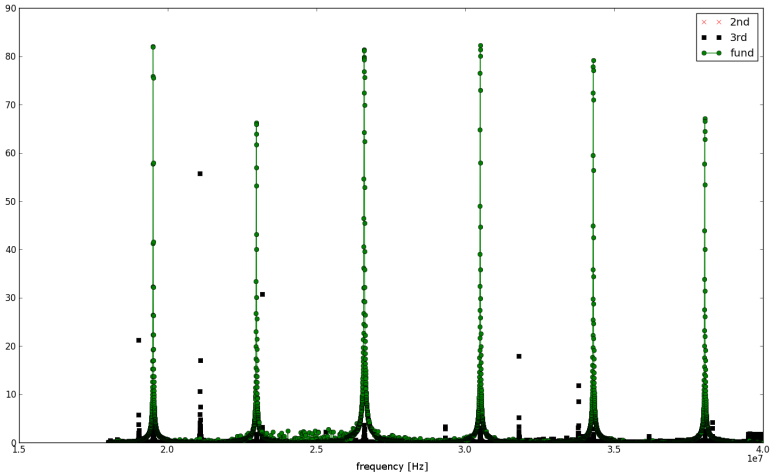

Figure 6.7: Example of conducting a search for the resonator resonances via FFT. Resonances whose FFT signal showed a resonance frequency at twice the excitation frequency are shown in red, those with frequencies at three times the excitation frequency in black.

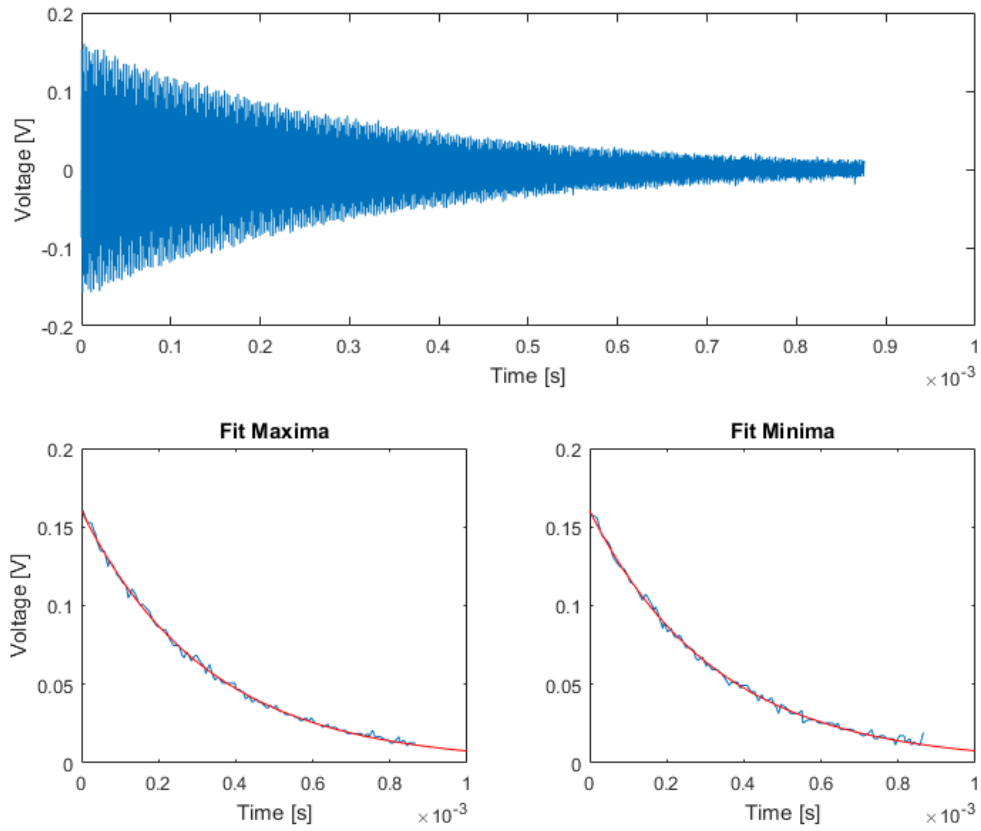

Figure 6.8: Visualization of the fitting procedure to determine τ. In this figure the quality factor for the fundamental mode of a resonator at $f_0 = 1.77\,\mathrm{MHz}$ was measured.

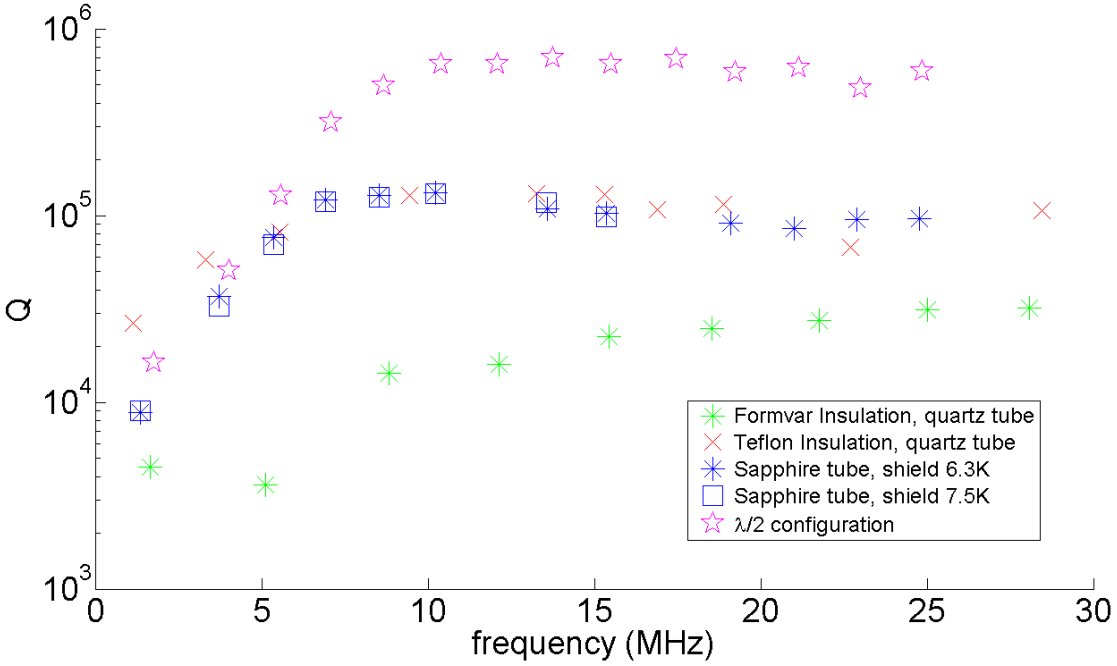

Figure 6.9: Q factor vs frequency for a variety of different resonators we built. The measurement points shown as purple stars and the blue boxes and stars were measured with the same coil. The only difference was the connections on the measurement board which was in $\lambda/4$ for the blue data points and $\lambda/2$ for the purple data points.

setup tested. The heating is likely stronger for higher amplitudes, so we check resonance Q versus excitation signal amplitude for new coils but so far no dependency has been seen any for the coils investigated when keeping with a 1% duty cycle and a maximum amplitude of 10 V, which is high enough to get a $S/N > 1$ for all coils tested.

6.3 Iterative improvements of the solenoid LC resonator

The first coil was wound from 99.8% pure, Formvar insulated Nb wire and had a fundamental resonance frequency of 3.8 MHz with a quality factor $Q = 3000$. The wire was held in place with a thin layer of super-glue. This likely reduced the quality factor and for the next coil, only the beginning and the end were attached with a drop of Stycast 1266. Further investigation of this coil discovered that a whole range of resonances existed. The LC-resonator has the same boundary conditions as a Helical resonator in $\frac{\lambda}{4}$ configuration [75][103] as shown in Fig. 6.6a. The spacing of the resonances is consistent with Eq. 6.3 within an error of 10%.

In the next iteration of the coil, we used Teflon insulated 99.8% pure Nb wire and

achieved $Q = 2.7 * 10^4$ for the first resonance and $Q > 10^5$ for resonances $f > 10^7$ Hz. It is evident in Fig. 6.9, that the quality factor rises steeply for the first few resonances. This is unlikely to be caused by the frequency dependence of the loss tangent as it tends to increase with higher frequencies [92][95][96], even though only limited frequency data is available for the materials we use. Also, previous experiments at kHz frequencies showed that the quality factor decreases with higher frequencies [80]. Though in that experiment, for each resonance a different capacitor of the same make and series was used the shift the resonance frequency, whereas here we are measuring higher order modes. The likely cause is a series DC resistance which limits the maximum Q following the relation

$$Q = \frac{\omega L}{R_s} \,. \tag{6.13}$$

In this case, we have a linear dependence of Q and ω which is also visible in Fig. 6.9. For roughly a factor of eight in frequency, we gain an order of magnitude in Q. For higher frequencies, this dependence disappears as other loss mechanisms such as the loss tangent become the limiting factor.

In a further attempt to improve the quality factor and increase the robustness the coil during cool-downs, we switched to sapphire coil formers. While the quality factor did not increase, the resonator assembly would no longer break when thermally cycling it from room temperature to 4 K.

We also measured the quality factor at different temperatures fo the coil former, the result of which is shown in Fig. 6.10. We used a carbon thermometer, glued with Stycast 2850FT to the inside of the coil former, to measure the temperature. For multiple resonances, we observed a sharp increase of the quality factor below 6 K. Likely a threshold temperature for a loss mechanism in the dielectric or the result of an additional section of the wire becoming superconducting. For later measurements we were restricted to higher coil temperatures and no temperature dependence was observed in the temperatures range we could access (see Fig. 6.9). A cryostat with a larger cooling power that allows us to cool past $4\,K$ would allow us to increase the Q according to these measurements.

The last measurement in Fig. 6.9 was conducted with different boundary condition creating a $\frac{\lambda}{2}$-resonator. For this measurement, both ends of the coil were only weakly capacitively coupled. The increase of quality factor for higher frequency overtones that resulted was likely due to the increased decoupling from the environment hinting at losses, not in the coil itself, but in the circuit after the coupling board. Another possibility is that the different electric field distribution for this coupling method plays a role. Also observed are losses for frequencies below 10 MHz, that we have not yet reduced with our current changes, which further substantiates the idea that those losses come from a DC resistance described by 6.13.

We also tried a different coupling method to determine if our measurement board might be responsible for some losses. The setup for the method is shown in Fig. 6.11. The coil wire is not crimped but placed parallel to another wire that connects to the coaxial cable running to the cryostat feedthrough. This way we can find out if the connection to the measurement

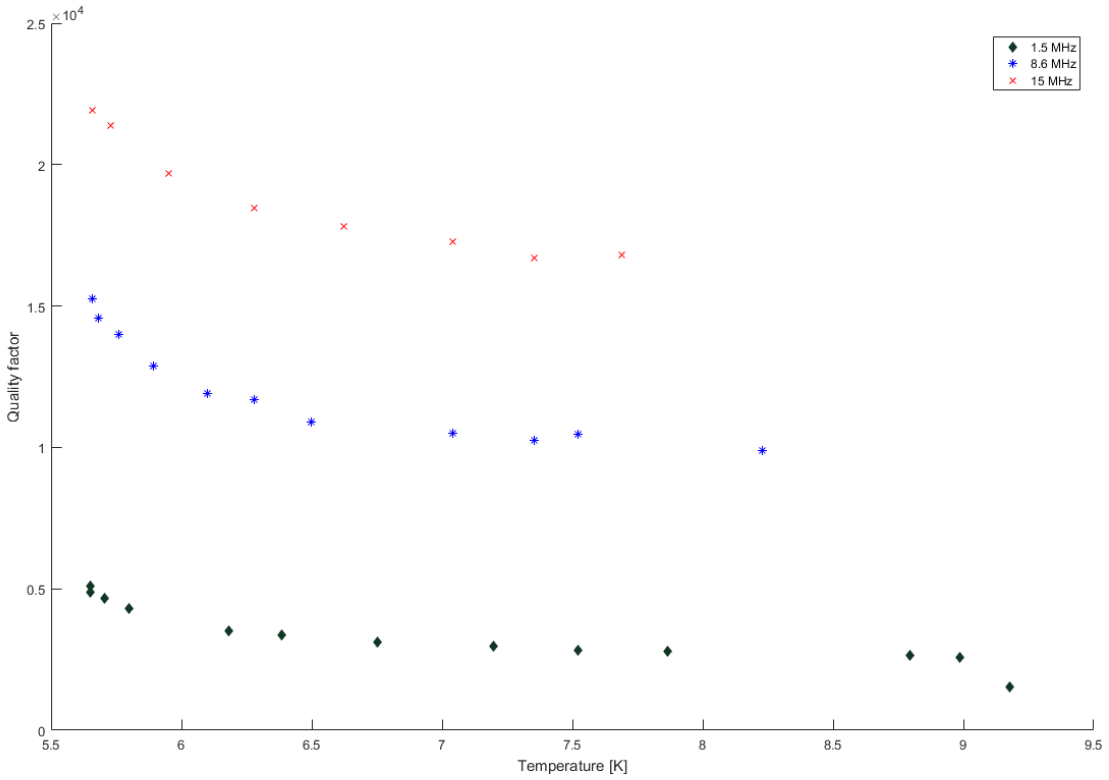

Figure 6.10: The plot is showing the temperature dependence of the quality factor for three different modes of the resonator for an early LC resonator.

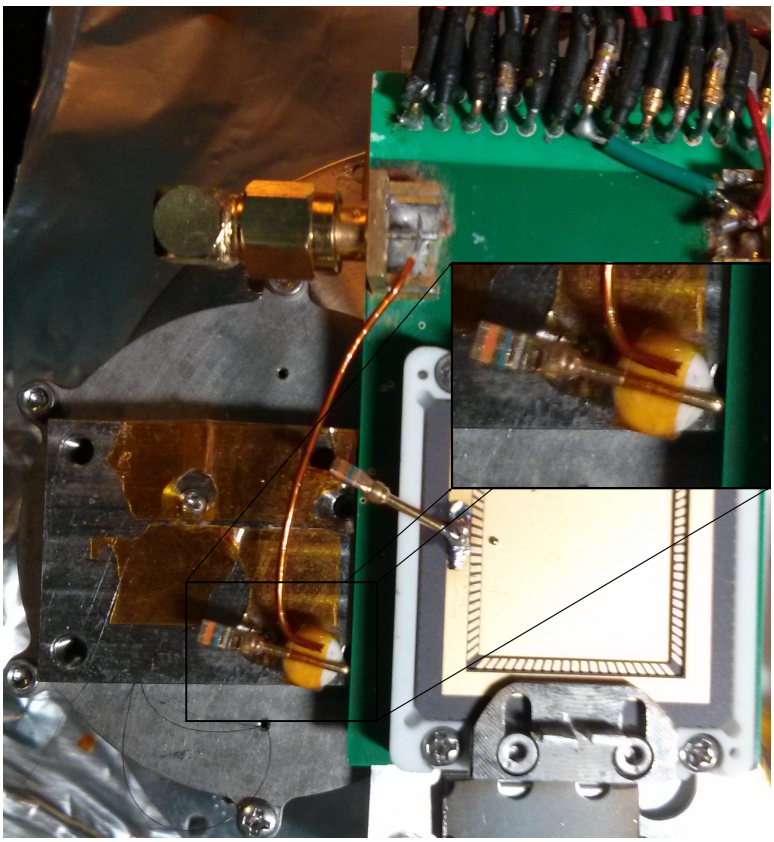

Figure 6.11: Alternative coupling method to the previously shown measurement board. The wire from the coil is crimped to a gold pin and placed in proximity of a Kapton insulated copper wire, which is connected to the center conductor of a coaxial cable. The other side is crimped into a gold coated pin that is soldered to the trap ground.

Figure 6.12: Picture of a toroidal resonator and the PTFE parts used as a former. This specific resonator is wound from copper wire while the ones in our experiment are made from NbTi wire.

board we previously used is a source of losses. While in the first iteration, we still used a crimp contact for the wire connected to ground, we later spot-welded the niobium wire to a larger diameter copper wire, which was soldered to the trap ground. In these experiments, we did not observe an improvement of the quality factor, from which we concluded that the measurement connections currently do not provide any limitation for our experiment.

The LC resonator used in coupling experiments

After initial resonators with $Q > 10^5$ we measured lower quality factors for newer resonators. The first coupling experiment described in Sec. 8.2 was performed with a coil were the quality factor of the fundamental mode at $f_0 = 2.64\,\mathrm{MHz}$ was measured as $Q \sim$1000, the exact value changing by factors of three for separate measurements using different coupling methods without any clear trend. In some cases, the S/N-ratio was too small to reliably determine a quality factor and only an order of magnitude estimate was made. For low quality factors, the initial signal is saturating the amplifier and causing an offset of the overall decay. Lower excitation powers do not solve this problem as the low quality factor leads to a fast decay of the signal. The change in quality factor was likely due to parts of the wire not reaching T_C as we later found (see Sec. 6.1.3).

6.3.1 Toroidal resonators

A very different and promising design is that of a toroidal resonator in which the field is contained inside the toroid, hence such a resonator is far less susceptible to losses due to imperfections in the shielding or dielectrics on the outside of the coil. Examples of such resonators in the literature have shown a factor of four improvement over the results we showed so far [104]. We could not verify this improvement in our experiment, though this might in part due to a section of the NbTi-wire not cooled below the superconducting transition temperature since we did not replace the last section leading to the measurement board with copper wire. The maximum quality factor measured for the toroidal resonator was $Q \sim 5,000$ for a resonance at $f = 1.899\,\mathrm{MHz}$, we also measured several higher harmonics of the resonator with similar results. We tried several coupling methods, such as a measurement board (Fig. 6.6b) and parallel wires (Fig. 6.11), without any clear improvement of the quality factor.

Later attempts were foiled due to the coil breaking. Another detrimental factor of the toroidal resonator is that it is time-consuming to construct as we have to wind it manually, making on the order of 500 windings with a thin wire that is prone to ripping when too much strain is present. The toroid is wound in two halves to simplify the construction process and is separated into multiple sections so that the wire in the divisions does not shift around easily.

6.3.2 Finite DC resistance

Later resonators we produced from 99.8% pure niobium wire showed a distinctly limited Q compared to earlier versions. The quality factor would fluctuate between $100 - 10,000$. This is partly explained by limited thermal anchoring of the leads leading out of the shield, see Sec. 6.1.3, and also by the fact that the niobium wire has a finite DC resistance even below the superconducting transition resulting in $R_s = 80\,\Omega$ for a coil with $f_0 = 2.3\,\mathrm{MHz}$. The limitation for the quality factor due to a series resistance is given by Eq. 6.13. For our resonators, we find that the inductance is of order mH, meaning that a $Q \approx 1000$ resonator can be explained by a series resistance $R_s \geq 10\,\Omega$. It is unclear how earlier samples of wire were different, as we achieved much higher quality factor than should have been possible with wire that has the same residual resistance below the superconducting transition. For $Q = 27,00$ measured and the inductance of that resonator, we would expect $R_s = 1\,\Omega$, which is much lower than the $R_s = 80\,\Omega$ measured for a similar coil fabricated later. This suggests that there was something markedly different about the niobium wire used for the first coils, but so far we could not identify the difference.

7 Trap fabrication and electronics

In this chapter, we will focus on the fabrication of traps whose design was discussed in chapter 4. We will also go into detail of the voltage sources for the DC and RF electrodes and how we stabilize the trap frequencies.

7.1 Trap fabrication

For our experiments, we require traps that have a small ion electrode distance, smaller than commonly found in 3D traps. Initial simulations to find what tolerances are acceptable for a miniature 3D trap and consultation with specialists showed us that we should instead work with surface traps. These traps are designed such that all electrodes lie in a single plane.

There is increasing empirical evidence that contamination of the metal electrodes with hydrocarbons or other adsorbed molecules can drastically increase the heating rates of ion traps [65] [66]. While the heating rate can be strongly suppressed by cooling the ion traps to cryogenic temperatures [69], it is important to minimize the additional noise due to surface contamination for room temperature setups. We want to design a fabrication process also applicable for room temperature to simplify and unify the fabrication of traps. Therefore, we are using a fabrication method that minimizes the chemicals the trap comes into contact with after the evaporation of electrodes such as solvents to wash away excess photoresist.

For the traps fabricated at UC Berkeley, we developed a fabrication method that does not require a solvent cleaning step after metal evaporation. We pattern fused silica substrates with high aspect ratio, five times as deep as they are wide, trenches with methods described below. The patterned substrate is then mounted at an angle and evaporated with metal. The trench depth and evaporation angle prevents shorting between electrodes without the need of further photo-lithography.

Initial experiments were conducted with traps produced at ETH in Zurich, Switzerland, and which were also used in other early experiments in our group [105][106].

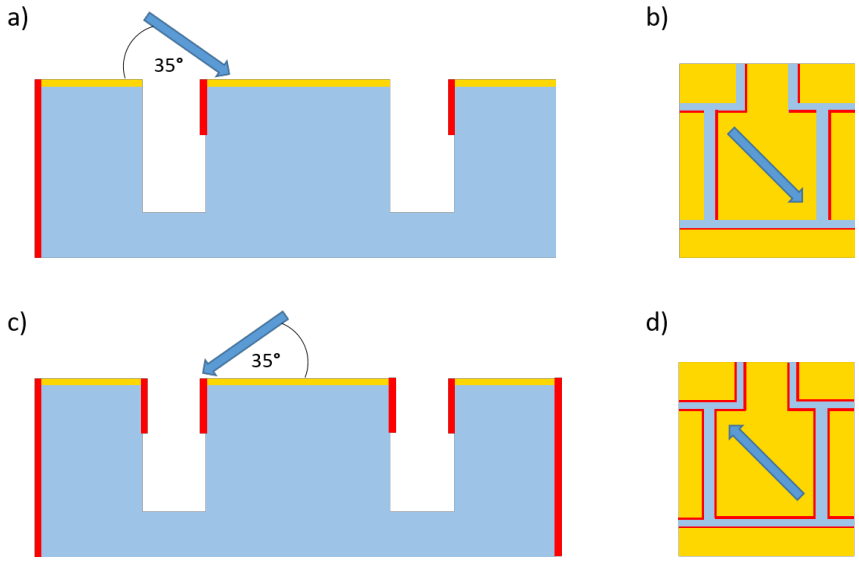

Figure 7.1: Illustration of the evaporation process. a) vertical cut through the substrate showing the trenches. The red color indicates which edges of the substrate are coated with metal. b) top view. Pictures c), vertical cut and d), top view, are after rotating the substrate by 180° and doing a second evaporation step of Ti and Au.

7.1.1 Ion etch patterning of substrates

The second generation of traps was produced at the Marvell Nanolab at UC Berkeley using photo-lithography and ICP DRIE with a CF_4 enchant, we achieved trench depths of approximately 20 µm. We coat quartz wafer with photoresist, which is developed with a mask. The photoresist protects the electrodes in the ICP DRIE etching step so that only the trench between the electrodes is etched. The excess photoresist is washed off and the wafer then evaporated with 15 nm Ti and 600 nm Au. The trap can then be mounted on a CLCC for wire-bonding. This fabrication method is explained in more details in reference [107].

7.1.2 Pulsed laser patterning of substrates

We later switched to a patterning process that is far simpler for us. The electrode pattern is defined via trenches in a fused silica substrate. A pulsed-laser weakens the fused silica substrate before the material is etched with hydrofluoric acid. These steps are performed by Translume, Ann Arbor, MI, and achieve trench depth of approximately 50 µm.

The actual metal coating of the substrate is then performed in-house. The substrates are first etched for 10 minutes in a Piranha solution (three parts concentrated sulfuric acid and one part 30% hydrogen peroxide solution) heated to 120°C. This step removes carbon compounds on the substrate surface and increases adhesion of the metal layer. After the cleaning, the trap is mounted on a holder for evaporation and placed in the evaporation chamber.

Material	rate of evaporation
Ti	0.5 Å/s
Al	5 Å/s
Cu	1 Å/s
Au	3 Å/s

Table 7.1: Evaporation rates used in the fabrication of the surface ion traps measured by the QCM.

7.1.3 Evaporation of traps

First trapping experiments were performed with traps whose electrodes were fabricated with gold. For this, we evaporate a layer of 15 nm titanium for adhesion and then 350 nm gold layer. For later experiments, such as coupling to the LC-resonator, we used AlCu as the electrode material with again a 15 nm titanium adhesion layer followed by 500 nm of aluminum and finally 30 nm of copper. In each case, we evaporate these metal layers twice for a total thickness of 730 nm or 1090 nm, respectively. To prevent electric connection through the trenches, the metals are evaporated under an angle of 65° to the normal of the plane of the trap. In addition, the projection of the atom beam onto the trapping plane is oriented 45° with respect to the orientation of the trenches (see Fig. 7.1). This ensures that the atoms can never reach the bottom of a trench. The evaporation is repeated with opposite orientation with respect to the projection on the trap plane to cover all sidewalls. The 65° angle of evaporation will result in a thinner layer of metal deposited than the quartz crystal microbalance (QCM) measures. The deposition rate onto a substrate is giving by the Knudsen relation $R \propto \frac{\cos\theta}{r^2}$ where r is the distance of the substrate to the source and θ is the angle between the normal of the substrate the arriving atoms. For the QCM $\theta_{QCM} = 90°$, while it is $\theta_{trap} = 65°$ for the trap. This results in a higher thickness reading on the QCM than is actually deposited on the trap surface. We adjust the amount of evaporated material accordingly so that we deposit a layer of the thickness we want.

Another important aspect to the fabrication of the trap is the deposition rate of the metals onto the substrate. The optimal rate depends on the metal evaporated and the equipment used. With the CHA electron beam evaporator at the Marvell Nanolab at UC Berkeley, we typically use the rates in Tab. 7.1. The main limitation for increasing the rate of Al is that the BN-TiB_2 crucible holding the Al melt gets too hot and cracks. With copper and gold electron beam evaporation, we encountered a different problem when using too high evaporation rates as discussed next.

Prevention of spitting of copper and gold

At evaporation rates of $3\,\frac{\text{Å}}{\text{s}}$ both copper and gold exhibit spitting behavior. This is caused by rapid vaporization of material on the melt surface that results in the ejection of metal

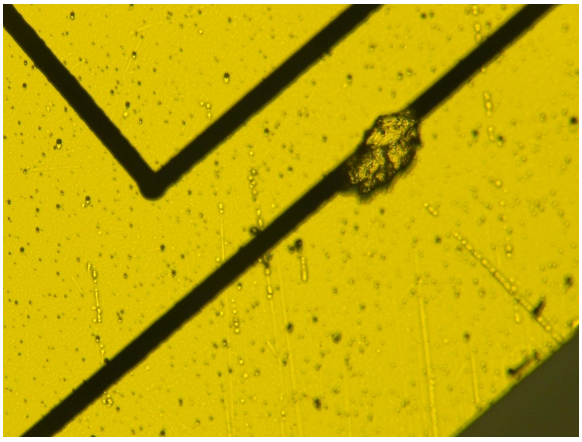

(a) Au nodule shorting a trap electrode.

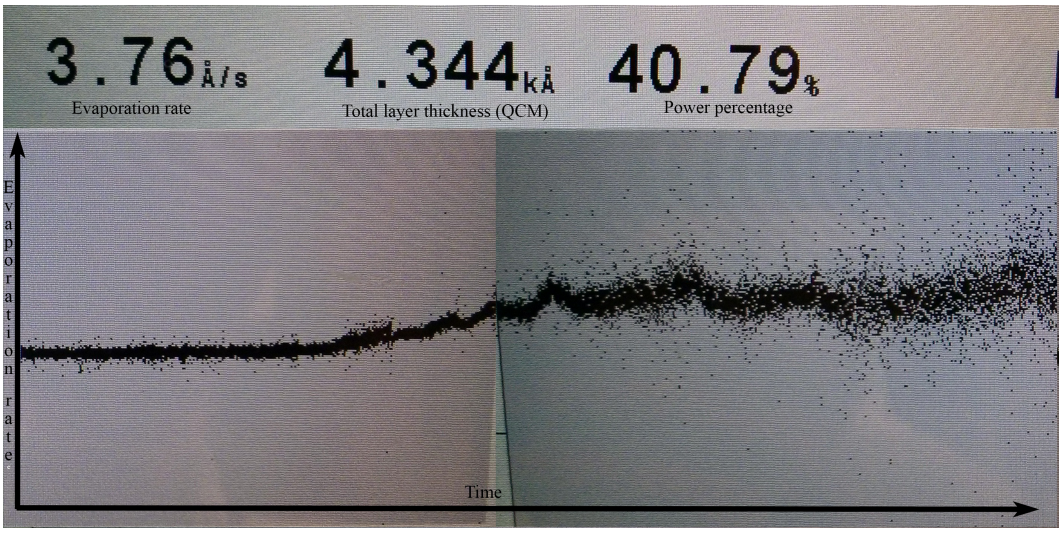

(b) The graph shows the evaporation rate of the nanolab CHA versus time. The picture was cut and stitched together to create a time axis with operating time increasing from left to right. In this run, as the time increases, the melt temperature increases. Additionally, as the melt is evaporated, carbon starts to increase in concentration. This results in an increase of fluctuations of the deposition rate.

Figure 7.2: Copper exhibits high fluctuations in deposition rates. A Fabmate® Graphite crucible was used in the evaporation run that these pictures are taken from.

particles, which deposit as nodules on the substrate [108]. These nodules can short trap electrodes, as seen in Fig. 7.2a, or change the trapping potential when they land on the center electrode close to the trapping position as they can be $10 - 20\,\mu m$ high, which is comparable with typical trapping heights of $50 - 200\,\mu m$. The cause of the ejection of nodules has been studied in the literature [109] [110]. It was found to be related to the presence of carbon in the melt. Carbon is less dense than gold and will float to the top of the melt. When electrons hit the carbon, they are reflected and can not heat the melt. With a constant electron beam size, we, therefore, need higher beam powers to maintain the same evaporation rate. The increased power density of the beam can rapidly boil the gold melt when the random movements of the carbon of the surface suddenly reveal a larger carbon-free patch [108].

Multiple strategies have been proven to alleviate this problem. So far we reduced this issue by sweeping the electron beam over a larger area to reduce the power density and reducing the evaporation rate from 3 to $1\,\frac{\text{Å}}{\text{s}}$. Further improvements are possible by using a tungsten crucible [110] or by adding tantalum to the gold melt [109]. The tantalum floats to the surface of the melt and acts as a getter for the carbon. A disadvantage of adding tantalum is that the melt can wick over the edge of the crucible, which would damage the evaporator [108].

Trap mounting

After evaporation, the trap is ready to be wire-bonded and put into the vacuum chamber. Thus, there is no need for additional processing steps and the trap does not need to come into contact with any solvents, which would contaminate the surface. We find that traps fabricated in this manner feature consistently small electric field noise with heating rates that are low as compared to with other traps with the same ion height [65]. Some of the associated heating rate measurements, including the effect of surface treatment, have been published in [65], [111], [112], and [113].

After evaporation, the trap is then mounted in a CLCC(ceramic leadless chip carrier)[1], seen in Fig. 7.3b, which has 84 contact pads and a recessed cavity in the middle. We place a $\frac{1}{8}$" Macor spacer underneath the trap chip to raise the trap out of the cavity of the CLCC so that the laser beams do not get blocked by the CLCC. Electrical connections are established with Al-1%Si, $31.73\,\mu m$ diameter wire bonds to the Au pads of the CLCC. We bond with two wire bonds per electrode to have redundancy in case of failure.

The combination of aluminum and gold is known to cause reliability issues, due to the formation of intermetallic compounds that are often visible as purple coloration [114]. This combination has five equilibrium phases: $AuAl_2$, $AuAl$, Au_2Al, Au_5Al_2, and Au_4Al. Experiments have shown that the intermetallic phases can be stronger than Au or Al. The problem with this metal combination is that voiding, the formation of cavities, can occur at the interface. These voids cause the bonds to fail [114]. The appearance of failures can be accelerated by heating the wire-bonds and as such can be problematic in setups that require

[1] PB-C86131, Kyocera

baking to reach an adequate vacuum for trapping of ions. A bond will lose its strength after 150 hours at 195°C but will last for two years at 125°C [115].

The setup described here is never heated above room temperature. The main purpose of heating a vacuum setup is to remove water and other molecules absorbed on the surfaces. These absorbed molecules would outgas over time in a room-temperature setup and limit the achievable vacuum. In our cryogenic setup, molecules freeze out and will not desorb from the chamber walls. As we avoid high temperatures, the failure of bonds due to the formation of intermetallic compounds is neglectable and failures that did appear in our setup are more likely caused by contamination of the surfaces. Bond reliability also depends on metalization thickness. For gold a thickness of 1 µm is recommended [116].

Socket and PCB assembly for quick interchangeability of traps

It is not advisable to use soldering to connect the CLCC to our filter PCB as the fumes from flux can contaminate the trap surface and removing the CLCC after it is soldered is difficult. Solder without flux is an option but those connections are not reliable and tend to break, especially with thermal cycling. Solder with a few percent of antimony content can reduce this problem [73].

Due to these restrictions, we use a mechanical solution. A Macor socket is screwed onto the filter PCB while two alignment pins make sure the socket is in the correct spot on the PCB. The CLCC is held in place with two stainless steel clamps that press it down. Electric contact is made via small springs[2], about 0.5 mm in diameter, manufactured from a fine gold-coated tungsten wire that is randomized to form so-called fuzz buttons. An example of how they look is shown in Fig. 7.3c. This process makes the fuzz button very reliable for conduction of RF and DC signals and they operate in a wide temperature range. To guard the spring during multiple connection cycles and prevent it from falling out of the socket, we put a hard hat on top of it. The hard hat, constructed from gold-plated beryllium copper, is shown in the drawing of the socket assembly in Fig. 7.3a. The entire assembly of CLCC, socket, and PCB is shown in Fig. 7.3b.

Mounting the trap on a CLCC has also the advantage that we can do all the preparation work in a cleanroom environment and we just have to drop the CLCC into our assembly. This reduces the amount of dust particles landing on the trap which can lead to shorting of trap electrodes or provide spots where charges can accumulate and lead to high stray fields.

7.2 Voltage sources

The DC voltages needed for the axial confinement of the ion are generated by a low noise DAC that is controlled by an FPGA and supply voltages between ±10 V with a 16-bit resolution (0.3 mV steps). If larger voltages are necessary, an additional Op-amp stage can

[2]Fuzz button®, Custom Interconnects LLC

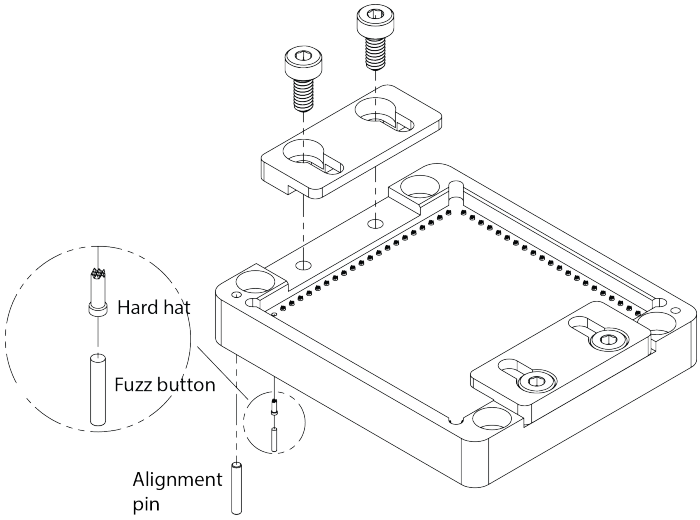

(a) Drawing of the socket that the CLCC sit in. The socket and the fuzz buttons are manufactured by custom interconnects.

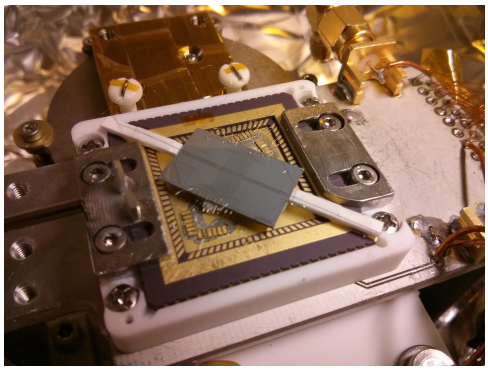

(b) Finished trap assembly.

(c) Fuzz buttons.

Figure 7.3: With the use of a socket and traps mounted on a CLCC, we can quickly change from one trap to another. The connection between the CLCC and the underlying PCB is made via Fuzz buttons.

multiply the output voltage of the DAC by a factor of four to yield ±40 V with a resolution of 1.2 mV.

The DAC output is low-pass filtered with a 3dB-point of 16 kHz utilizing RC filters inside the DAC box and an additional RC filter right before the CLCC inside the 4 K-stage of the cryostat. Typically, we have to choose a PCB material that has low outgassing rates[3] and can not take advantage of solder masks. Due to the extremely low temperatures in the cryostat outgassing is not a big concern for us since all molecules besides helium condense at the cryostat surfaces and are cryopumped. Because of this, we use PCBs with solder mask in our experiment. FR4 is also a possible material choice for our PCB, though we decided on Rogers 4350B because of its lower RF losses.

the last stage of filtering happens on the CLCC itself via 600 pF single layer capacitors[4]. The capacitors are soldered in the CLCC cavity. They are then connected to the CLCC pads and the trap via two wire bonds for each connection.

7.2.1 Electric components at cryogenic temperatures

Many electronic components have vastly different working parameters at cryogenic temperatures compared to room temperature. In particular, the drastically different behavior of semiconductors [117], capacitors [118], and resistors [76][119] needs to be understood to make sure the designed circuit works as intended. For multi-layer ceramic capacitors (MLCC) the capacitance value at 4 K can be 99% lower depending on the ceramic used. This would have a big impact on the 3dB-point of the filter. For C0G (NP0) capacitors there is no significant drop in capacitance when cooled to 4 K [118]. Ceramic capacitors are susceptible to noise cause by deformation and the piezoelectric effect. Coincidentally C0G capacitors also have no significant noise of this kind [120].

For some types of resistors, the resistance value increases with lower temperatures, which is why they can make good and cheap thermometers [76][119]. Metal film resistors have low temperature coefficients down to liquid helium temperatures [121] [122], and thus they are chosen for the filter board in the 4 K-stage. One might suspect that the resistance of a metal film resistor would drastically decline when cooled to cryogenic temperatures as seen for very pure metals. The reduction of resistivity depends on the concentration of lattice defects [73]. NiCr is often used for the fabrication of metal film resistors, but in some cases, other alloys are utilized as well. If the exact resistance value is important it is advisable to thoroughly test the specific resistors used. In our case the resistors were used as filters, as the resistance increases with decreasing temperature [122] the result will be a lower frequency 3dB-point.

[3] Rogers series laminates

[4] AVX, GH-series Microwave SLC with MAXI+ dielectric

7.2.2 RF drive

An RF generator[5] creates the RF signal for driving the ion trap. It is amplified[6] and sent through a feed-through to the 4 K-stage of the cryostat. We use a steel core coaxial cable that is thermally anchored at both the 4 K- and 40 K-stage with Stycast 2850FT. A helical resonator [75] with a resonance frequency of 36 MHz and $Q = 200$ is used to further amplify the voltage. The helical resonator is placed in the 4 K-stage as we need to minimize the capacitive load on the resonator. It has a high impedance output and additional capacitance will lower the amplitude of the RF voltage. We use a 28 mm outer diameter copper tube as a housing and close the ends with 1 mm copper sheets. At the side of the tube, we mount an SMA connector whose center pin is connected to the copper wire spiral inside the tube. The helical resonator is wound with AWG 18 copper wire which is a smaller diameter than typically used in our laboratory. We use it here as there are space constraints inside the cryostat. Due to the lower resistance of copper at cryogenic temperatures, the losses should be lower than for resonators with thicker wire at room temperature. One disadvantage is that the thinner wire is not as stiff as larger diameter wire and can be prone to vibrations changing the resonance frequency. The inside of the helical resonator is sputtered with NbN. While this step did increase the quality factor of the resonator, it is not caused by the sputtered film becoming superconducting as the improvement of the quality factor is already measurable at room temperature. We perform impedance matching of the helical resonator to the RF amplifier at room temperature by minimizing the reflections. When the cryostat is cooled down, the impedance matching barely changes and remains at an acceptable level.

The RF voltage is connected to the filter PCB using a twisted pair and then via the socket to the RF electrode. The amplitude of the RF-voltage is measured with a capacitive divider with a 1:30 division ratio as shown in Fig. 7.4. We use SMD components on a custom PCB to avoid change in the circuit performance which can happen when the wires or position of through-hole components changes. For ideal capacitors, the division ratio would be constant, though there are parasitic inductances and resistances present for real world devices, and the dielectric properties will also change for different frequencies. For this reason, we start by calibrating the division ratio for the resonance frequency of the helical resonator. The division ratio is finally calibrated once we can measure the trap frequency of the ion and determine the voltage amplitude from the BEM simulations, discussed in Sec. 4.1. We can then use the calibration of the capacitive divider to exactly measure the RF voltage amplitude in future experiments as long as the resonance frequency does not change. In our experience, changes of a couple of MHz are acceptable and do not influence the division ratio by more than a few percent.

[5] Marconi 2024
[6] Minicircuits, ZHL-1-2W+

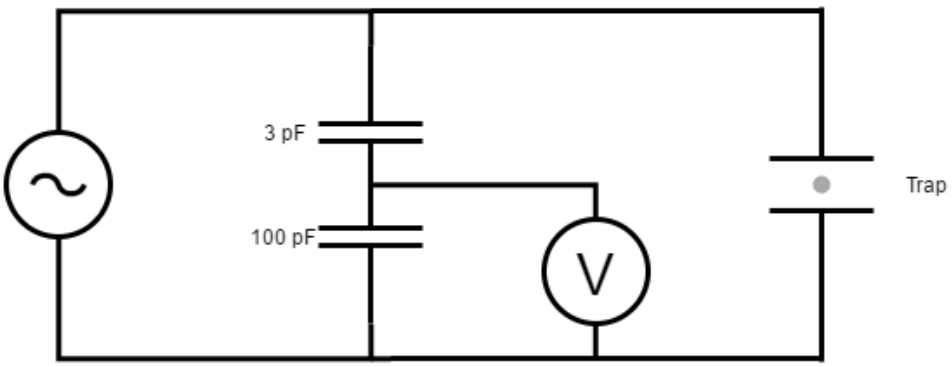

Figure 7.4: Circuit diagram for the capacitive divider used to measure the amplitude of the RF drive.

7.3 Ca-oven

In the room temperature setups in our group the Ca-oven, used to generate a beam of Ca atoms, is typically built from a 316 stainless steel tube with a tantalum foil spot welded on and filled with Ca granules [123]. With a current of 3 A and $1 - 2$ V this type of oven generally creates a sufficient amount of Ca at the trapping volume to photo-ionize [43]. In a cryogenic setup, this is a significant heat load which can raise the operating temperatures of the cryostat. For an optimally sized pair of conductors the heat load can be calculated by [73]

$$\frac{\dot{q}_{\mathrm{min,77–4\,K}}}{I} = 18\,\frac{\mathrm{mW}}{\mathrm{I}}\,. \tag{7.1}$$

This is in addition to the heat load of heating the stainless steel tube to a temperature with a high enough vapor pressure of the calcium.

We instead used a different oven design. In our design, a 1.8 mm steel tube is filled with Calcium granules and slightly compressed to prevent it from falling out. As a heat source, we use a fiber coupled NIR laser at 793 nm that is focused into the steel tube. A fine adjustment of the beam pointing is then performed while looking for neutral Ca fluorescence, maximizing the fluorescence signal with the least amount of optical power. The optical power necessary for loading the ion trap can be routinely reduced to 100 mW.

After multiple successful experiments with the laser heated oven, we also discovered some downsides. The design is more sensitive to the alignment of the steel tube as the laser has to directly hit the calcium grain or a much higher laser power of up to 2 W is required to generate a sufficient Ca flux. The calcium granules should also be fresh and not have an oxide film on their surface, as in that case, the CaO will need to be cracked first, which requires a higher power. Similar behavior is seen in the current heated design for which we need to increase the oven current a few ampere over the steady state value for the first-time operation of a freshly built oven.

Because of these downsides, we eventually also decided to use the more traditional cal-

cium oven design. Due to the high heat load, we place the oven outside the 40 K heat shield and mount it on an adjustable bellow. The bellow can be adjusted and held in place with locking nuts on threaded rods. We remove the window on the 40 K-heat shield on the oven side to have a 1" diameter opening for the calcium beam. On the 4 K-heat shield, we place an aluminum disk with a position adjustable 1 mm hole. This opening we adjust so that the calcium beam is directed above the trap to avoid shorting electrodes.

7.4 Trap frequency stabilization

For initial experiments, we want to achieve an efficient energy transfer from the LC resonator to the ion. In a typical Paul trap, the radial trap frequencies fluctuate due to instabilities of the RF voltage. We ideally need to reduce these fluctuations, so that $\Delta\omega_{\mathrm{LC}} > \Delta\omega_y$, meaning the width of the resonator resonance is larger than trap frequency noise. Additionally, we also want to eliminate slower drifts of the trap frequency, keeping both oscillators in resonance for the entire duration of an exchange t_π, as well as over the course of multiple experiments as each experiment is typically repeated hundreds of times to generate enough statistics.

The secular frequency of a trapped ion is dependent on both the DC and RF voltage applied to the trap electrodes. The DC voltage can be kept stable with filtering of the electrodes which is not straightforward for the RF voltage. If we neglect the contribution of the DC voltage to the radial secular frequencies we find

$$\omega_i = \alpha_i \left(\frac{\sqrt{2} e V_0}{m D_{\mathrm{eff}}^2 \Omega} \right) \tag{7.2}$$

The width of the resonator is set by its quality factor. As a result, we find $\Delta\omega_{\mathrm{LC}} = \frac{\omega_{\mathrm{LC}}}{Q} > \Delta\omega_y$ from which follows that we need to stabilize the fractional trap frequency to better than $\frac{1}{Q}$ for an optimal energy transfer. For the coils we use with our current experiments, this translates to a frequency stability of one part in 10^4, which directly translates to an RF voltage stability on the same order according to Eq. 7.2.

7.4.1 The RF voltage stabilization circuit

We stabilize the RF voltage by connecting a voltage controlled attenuator[7] between the signal generator and the amplifier. The applied RF voltage is measured after the helical resonator with a capacitive divider that feeds a rectifying circuit, whose output is used as the sensor voltage in a PID controller as seen in Fig. 7.5. A similar approach can be found in [124]. Approaches for increasing the temperature stability of the rectifying circuit are shown in Fig. 7.6. The simplest version is using a diode[8] as a self-biasing half-wave rectifier,

[7] Minicircuits, ZX73-2500+

[8] 1N4148

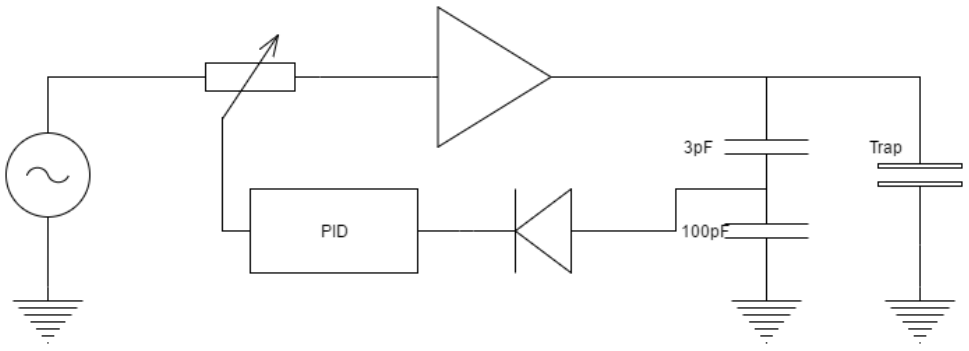

Figure 7.5: The RF stabilization setup. The RF voltage applied to the trap is measured with a capacitive divider and rectified before being fed to a PID controller whose output regulates a voltage variable attenuator.

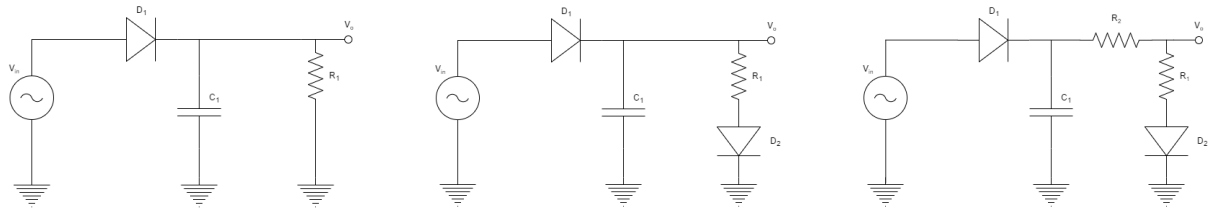

(a) (b) (c)

Figure 7.6: Construction of a temperature insensitive rectifying circuit for RF stabilization with increasing temperature stability from a) to c).

which works well for RF power levels above 0 dBm [125]. The output equivalence circuit of the diode can be modeled as a voltage source with a series resistor R_j and the output voltage becomes

$$V_0 = V_{\text{rectified}} \frac{R_1}{R_1 + R_j} \,. \tag{7.3}$$

For small signal powers, the junction resistance R_j is

$$R_j = \frac{nk_BT}{q(I_s + I_b)} \tag{7.4}$$

with n the diode ideality factor, the Boltzmann's constant k_B, the diode saturation current I_s, and the external bias current I_b. For low input powers $R_j > R_1$, which lowers the output voltage and will also result in a temperature dependence. We add another diode D_2, whose junction resistance also follows Eq. 7.4. The rectifying current produced in D_1 also flows through D_2, which has a similar junction resistance as D_1 resulting in a higher output voltage V_0. An even better temperature stability is achieved by using a variable voltage divider as opposed to a DC load. The voltage divider is constructed by adding resistor R_2 to the circuit as in Fig. 7.6c. This option reduces the output voltage V_0 in the case of high RF powers when R_j becomes small compared to R_1 and R_2. However, this is not a concern in our case as the RF powers are too small to run into this problem.

To further improve the operation of the circuit, we mount the two diodes D_1 and D_2 and resistors R_1 and R_2 on a thermoelectric cooler and stabilize the temperature. The circuit elements are mounted using Stycast 2850FT epoxy and the other side of the thermoelectric cooler is mounted directly onto the aluminum box so that the box can act as a heat sink.

7.4.2 Measurement of the trap frequency

There are multiple ways to measure the trap frequency of an ion. One widely used method is using laser pulses to drive a red or blue sideband transition (see Sec. 2.5.2). We find the sideband frequency by measuring a spectrum of the $4^2S_{1/2} \rightarrow 3^2D_{5/2}$ with an additional offset of the estimated trap frequency, effectively driving a sideband transition. The disadvantage of this method is that our cavity[9] [42] to which the probe laser is stabilized drifts typically with a rate of 1 $\frac{\text{Hz}}{\text{s}}$, though the drifts can be as high as 10 $\frac{\text{Hz}}{\text{s}}$. This directly corresponds to a measurement error of the trap frequency as we typically only perform a measurement to correct for drifts every 6 minutes.

An alternative method that is insensitive to the laser drifts is the pulsed heating technique [126][30]. For this method, we pulse the 397 nm laser with a square wave of a duty-cycle of 50% and shine it onto the ion for a couple milliseconds. We then scan the frequency of the square wave across the suspected trap frequency. On resonance with the trap frequency, the pulses lead to parametric heating of the ion motion. The force of photons scattering from

[9] Stable Laser Systems

the ion displaces the ion from its equilibrium position by [30]

$$x_{i,eq} = \frac{\hbar k \Gamma \rho_{ee}}{\hbar \omega_i} = \frac{\hbar k \Gamma}{2\hbar \omega_i} \,. \tag{7.5}$$

We assume the laser is switched on when the ion is at the turning point of its oscillation cycle and that the laser highly saturates the transition. The ion is then displaced by $2Nx_{i,eq}$ after half of its oscillation cycle when we switch the laser off. After N laser pulses the ion motional amplitude is $x_{i,N} = x_{i,0} + 2Nx_{i,eq}$ with an energy

$$E_N = \frac{1}{2} m\omega_i^2 (x_{i,0} + 2Nx_{i,eq})^2 \tag{7.6}$$

and the energy of the ion rises quadratically with the number of pulses.

If the pulsing frequency is not the trap frequency of the ion, the ion motion, and the pulses get out of synchronization and the ion is again displaced towards $x_{i,0}$. As a result, the mean population number $\bar{n}$ is much smaller if the pulsing does not happen on resonance with the trap frequency.

To detect if the pulses heated the ion motion, we drive a blue sideband pulse as described in Sec. 2.5.2. The strength of carrier and sideband transitions have different dependencies on the motional state population n, and for high n, the sideband transitions can have a larger Rabi frequency than the carrier transitions [54]. It follows that if the pulsed 397 nm laser did not cause a large increase of the motional state n, the probability of finding the ion in the excited state $|D, n+1\rangle$ is not as high. The results of such a measurement can be seen in Fig. 7.7. With this method, we can determine the trap frequency with a precision of about 100 Hz. The spectroscopy method is far less precise, depending on the drift rate of the cavity and the measurement time, which is about 1 minute and the error can be up to 3 kHz.

7.4.3 Results of RF stabilization

The benefit of RF stabilization can be seen in Fig. 7.7b. The variation of the trap frequency in Fig. 7.7a tracks the temperature measured in the lab, which varies about $1 - 2$ K with a period of roughly one hour. This temperature fluctuation can, in turn, affect the RF amplifiers and the performance of various other electronics. The 2 kHz amplitude of the fluctuations corresponds to a frequency stability of $\frac{\Delta\omega}{\omega} \approx 10^{-3}$. After feeding back on the RF power, the radial trap frequency was stable to within 100 Hz resulting in a relative trap frequency stability of $\frac{\Delta\omega}{\omega} \approx 10^{-4}$. The rectifying circuit used for these measurements is the one in Fig. 7.6b, which was later replaced with the one in Fig. 7.6c for further improvement, though we do not have the data on its performance so far.

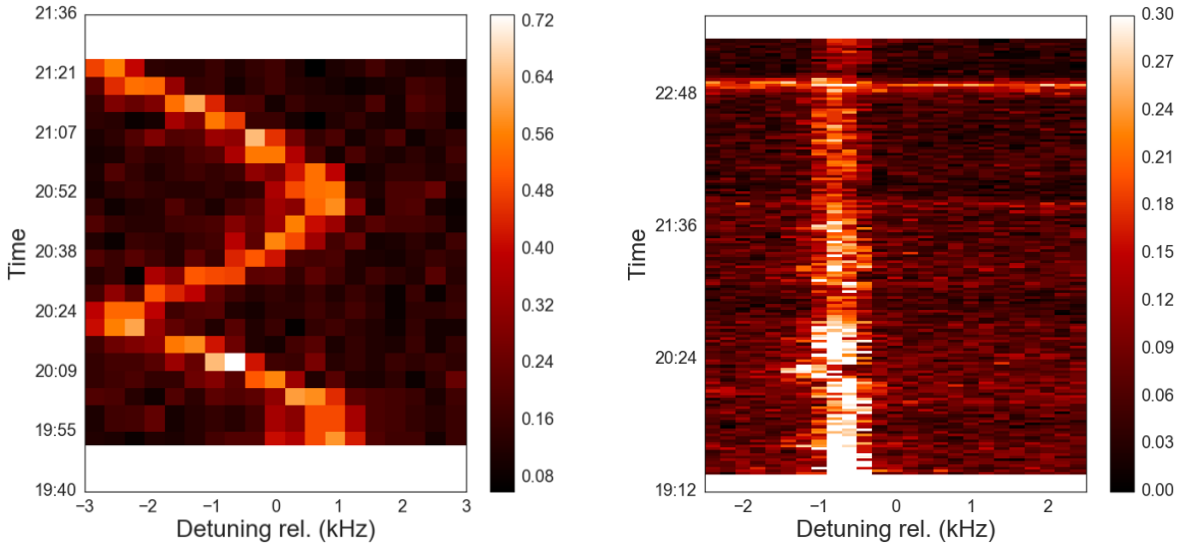

(a) without RF stabilization.

(b) using the stabilization circuit in figure 7.6b.

Figure 7.7: Variation of the radial trap frequency measured over the course of a few hours without (a) and with (b) RF stabilization. These measurements were taken in a macroscopic trap described in [30].

8 Trap operation and coupling

In this chapter, we will discuss our experience operating the experiment and initial results of the coupling experiments.

8.1 Trap operation

After completing the setup of the cryostat, we tried trapping with multiple traps that had a coupling wire height of 250 µm. The mounting of the wire was as described in Sec. 4.3. All our attempts were unsuccessful until we removed the wire. Once we trapped an ion, we measured the trap frequency by pulsed heating (see Sec. 7.4.2), finding the same axial frequency as predicted by simulations to within $\frac{\delta\omega}{\omega} = 10^{-3}$. Since the axial trap frequency is defined only by the DC electrodes, we confirmed the intended voltages arrive at the trap electrodes and also that the simulations accurately model our ion trap.

When again placing the coupling wire on top of the trap, we discovered the closest ion-wire distance, which still allowed for trapping, to be 507 µm. For further experiments, we used this distance in our traps. A trial of having the wire perpendicular to the trap axis and shuttle the ion in towards the wire proved unsuccessful because we would lose the ion in close proximity needed for coupling to the LC resonator. Close to the wire we would lose the ion and be unable to reload the trap.

Once trapped, the ion lifetime we would lose the ion only when attempting something new and creating unstable conditions. Otherwise, the ion stays in the trap for multiple hours until we would switch off the lasers. We could keep the ion for about ten minutes without Doppler cooling. This estimate is based only one very few experiments, as it is time-consuming to conduct. Additionally, we tested how long we could keep the ion after switching off the cryostat and letting it warm up. The ion would reproducibly disappear at roughly 13 K, likely because of increasing pressure when gas frozen out at the walls reevaporates.

8.1.1 Micromotion compensation

The source of micromotion, an additional driven oscillation of the ion with the drive frequency, has already been discussed in Sec. 2.1. Here we will cover how to minimize its amplitude. Compensation of excess micromotion is an essential first step in ion trapping experiments as it broadens the Doppler cooling line thereby increasing the Doppler-cooling limit. Additionally, a large micromotion amplitude can lead to additional heating [55] and increase the Lamb-Dicke factor to $\eta\left(1-\frac{\omega}{2\sqrt{2}\Omega_{RF}}\right)$ [55]. Excessively large stray field might even prevent trapping at all.

Compensation of micromotion typically follows the route of detecting the amplitude of the micromotion and testing what compensation fields are needed to reduce that amplitude. Progressively more sensitive methods of detection are used to reduce the micromotion amplitude to the minimum value possible. Some methods of detecting micromotion in surface traps are also discussed in [106]. We use the following methods in order of increasing sensitivity.

Ion movement detection

The first method we use to detect the micromotion is increasing the RF voltage amplitude. The stronger confinement pushes the ion closer to the RF null and so we learn in which direction it lies. This works best in the horizontal direction, that is in this direction, as the movement of the ion is directly visible on the camera. In the vertical direction, one has to move the objective to refocus the ion to learn which direction the ion has moved. We then reduce the RF amplitude back to the original value and use the compensation fields to push the ion in the same direction as it was moving with the higher amplitude. This is repeated until the ion does not move anymore with the increase of RF voltage.

Linewidth reduction method

The next iteration to reduce the micromotion is achieved by reducing the line width of the $4^2S_{1/2} \rightarrow 4^2P_{1/2}$ transition. We detune the laser to the red until the counts from fluorescence are about half of the on-resonance value while keeping the laser intensity at about one-third of the saturation intensity. Then we vary the compensation fields to minimize the fluorescence signal.

The first-order Doppler shift alters the spectrum of the transition. The steady-state solution for the excited state population P_e is [127]

$$P_e = \left(\frac{\mathcal{P}|E_0|}{\hbar}\right)^2 \sum_{n=-\infty}^{\infty} \frac{J_n^2(\beta)}{(\omega_0 - \omega_{\text{laser}} + n\Omega)^2 + (0.5\Gamma)^2} \,. \tag{8.1}$$

We plot $P_e' = P_e\left(\frac{\hbar\Gamma}{2\mathcal{P}|E_0|}\right)$ for different magnitudes of micromotion, measured by the modulation index β. We assume laser powers below the saturation limit, with a parameter

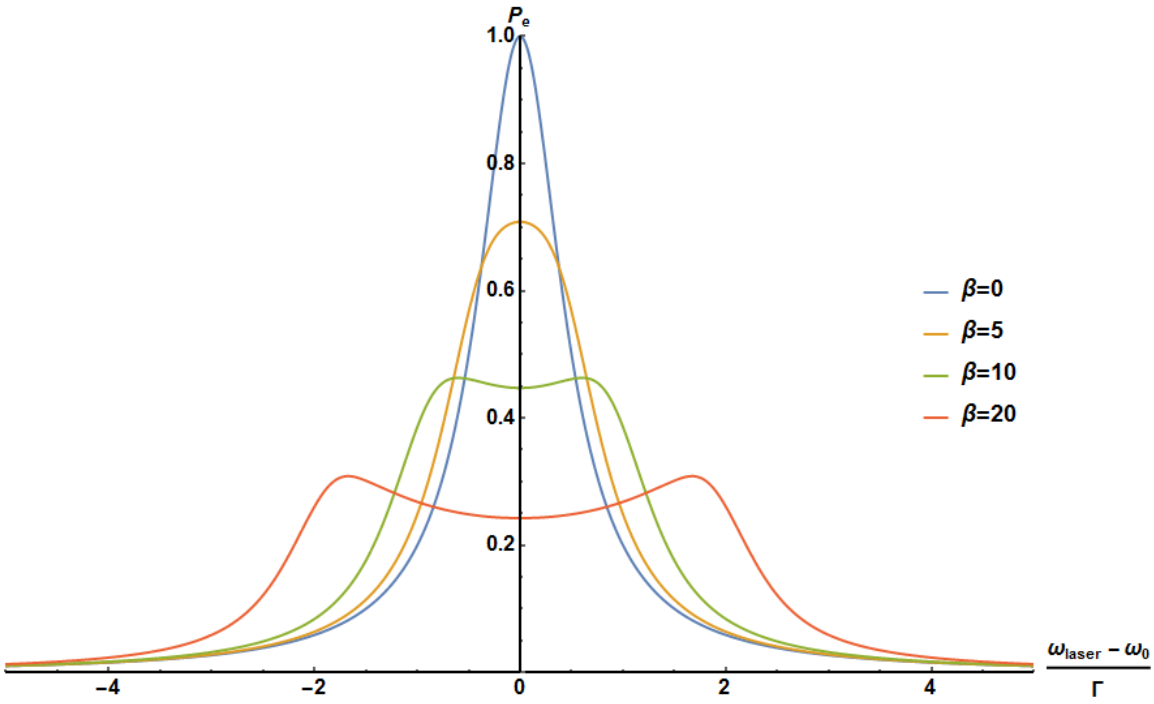

Figure 8.1: Simulation of the scattering rate for different amplitudes of micromotion and detuning. The micromotion amplitude increases in the order blue, orange, green, and red [127].

$\frac{\Omega}{\Gamma} = 0.1$. The resulting plot is shown in Fig. 8.1 and we see that the fluorescence signal will decrease as we reduce the micromotion amplitude. We also notice that for large micromotion amplitudes a further detuning from resonance is necessary to measure a decrease in fluorescence with increasing compensation.

This method of micromotion compensation only works if the laser has a projection on the trap axis for which we want to compensate micromotion and so it is not effective for the vertical direction.

Resolved micromotion sideband method

One sensitive method of compensating excess micromotion is to compare the Rabi frequency of the carrier transition to that of the micromotion sideband [54]. We first determine the Rabi frequencies of the carrier Ω_0 and the first micromotion sideband Ω_1. This then allows us to calculate the modulation index β in the limit of low modulation via [54]

$$\frac{\Omega_0}{\Omega_1} = \frac{J_1(\beta)}{J_0(\beta)} = \frac{\beta}{2} + O(\beta^2)\,. \tag{8.2}$$

We then adjust the compensation fields to minimize the modulation index.

While this is more sensitive than the previous method, it is also only possible in the case of a projection of the 729 nm laser on the micromotion.

8.1.2 Build up of stray fields

In previous surface ion trap experiments, we gathered some experience with what magnitude of stray fields to expect. They tend to be $< 1 \frac{\mathrm{V}}{\mathrm{mm}}$ even for traps that have been in operation for multiple months. In some experiments, the ion trap's continuous active use over a period of months was shown to increase the magnitude of the stray fields [106]. In earlier experiments, we found that the stray fields are highest in the area of the trap where ions have been continuously trapped [106]. The surfaces below the ion charge to higher fields with a larger electric field noise spectral density. The exact mechanisms of both the charging and the field noise are uncertain but laser light has been observed [106][41].

The first trap to successfully trap ions in the cryostat used a manufacturing process identical to the trap discussed in [106] and [105]. The trap electrodes were patterned with photolithography and their thickness increased by electroplating the trap electrodes with gold. The traps we used were produced at the same time as the ones discussed in the references, though they have been sitting in the laboratory air for about five years, which might have changed their surface composition by adsorbing molecules.

When we first trapped ions in the trap, we found stray fields comparable with Ref. [106] of $E_x \approx 0.28 \frac{\mathrm{V}}{\mathrm{mm}}$ and $E_y \approx -0.06 \frac{\mathrm{V}}{\mathrm{mm}}$. The fields were detected with the linewidth reduction method.

Five days later we again trapped again after several unsuccessful trials earlier finding compensation fields of $E_x \approx 0.07 \frac{\mathrm{V}}{\mathrm{mm}}$ and $E_y \approx -1.3 \frac{\mathrm{V}}{\mathrm{mm}}$, a much larger change than expected after just such a short time. With these stray field in the vertical direction, trapping ions was no longer possible with the compensation fields successfully used a few days before. We note that during the intermediate time, the RF drive and the lasers had been switched off for the night. We observed an increase of the stray fields from the time we switched off the lasers to when we again trapped a couple of days later. If the jump in stray fields were solely due to the presence of the light, we would observe a rapidly charging stray field during the trap operation. While UV and visible laser light has previously been demonstrated as one possible charging mechanism [41], here an additional process seems also involved.

Trapping again three days later, we again found the stray fields had increased further and with the same polarity finding a compensation field of $E_y \approx -3.8 \frac{\mathrm{V}}{\mathrm{mm}}$. We, again, had to guess the magnitude of the vertical stray field. Trapping with the previous parameters was no longer possible.

Investigation of possible stray field sources

In other experiments in our laboratory, we observed charging of the bottom viewport causing stray fields. In those experiments, a UV LED was used to successfully discharge the viewport, this solution that was not helpful in our case.

Also heating the trap with 1 W of optical power to 14 K did not change the compensation voltages needed. We did, however, manage to charge up the trap by shining 200 µW of 375 nm light onto the trap to the degree that the ion moved about an ion diameter on the camera at an axial trap frequency of 500 kHz and a horizontal trap frequency of 1.43 MHz.

Warming the cryostat up to room temperature and cooling it back down for trapping resets the charging process. Loading again after thermal cycling we found a compensation field of $E_y = 0 - -0.2\,\frac{\mathrm{V}}{\mathrm{mm}}$ and a field close to zero for E_x. After initially trapping with low stray fields, the fields increase again to larger and larger values over the course of days, similar to the increase described earlier. The polarity of the stray fields was consistent with previous trapping attempts, which means it is likely that we create charges of a specific polarity. Since we do not know the location of the charges, we can only deduce from the negative compensation field needed in the vertical direction, that we either create negatively charged areas on the viewport or positively charged areas on the trap.

Charging in later traps

After initial trapping, we continued working with the newer generation of traps discussed in Sec. 7.1. Similar charging behavior was seen with these traps with evaporated gold and copper-aluminum electrodes. For most of the experiments, we operated the traps right after cooling down to avoid extremely high stray fields. The polarity of the fields was typically as described earlier, though in a couple of cases for an unknown reason we observed a field with opposite polarity.

8.2 Heating the ion with the LC resonator

The most straightforward initial experiment to demonstrate coupling between the two oscillators is to measure the increased heating of the ion in resonance with one of the modes of the LC resonator. The resonator mode is coupled to a bath at the temperature of the cryostat between 6-9 K. On the other hand, we have the ion, which we can cool to a much lower temperature of $T_D = 0.5$ mK. The contribution of the resonator mode to the heating rate of the trapped ion on resonance can be calculated from 3.14:

$$\dot{\bar{n}}_{\mathrm{ion}} = \frac{d}{dt}\bar{n}_{\mathrm{bath}}\left(1 - e^{-\gamma t}\right) = \bar{n}_{\mathrm{bath}}\gamma e^{-\gamma t}\,. \tag{8.3}$$

With $\bar{n} = 65,000$ for a frequency of $\omega_i = 2\pi \times 2.64\,\mathrm{MHz}$ and a temperature of 8 K and the damping constant γ (Sec. 3.3).

The trap used in this experiment had a NbTi wire suspended 507 µm above the trap corresponding to a $D_{\mathrm{eff,y}} = 910\,\mu\mathrm{m}$ for the vertical ion motion. The trapping height was 164 µm. The LC resonator had an inductance of 0.56 mH, calculated from the estimated 160 windings resulting from the winding speed selected and the length of the coil former. We calculate a coupling constant of $g_y = 2\pi \times 42\,\mathrm{Hz}$ for these parameters. The trapping

height and the wire height were chosen due to previous problems trapping ions closer to the coupling wire.

The effective distance for the horizontal trap axis is much larger since the ion-wire distance hardly changes. We find an effective distance $D_{\mathrm{eff,x}} = 6100\,\mu\mathrm{m}$, resulting in a coupling constant $g_y = 2\pi \times 6.2\,\mathrm{Hz}$.

We replaced the previously used measurement board with a Nb-tube crimp secured on a 22 AWG, Kapton-insulated copper wire held in place with PTFE tape. The copper wire is then connected to a coaxial cable similar to the setup in Fig. 6.11. This setup allows us to measure the resonance frequency just before the coupling experiment as it fluctuates by tens of kilohertz between cool-downs. In the experiment described here, the fundamental frequency of the LC resonator was 2.64 MHz.

The heating rate of the ion was measured as we altered the RF drive power to change the secular trap frequency of the ion. We determine the heating rate on resonance and to either side of it, to verify that the elevated heating rate does not come from electrical noise but follows the resonance of the LC resonator. To calculate the heating rate, we determine the mean motional occupation number for different waiting times t after Doppler cooling. The mean occupation $\bar{n}_t$ is measured via carrier rabi flops as discussed in Sec. 2.5.1. For measurements close to the resonance of the LC resonator the maximum wait time used is 50 ms as we observe a saturation behavior for longer wait times. The saturation behavior is a sign that we are no longer in the Lamb-Dicke regime, $\eta^2(2n+1) \ll 1$, and driving carrier Rabi flops is no longer a reliable method for determining $\bar{n}$. A linear fit is then used to calculate the heating rate from the measurement of the various $\bar{n}_t$.

For the vertical transversal mode of the ion, we measure a maximum heating rate of $\dot{\bar{n}}_{\mathrm{y}} = 220 \pm 15\,\frac{\mathrm{phonons}}{\mathrm{ms}}$. The expected heating rate depends on a calculated the value of the resonator inductance and an estimation of the quality factor of the resonator mode. The main uncertainty for a calculation of the theoretically predicted value of the heating rate is the quality factor of the resonant mode. From 8.3 we calculate that for the inductance of the resonator and the simulated D_{eff}, Q=800 would result in the observed heating rate. This estimated Q is in good agreement with the range of previously measured quality factors for this LC resonator. The measured heating rate of the vertical direction for multiple trap frequencies is plotted in Fig. 8.2.

For the horizontal direction, which is plotted with blue squares in Fig. 8.2, we observe $\dot{\bar{n}}_x = 6 \pm 0.4\,\frac{\mathrm{phonons}}{\mathrm{ms}}$. Off-resonance we measure for both the vertical and horizontal direction a heating rate of $\dot{\bar{n}} = 0.5\,\frac{\mathrm{phonons}}{\mathrm{ms}}$.

A further method to verify the simulated values of the coupling constant and our model is to examine the ratio of the measured heating rates. To remove the uncertainty of the LC resonator Q we can examine ratios derived from 3.18 and 8.3:

$$\begin{aligned} \frac{\dot{\bar{n}}_{\mathrm{y}}}{\dot{\bar{n}}_{\mathrm{x}}} &= \frac{220}{6} = 37 \pm 3 \\ \frac{g_{\mathrm{y}}^2}{g_{\mathrm{x}}^2} &= \frac{42^2}{6.2^2} = 46\,. \end{aligned} \tag{8.4}$$

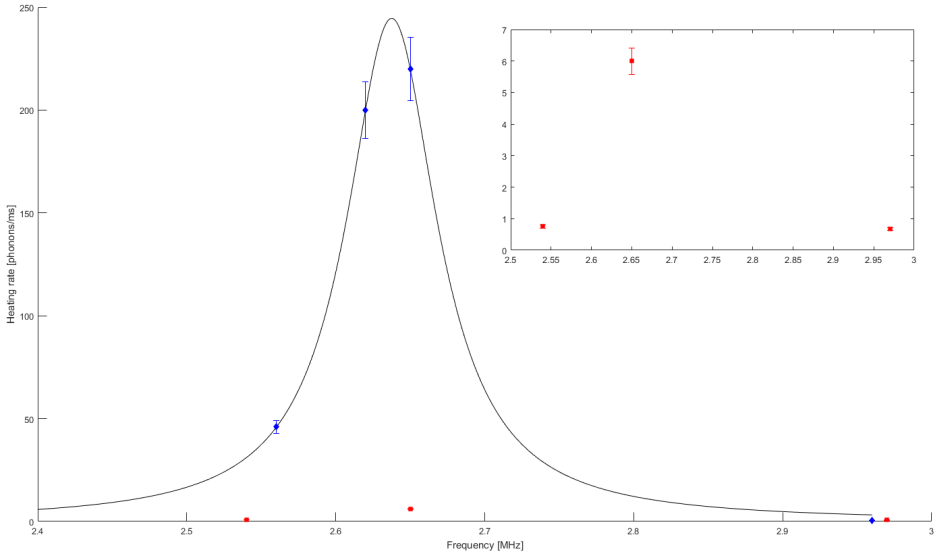

Figure 8.2: Measurement of the heating rate for various RF drive powers, resulting in different trap frequencies. Blue data points are the heating rates measured in the vertical direction, towards the suspended wire. The red data points are the heating rates measured in the horizontal direction. The ion is in resonance with the coil for a trap frequency of approximately 2.63 MHz, determined by fitting a Lorentzian to the data points.

The calculation of the ratios depends on us measuring the heating rates on resonance. Ideally, we would measure for multiple secular frequencies and then perform a fit to find the on resonance heating rate. We rely on tuning to the resonance with the RF drive for the horizontal direction ss we do not have enough data points to perform a fit. The Rf drive power was varied in 0.1 dBm steps corresponding to a secular frequency change of 30 kHz. As a result, we could easily miss the exact resonance. Considering this limitation the agreement of the two ratios is a promising first step and more detailed experiments should be conducted to confirm our model for the coupling rate. The error of the heating rate ratios was determined by propagation of uncertainties.

With the presence of these high heating rates and the resulting uncertainties of the measurements, more careful measurements should be taken to further validate these promising first results. After making improvements to the resonator design, specifically the thermal anchoring of all parts of the NbTi wire, a high Q coil will allow us to measure the quality factor of the coil while connected to the trap as well as increase the motional heating the ion experiences.

The width of the frequency range with elevated heating rates should reflect the quality factor of the LC resonator. With a fundamental resonance at $f_0 = 2.64\,\mathrm{MHz}$ and $Q = 800$ as calculated from the measurements, we expect a full-width half maximum of $\Delta f = 3\,\mathrm{kHz}$. The width of the frequency range, we observed increased heating rates in, is much larger than the expected width. One possible explanation is a higher noise temperature than the 8 K bath temperature of the cryostat. When measuring the response of the LC resonator, we observed voltage spikes with an amplitude of roughly 100 mV that would last for fractions of a microsecond and would repeat randomly with a time of tens of milliseconds between the voltage spikes. The source of these spikes is unknown. These or other effects could cause excess electrical noise. Assuming we did not tune the ion exactly into resonance but rather measured to either side of it, we fit a Lorentz profile to the data points. The width of the fitted profile is 90 kHz with a center at 2.63 MHz, though due to few data points with high error, this result should only be treated as preliminary, but it suggests another cause for the larger than expected width of the heating effect.

Further experiments should also investigate if the horizontal mode has a similar width as the vertical mode.

9 Summary and outlook

In this thesis, we discussed the first steps to building a hybrid quantum system consisting of trapped ions and superconducting transmission lines. This opens up the possibilities of coupling trapped ions to superconducting qubits and would allow combining the advantages of both trapped ion and superconducting qubits to build a more capable quantum computer.

In the course of this thesis, we discussed how the ion can be described as a lumped element LC resonance circuit, which allows us to view the ion-resonator system as two coupled LC resonators. We further explained how to calculate the coupling constant from the electric dipole moment of the ion.

We described novel ion traps, which maximize the coupling constant by reducing the equivalent inductance of the ion. Besides improving the coupling by trapping more ions or lighter atoms, the main metric to minimize is D_{eff}, the effective distance. The most straightforward way of achieving this goal is to reduce the trapping height. Another possibility is an additional coupling electrode above the ion.

In the experimental part of the thesis, we discussed the construction of the cryostat used to cool the LC resonator below T_{C} to reach its superconducting state. The low temperature has the added benefit of reducing the heating rate of the ion motion due to anomalous heating by two orders of magnitude.

For the resonator itself, it is important to note that it behaves as a distributed circuit element instead of a lumped circuit LC resonator. This is evident in the multiple higher harmonics we observed. We review how we can theoretically model the multiple resonances of the resonator. Furthermore, we explain the design considerations for the wire, insulation, and other choices, as well as show the results of our quality factor measurements.

Next, we discuss in detail the fabrication of the surface traps used for our experiments and the trap assembly utilized in the cryostat. We also examine the voltage sources used to create the confining potential, as well as discuss how we stabilize the RF amplitude in order to stabilize the trap frequency.

Finally, we give an overview of our experience trapping ions in the setup and first results of coupling the resonator to an ion.

There are multiple aspects of this experiment that merit further investigation. We used to routinely attain quality factors that were competitive with quality factors realized in other laboratories, after initial success our quality factors are consistently two orders of magnitude lower than in the past. Recovering the original quality factors would allow us to proceed further towards the goal of coherently exchanging excitation or cool one of the resonator modes.

The first demonstration of heating the ion with the resonator mode was shown in a trap configuration with a D_{eff} a factor of three larger than possible with trapping heights already demonstrated in other experiments. An additional improvement in this configuration is possible as the NbTi coupling wire was not superconducting in that experiment. The wire was not thermally anchored as we later found out, to assure superconductivity it needs to be in direct contact with a cold surface. The best solution would be to replace it with a copper or silver wire, a solution that was successful in reducing the DC resistance of the LC resonator. Alternatively, we could use a trap design without a coupling wire, which would simplify the setup greatly while only resulting in a small penalty for the coupling constant.

The experiment also confirmed the simulation of the coupling constant. While the exact Q of the LC resonator mode during the experiment was not known, we observe an increase in the heating rate while coupling to the horizontal and vertical motion of the ion. The smaller increase in the heating rate while coupling to the horizontal motion matches the theoretical prediction.

After these preliminary demonstrations, the next step will be to show cooling of the LC resonator mode, proving that we are in the strong coupling regime. Another useful demonstration would be to demonstrate parametric coupling to a higher harmonic or a resonator with a fundamental frequency larger than the ion because this will be necessary when coupling ions to superconducting qubits.

Finally, I would like to thank you, the reader, for showing an interest in this work and reading it all the way to the end.

Bibliography

[1] Jean E Sansonetti and WC Martin. Handbook of basic atomic spectroscopic data. *J.Phys. Chem. Ref. Data*, 34(4):1559–2259, 2005.

[2] Richard P Feynman. Simulating physics with computers. *International journal of theoretical physics*, 21(6):467–488, 1982.

[3] David Deutsch. Quantum computational networks. In *Proceedings of the Royal Society of London A: Mathematical, Physical and Engineering Sciences*, volume 425, pages 73–90. The Royal Society, 1989.

[4] Peter W Shor. Algorithms for quantum computation: Discrete logarithms and factoring. In *Foundations of Computer Science, 1994 Proceedings., 35th Annual Symposium on*, pages 124–134. IEEE, 1994.

[5] David P DiVincenzo et al. The physical implementation of quantum computation. *arXiv preprint quant-ph/0002077*, 2000.

[6] Thaddeus D Ladd, Fedor Jelezko, Raymond Laflamme, Yasunobu Nakamura, Christopher Monroe, and Jeremy L O'Brien. Quantum computers. *Nature*, 464(7285):45–53, 2010.

[7] Rainer Blatt and David Wineland. Entangled states of trapped atomic ions. *Nature*, 453(7198):1008–1015, 2008.

[8] Hartmut Häffner, Christian F Roos, and Rainer Blatt. Quantum computing with trapped ions. *Physics reports*, 469(4):155–203, 2008.

[9] Juan I Cirac and Peter Zoller. Quantum computations with cold trapped ions. *Physical review letters*, 74(20):4091, 1995.

[10] Jan Benhelm, Gerhard Kirchmair, Christian F Roos, and Rainer Blatt. Towards fault-tolerant quantum computing with trapped ions. *Nature Physics*, 4(6):463–466, 2008.

[11] Philipp Schindler, Julio T Barreiro, Thomas Monz, Volckmar Nebendahl, Daniel Nigg, Michael Chwalla, Markus Hennrich, and Rainer Blatt. Experimental repetitive quantum error correction. *Science*, 332(6033):1059–1061, 2011.

[12] David Kielpinski, Chris Monroe, and David J Wineland. Architecture for a large-scale ion-trap quantum computer. *Nature*, 417(6890):709–711, 2002.

[13] Chris Monroe. Quantum information processing with atoms and photons. *Nature*, 416(6877):238–246, 2002.

[14] David Kielpinski, V Meyer, MA Rowe, CA Sackett, WM Itano, C Monroe, and DJ Wineland. A decoherence-free quantum memory using trapped ions. *Science*, 291(5506):1013–1015, 2001.

[15] Lilian Childress and Ronald Hanson. Diamond NV centers for quantum computing and quantum networks. *MRS bulletin*, 38(02):134–138, 2013.

[16] John Clarke and Frank K Wilhelm. Superconducting quantum bits. *Nature*, 453(7198):1031–1042, 2008.

[17] L Tian, P Rabl, R Blatt, and P Zoller. Interfacing quantum-optical and solid-state qubits. *Physical review letters*, 92(24):247902, 2004.

[18] L Tian, R Blatt, and P Zoller. Scalable ion trap quantum computing without moving ions. *The European Physical Journal D-Atomic, Molecular, Optical and Plasma Physics*, 32(2):201–208, 2005.

[19] Nikos Daniilidis and Hartmut Häffner. Quantum interfaces between atomic and solid-state systems. *Annu. Rev. Condens. Matter Phys.*, 4(1):83–112, 2013.

[20] Lin Tian and Peter Zoller. Coupled ion-nanomechanical systems. *Physical review letters*, 93(26):266403, 2004.

[21] Anders S Sørensen, Caspar H van der Wal, Lilian I Childress, and Mikhail D Lukin. Capacitive coupling of atomic systems to mesoscopic conductors. *Physical review letters*, 92(6):063601, 2004.

[22] Klemens Hammerer, Margareta Wallquist, Claudiu Genes, Max Ludwig, Florian Marquardt, Philipp Treutlein, Peter Zoller, Jinwu Ye, and H Jeff Kimble. Strong coupling of a mechanical oscillator and a single atom. *Physical review letters*, 103(6):063005, 2009.

[23] RJ Schoelkopf and SM Girvin. Wiring up quantum systems. *Nature*, 451(7179):664–669, 2008.

[24] Ze-Liang Xiang, Sahel Ashhab, J. Q. You, and Franco Nori. Hybrid quantum circuits: Superconducting circuits interacting with other quantum systems. *Rev. Mod. Phys.*, 85:623–653, Apr 2013.

[25] DJ Heinzen and DJ Wineland. Quantum-limited cooling and detection of radio-frequency oscillations by laser-cooled ions. *Physical Review A*, 42(5):2977, 1990.

[26] Nikos Daniilidis, Dylan J Gorman, Lin Tian, and Hartmut Häffner. Quantum information processing with trapped electrons and superconducting electronics. *New Journal of Physics*, 15(7):073017, 2013.

[27] Wolfgang Paul and Helmut Steinwedel. Ein neues Massenspektrometer ohne Magnetfeld. *Z. Naturforschg.*, 8a:448–450, 1953.

[28] Lowell S Brown and Gerald Gabrielse. Geonium theory: Physics of a single electron or ion in a Penning trap. *Reviews of Modern Physics*, 58(1):233, 1986.

[29] D. Leibfried, R. Blatt, C. Monroe, and D. Wineland. Quantum dynamics of single trapped ions. *Reviews of Modern Physics*, 75(1):281, 2003.

[30] M. Ramm. *Quantum Correlations and Energy Transport in Trapped Ions*. PhD thesis, UC Berkeley, 2014.

[31] Stephan A Schulz, Ulrich Poschinger, Frank Ziesel, and Ferdinand Schmidt-Kaler. Sideband cooling and coherent dynamics in a microchip multi-segmented ion trap. *New Journal of Physics*, 10(4):045007, 2008.

[32] CE Pearson, DR Leibrandt, WS Bakr, WJ Mallard, KR Brown, and IL Chuang. Experimental investigation of planar ion traps. *Physical Review A*, 73(3):032307, 2006.

[33] Signe Seidelin, John Chiaverini, Rainer Reichle, John J Bollinger, Didi Leibfried, Joe Britton, JH Wesenberg, RB Blakestad, RJ Epstein, DB Hume, et al. Microfabricated surface-electrode ion trap for scalable quantum information processing. *Physical review letters*, 96(25):253003, 2006.

[34] J. H. Wesenberg. Electrostatics of surface-electrode ion traps. *Phys. Rev. A*, 78:063410, Dec 2008.

[35] Andreas Walther, Frank Ziesel, Thomas Ruster, Sam T Dawkins, Konstantin Ott, Max Hettrich, Kilian Singer, Ferdinand Schmidt-Kaler, and Ulrich Poschinger. Controlling fast transport of cold trapped ions. *Physical review letters*, 109(8):080501, 2012.

[36] WK Hensinger, S Olmschenk, D Stick, D Hucul, M Yeo, M Acton, L Deslauriers, C Monroe, and J Rabchuk. T-junction ion trap array for two-dimensional ion shuttling, storage, and manipulation. *Applied Physics Letters*, 88(3):034101, 2006.

[37] C Ospelkaus, U Warring, Y Colombe, KR Brown, JM Amini, D Leibfried, and DJ Wineland. Microwave quantum logic gates for trapped ions. *Nature*, 476(7359):181–184, 2011.

[38] David R Leibrandt, Robert J Clark, Jaroslaw Labaziewicz, Paul Antohi, Waseem Bakr, Kenneth R Brown, and Isaac L Chuang. Laser ablation loading of a surface-electrode ion trap. *Physical Review A*, 76(5):055403, 2007.

[39] RD Knight. Storage of ions from laser-produced plasmas. *Applied Physics Letters*, 38(4):221–223, 1981.

[40] Kenneth R Brown, Robert J Clark, Jaroslaw Labaziewicz, Philip Richerme, David R Leibrandt, and Isaac L Chuang. Loading and characterization of a printed-circuit-board atomic ion trap. *Physical Review A*, 75(1):015401, 2007.

[41] Maximilian Harlander, Michael Brownnutt, Wolfgang Hänsel, and Rainer Blatt. Trapped-ion probing of light-induced charging effects on dielectrics. *New Journal of Physics*, 12(9):093035, 2010.

[42] T. Pruttivarasin. *Spectroscopy, fundamental symmetry tests and quantum simulation with trapped ions*. PhD thesis, UC Berkeley, 2014.

[43] S Gulde, D Rotter, P Barton, F Schmidt-Kaler, R Blatt, and W Hogervorst. Simple and efficient photo-ionization loading of ions for precision ion-trapping experiments. *Applied Physics B*, 73(8):861–863, 2001.

[44] M Sankari, PV Kiran Kumar, and MV Suryanarayana. Optical selectivity calculation of calcium isotopes in a double-resonance ionization scheme. *Journal of Physics B: Atomic, Molecular and Optical Physics*, 33(21):4927, 2000.

[45] R Gerritsma, G Kirchmair, F Zähringer, J Benhelm, R Blatt, and CF Roos. Precision measurement of the branching fractions of the $4p^2P_{3/2}$ decay of Ca II. *The European Physical Journal D*, 50(1):13–19, 2008.

[46] PA Barton, CJS Donald, DM Lucas, DA Stevens, AM Steane, and DN Stacey. Measurement of the lifetime of the $3d^2D_{5/2}$ state in $^{40}Ca^+$. *Physical Review A*, 62(3):032503, 2000.

[47] Jian Jin and DA Church. Precision lifetimes for the Ca+ $4p^2P$ levels: experiment challenges theory at the 1% level. *Physical review letters*, 70(21):3213, 1993.

[48] Michael Ramm, Thaned Pruttivarasin, Mark Kokish, Ishan Talukdar, and Hartmut Häffner. Precision measurement method for branching fractions of excited $P_{1/2}$ states applied to $^{40}Ca^{+}$. *Physical review letters*, 111(2):023004, 2013.

[49] Daniel FV James. Quantum dynamics of cold trapped ions with application to quantum computation. *Applied Physics B: Lasers and Optics*, 66(2):181–190, 1998.

[50] D. J. Wineland, R. E. Drullinger, and F. L. Walls. Radiation-pressure cooling of bound resonant absorbers. *Phys. Rev. Lett.*, 40:1639–1642, Jun 1978.

[51] W. Neuhauser, M. Hohenstatt, P. Toschek, and H. Dehmelt. Optical-sideband cooling of visible atom cloud confined in parabolic well. *Phys. Rev. Lett.*, 41:233–236, Jul 1978.

[52] R. Loudon. *The Quantum Theory of Light*. OUP Oxford, 2000.

[53] CA Blockley, DF Walls, and H Risken. Quantum collapses and revivals in a quantized trap. *EPL (Europhysics Letters)*, 17(6):509, 1992.

[54] C.F. Roos. *Controlling the quantum state of trapped ions*. PhD thesis, Leopold-Franzens-Universität Innsbruck, 2000.

[55] David J Wineland, C Monroe, Wayne M Itano, Dietrich Leibfried, Brian E King, and Dawn M Meekhof. Experimental issues in coherent quantum-state manipulation of trapped atomic ions. *J. Res. Natl. Inst. Stand. Technol.*, 103:259, 1998.

[56] William Shockley. Currents to conductors induced by a moving point charge. *Journal of applied physics*, 9(10):635–636, 1938.

[57] DJ Wineland and HG Dehmelt. Principles of the stored ion calorimeter. *Journal of Applied Physics*, 46(2):919–930, 1975.

[58] David J Wineland and Wayne M Itano. Laser cooling of atoms. *Physical Review A*, 20(4):1521, 1979.

[59] Michel H Devoret et al. Quantum fluctuations in electrical circuits. *Les Houches, Session LXIII*, 7(8), 1995.

[60] J Ye, DW Vernooy, and HJ Kimble. Trapping of single atoms in cavity QED. *Physical Review Letters*, 83(24):4987, 1999.

[61] Kilian Singer, Ulrich Poschinger, Michael Murphy, Peter Ivanov, Frank Ziesel, Tommaso Calarco, and Ferdinand Schmidt-Kaler. Colloquium: Trapped ions as quantum bits: Essential numerical tools. *Reviews of Modern Physics*, 82(3):2609, 2010.

[62] G. Littich. Electrostatic control and transport of ions on a planar trap for quantum information processing. Master's thesis, UC Berkeley, 2011.

[63] John David Jackson. *Classical electrodynamics*. Wiley, New York, NY, 3rd ed. edition, 1999.

[64] M Brownnutt, M Kumph, P Rabl, and R Blatt. Ion-trap measurements of electric-field noise near surfaces. *Reviews of Modern Physics*, 87(4):1419, 2015.

[65] N Daniilidis, S Gerber, G Bolloten, M Ramm, A Ransford, E Ulin-Avila, I Talukdar, and H Häffner. Surface noise analysis using a single-ion sensor. *Physical Review B*, 89(24):245435, 2014.

[66] Dustin A Hite, Yves Colombe, Andrew C Wilson, Kenton R Brown, U Warring, R Jördens, John D Jost, KS McKay, DP Pappas, D Leibfried, et al. 100-fold reduction of electric-field noise in an ion trap cleaned with in situ argon-ion-beam bombardment. *Physical review letters*, 109(10):103001, 2012.

[67] Pulak Dutta and PM Horn. Low-frequency fluctuations in solids: 1 f noise. *Reviews of Modern physics*, 53(3):497, 1981.

[68] Q. A. Turchette, Kielpinski, B. E. King, D. Leibfried, D. M. Meekhof, C. J. Myatt, M. A. Rowe, C. A. Sackett, C. S. Wood, W. M. Itano, C. Monroe, and D. J. Wineland. Heating of trapped ions from the quantum ground state. *Phys. Rev. A*, 61:063418, May 2000.

[69] Jaroslaw Labaziewicz, Yufei Ge, Paul Antohi, David Leibrandt, Kenneth R Brown, and Isaac L Chuang. Suppression of heating rates in cryogenic surface-electrode ion traps. *Physical review letters*, 100(1):013001, 2008.

[70] Louis Deslauriers, S Olmschenk, D Stick, WK Hensinger, J Sterk, and C Monroe. Scaling and suppression of anomalous heating in ion traps. *Physical Review Letters*, 97(10):103007, 2006.

[71] Cryogenic Technologies Group. Cryogenics technologies group, material properties, 2016.

[72] ED Marquardt, JP Le, and Ray Radebaugh. Cryogenic material properties database. In *Cryocoolers 11*, pages 681–687. Springer, 2002.

[73] Jack W. Ekin. *Experimental Techniques For Low-Temperature Measurements: Cryostat Design, Material Properties, and Superconductor Critical-Current Testing*. Oxford University Press, 2007.

[74] Louis J Salerno, Peter Kittel, and Alan L Spivak. Thermal conductance of pressed metallic contacts augmented with indium foil or Apiezon grease at liquid helium temperatures. *Cryogenics*, 34(8):649–654, 1994.

[75] A Zverev and H Blinchikoff. Realization of a filter with helical components. *IRE Transactions on Component Parts*, 8(3):99–110, 1961.

[76] F.J. Kopp and T Ashworth. Carbon resistors as low temperature thermometers. *Review of Scientific Intruments*, 43(2):327–332, 1972.

[77] Herbert Gross, Wolfgang Singer, and Michael Totzeck. *Handbook of optical systems*, volume 1. Wiley Online Library, 2005.

[78] S. Ulmer, H. Kracke, K. Blaum, S. Kreim, A. Mooser, W. Quint, C. C. Rodegheri, and J. Walz. The quality factor of a superconducting RF resonator in a magnetic field. *Review of Scientific Instruments*, 80:123302, 2009.

[79] F. Ayela, J.L. Bret, and J. Chaussy. Design and applications of a very low losses superconducting LC resonator at 4.2 K. *Cryogenics*, 32(1):35–38, 1991.

[80] P Falferi, M Cerdonio, L Franceschini, R Macchietto, S Vitale, and JP Zendri. A high inductance kHz resonator with a quality factor larger than 10^6. *Review of scientific instruments*, 65(9):2916–2919, 1994.

[81] Michele Bonaldi, Paolo Falferi, Massimo Cerdonio, Andrea Vinante, Rita Dolesi, and Stefano Vitale. Thermal noise in a high Q cryogenic resonator. *Review of scientific instruments*, 70(3):1851–1856, 1999.

[82] Gabriele Grandi, Marian K Kazimierczuk, Antonio Massarini, and Ugo Reggiani. Stray capacitances of single-layer solenoid air-core inductors. *IEEE Transactions on Industry Applications*, 35(5):1162–1168, 1999.

[83] KL Corum, PV Pesavento, and JF Corum. Multiple resonances in RF coils and the failure of lumped inductance models. In *Sixth International Symposium Nikola Tesla, Belgrade, Serbia*, 2006.

[84] Kenneth L Corum and James F Corum. RF coils, helical resonators and voltage magnification by coherent spatial modes. In *Telecommunications in Modern Satellite, Cable and Broadcasting Service, 2001. TELSIKS 2001. 5th International Conference on*, volume 1, pages 339–348. IEEE, 2001.

[85] Caio Marcelo de Miranda and Sérgio Francisco Pichorim. Self-resonant frequencies of air-core single-layer solenoid coils calculated by a simple method. *Electrical Engineering*, 97(1):57–64, 2015.

[86] A.G. Kandoian and William Sichak. Wide-frequency-range tuned helical antennas and circuits. *Electrical Communication*, 30(4):294–299, 1953.

[87] David M. Pozar. *Microwave Engineering 4th edition*. Whiley, 2012.

[88] Agilent Technologies Inc. *Genesys 2008.01 Documentation Set*. Agilent Technologies, Inc., 395 Page Mill Road, Palo Alto, CA 94304 U.S.A., 1 2008. loss tangent data.

[89] H.A. Willis, W. Reddish, K.A. Buckingham, D.T. Llewellyn-Jones, R.J. Knight, and H.A. Gebbie. Measurement of the absorption spectrum of polytetrafluoroethylene in the near millimeter region by an untuned cavity. *Polymer*, 22:20, 1981.

[90] Jerzy Krupka, Krzysztof Derzakowski, Michael Tovar, John Hartnett, and Richard G. Geyer. Complex permittivity of some ultralow loss dielectric crystals at cryogenic temperatures. *Meas. Sci. Technol.*, 10:387, 1999.

[91] M. Barucci, G. Bianchini, E. Gottardi, I. Peroni, and G. Ventura. Dielectric properties of stycast 1266 over the 0.07-300 K temperature range. *Cryogenics*, 39:963–966, 1999.

[92] Howard W. Jr. Starkweather, Peter Avakian, R.R. Jr. Matheson, John J. Fontanella, and Mary C. Wintersgill. Low-temperature dielectric behavior of polymers and copolymers of tetrafluoroethylene. *Macromolecules*, 24(13):3853–3856, 1991.

[93] R. Morrell. *Handbook of Properties of Technical Engineering Ceramics. Part 2. Data Reviews, Section I. High-alumina ceramics*. Stationery Office Books, 1987.

[94] Jerzy Krupka, Richard G. Geyer, Matthias Kuhn, and Johann Heyen Hinken. Dielectric properties of single crystals of Al_2O_3, $LaAlO_3$, $NdGaO_3$, $SrTiO_3$, and MgO at cryogenic temperatures. *IEEE Transactions on Microwave Theory and Techniques*, 42(10):1886–1889, 1994.

[95] Jean-Michael Le Floch, Romain Bara, John G. Hartnett, Michael E. Tobar, David Mouneyrac, Damien Passerieux, Dominique Cros, Jerzy Krupka, Philippe Goy, and Sylvain Caroopen. Electromagnetic properties of polycrystalline diamond from 35 K to room temperature and microwave to terahertz frequencies. *Journal of Applied Physics*, 109:094103, 2011.

[96] Michael Edmund Tobar and John Gideon Hartnett. Proposal for a new test of the time independence of the fine structure constant α using orthogonally polarized whispering gallery modes in a single sapphire resonator. *Physical Review D*, 67(6):062001, 2003.

[97] VR Karasik and I Yu Shebalin. Superconducting properties of pure niobium. *Soviet Journal of Experimental and Theoretical Physics*, 30:1068, 1969.

[98] T. Van Duzer and C.W. Turner. *Principles of Superconductive Devices and Circuits*. Elsevier, 1981.

[99] J.E. Jensen, W.A. Tuttle, R.B. Steward, H Brechna, and A.G. Prodell. *Selected Cryogenic Data Notebook*. Brookhaven National Laboratory, 1980.

[100] Curt Schmidt. Simple method to measure the thermal conductivity of technical superconductors, eg, NbTi. *Review of Scientific Instruments*, 50(4):454–457, 1979.

[101] D Gandolfi, M Niedermayr, M Kumph, M Brownnutt, and R Blatt. Compact radio-frequency resonator for cryogenic ion traps. *Review of Scientific Instruments*, 83(8):084705, 2012.

[102] John C Young and Chalmers M Butler. Inductance of a shielded coil. *IEEE Transactions on Antennas and Propagation*, 49(6):944–953, 2001.

[103] JD Siverns, LR Simkins, S Weidt, and WK Hensinger. On the application of radio frequency voltages to ion traps via helical resonators. *Applied Physics B*, 107(4):921–934, 2012.

[104] Andreas Mooser. *Der g-Faktor des Protons*. PhD thesis, Johannes Gutenberg-Universitt, 2013.

[105] N Daniilidis, S Narayanan, SA Möller, R Clark, TE Lee, PJ Leek, A Wallraff, St Schulz, F Schmidt-Kaler, and H Häffner. Fabrication and heating rate study of microscopic surface electrode ion traps. *New Journal of Physics*, 13(1):013032, 2011.

[106] S Narayanan, N Daniilidis, SA Möller, R Clark, F Ziesel, K Singer, F Schmidt-Kaler, and H Häffner. Electric field compensation and sensing with a single ion in a planar trap. *Journal of Applied Physics*, 110(11):114909, 2011.

[107] E. Ulin-Avila. *Nanoscale interfacial structure for Novel Opto-electronic and Ion-trapping Devices*. PhD thesis, UC Berkeley, 2013.

[108] Kezia Cheng. Electron radiation as an indicator of gold nodule defect during E-beam evaporation. In *2011 CS MANTECH Conference*, 2011.

[109] James Cotronakis, Ray Lawrence Martin Clarke, Jan Campbell, and Craig Gaw. Continuous defectivity improvements and impact on high density metal-insulator-metal (hdmim) capacitor yields. In *2004 International Conference on Compound Semiconductor Manufacturing Technology*, 2004.

[110] LG Feinstein and MJ Bill. Reduction of nodules in electron-gun-evaporated au films. *Journal of Vacuum Science & Technology*, 12(3):704–708, 1975.

[111] Philipp Schindler, Dylan J Gorman, Nikos Daniilidis, and Hartmut Häffner. Polarization of electric-field noise near metallic surfaces. *Physical Review A*, 92(1):013414, 2015.

[112] I Talukdar, DJ Gorman, N Daniilidis, P Schindler, S Ebadi, H Kaufmann, T Zhang, and H Häffner. Implications of surface noise for the motional coherence of trapped ions. *Physical Review A*, 93(4):043415, 2016.

[113] M. F. Brandl, M. W. van Mourik, L. Postler, A. Nolf, K. Lakhmanskiy, R. R. Paiva, S. Mller, N. Daniilidis, H. Hffner, V. Kaushal, T. Ruster, C. Warschburger, H. Kaufmann, U. G. Poschinger, F. Schmidt-Kaler, P. Schindler, T. Monz, and R. Blatt.

[114] Elliott Philofsky. Intermetallic formation in gold-aluminum systems. *Solid-State Electronics*, 13(10):1391–1394, 1970.

[115] Texas Instruments. Plastic encapsulant impact on au/al ball bond intermetallic life. Technical report, Texas Instruments.

[116] Jianbiao Pan and Patrice Fraud. Wire bonding challenges in optoelectronics packaging. Technical report, 2004.

[117] Francis Balestra and Gérard Ghibaudo. *Device and circuit cryogenic operation for low temperature electronics*. Springer, 2001.

[118] F Teyssandier and D Prêle. Commercially available capacitors at cryogenic temperatures. In *Ninth International Workshop on Low Temperature Electronics-WOLTE9*, 2010.

[119] M.L. Siqueira, R.J. Viana, and R.E. Rapp. Carbon and thick film chip resistors as thermometers for heat capacity measurements below 1 K. *Cryogenics*, 31:796–800, 1991.

[120] Mark Laps, Roy Grace, Bill Sloka, John Prymak, Xilin Xu, Pascal Pinceloup, Abhijit Gurav, Michael Randall, Philip Lessner, and Aziz Tajuddin. Capacitors for reduced microphonics and sound emission. In *CARTS-CONFERENCE-*, volume 27, page 207. Components technology institute INC., 2007.

[121] G Bjarke. Microdegree temperature controller for liquid helium ii bath. Technical report, Los Alamos Scientific Lab., N. Mex., 1966.

[122] Richard Patterson, Ahmad Hammoud, and Scott Gerber. Performance of various types of resistors at low temperatures. *NASA Glenn Res. Center, Cleveland, OH, USA, GESS Rep. NAS3-00142*, 2001.

[123] D. Rotter. Photoionisation von kalzium. Master's thesis, Leopold-Franzens-Universität Innsbruck, 2003.

[124] KG Johnson, JD Wong-Campos, A Restelli, KA Landsman, B Neyenhuis, J Mizrahi, and C Monroe. Active stabilization of ion trap radiofrequency potentials. *Review of Scientific Instruments*, 87(5):053110, 2016.

[125] Hans Eriksson and Raymond W Waugh. A temperature compensated linear diode detector. *RF DESIGN*, 23(6):40–47, 2000.

[126] Michael Ramm, Thaned Pruttivarasin, H Hartmut, et al. Energy transport in trapped ion chains. *New Journal of Physics*, 16(6):063062, 2014.

[127] DJ Berkeland, JD Miller, JC Bergquist, WM Itano, and DJ Wineland. Minimization of ion micromotion in a paul trap. *Journal of Applied Physics*, 83(10):5025–5033, 1998.